Integrating Scanning Lidar with LES for Wake Characterization in Complex Terrain

Erik Haugen

Technische Universiteit Delft

Delft University of Technology

Challenge the future

Integrating Scanning Lidar with LES for Wake Characterization in Complex Terrain

by

Erik Haugen

in partial fulfillment of the requirements for the degree of Master of Science in Aerospace Engineering at Delft University of Technology and Master of Science in Engineering (European Wind Energy) at The Technical University of Denmark.

Student number:	4621107	
Project duration:	November 1, 2017 – August 31, 2018	
Supervisors:	Dr.ir. W.A.A.M. Bierbooms	TU Delft
	Prof.Dr. Jacob Berg	DTU
Chairman:	Prof.dr. S.J. Watson	TU Delft

An electronic version of this thesis is available at `http://repository.tudelft.nl/`.

Contents

Nomenclature

$\boldsymbol{u}$	Full velocity vector
$\boldsymbol{X_s}$	Position vector of maximum velocity deficit for a synthetic scan
Δ	Cutoff scale for LES spatial filter
ν	Kinematic viscocity
$\overline{u}$	Mean part of u
ϕ	Lidar elevation angle
σ_u	Standard deviation of u
τ_{ij}	subfilter-scale Reynolds stress
θ	Lidar azimuth angle
$\{\hat{u}, \hat{v}, \hat{w}\}$	Lidar Cartesian velocity
$\{u, v, w\}$	LES velocity
$\{x_L, y_L, z_L\}$	Lidar position in LES coordinates
$\{x_T, y_T, z_T\}$	Turbine position in LES coordintes
$\{x_{L,T}, y_{L,T}\}$	Lidar position with respect to turbine
D	Turbine diameter
E_{u_r}	Wake center velocity error
E_X	Wake center position error
G	LES filter function
h	Height above ground
J	Jacobian
LES	Large-eddy simulation
N_c	Total number of scan cycles within total simulation time
N_i	Number of cells in i direction
N_s	Total number of instantaneous fields in simulation time
N_s	Total number of instantaneous fields of LES
p	Pressure
R	Turbine radius

t_E	Largest eddy size possible in the domain
t_L	Time of LES instantaneous field
t_o	First instant of a scan cycle
t_s	Time of lidar beam sampling
t_{cycle}	Lidar scan cycle period
T_{LES}	Total time simulated in LES
U	Horizontal wind speed, Contravariant flux velocity
u'	Fluctuating part of u
u_r^*	Normalized radial velocity
u_*	Friction velocity
U_d	Velocity deficit
u_r	Lidar LOS speed
u_s	Normalized radial velocity at wake center for a synthetic scan
u_∞	Reference velocity
x^+	Downstream distance from turbine hub
x_t, y_t, z_t	Turbine hub location
$\{\hat{x}, \hat{y}, \hat{z}\}$	Lidar Cartesian coordinate system
$\{\xi, \eta, \zeta\}$	LES computational coordinates
$\{x, y, z\}$	LES coordinate system

Abstract

Flows over complex terrains present uncertainties in wind farm power production and lifespan. Core to these uncertainties are wake dynamics, which lack adequate models and need further validation. In lieu of conducting field experiments, this study integrates scanning lidar measurements and large eddy simulation (LES) to characterize wakes in complex terrain. LES data of flow over complex terrain near Perdigão, Portugal has been generated prior to this study. In the current study a 'synthetic' lidar is placed inside the LES to sample the wind field in space and time as a commercial scanning lidar would. From the synthetic scan fields, the wake is located and characterized using metrics of wake center location and maximum velocity deficit. These metrics are evaluated against the same metrics as determined by LES fields. By treating the LES metrics as the "target", the relative accuracy of the metrics can be determined. This accuracy is a function of the scan geometry, allowing for the geometry to be optimized for wake characterization. Since a lidar scan represents neither an instantaneous field nor a mean field, it is not clear whether the target should be the LES instantaneous or mean fields, therefore the metric accuracy is assessed using different LES fields in the form of instantaneous snapshots of the wake, fields averaged over the time of a scan cycle, and long-term averaged fields.

A set of scan geometries was tested which vary in measurement point density, scan direction, and scan area to find that accuracy depends on a trade-off in the temporal and spatial resolution of the geometry. The results highlight not only the dependency of accuracy on the geometry parameters, but also on which type of LES field is used as the target. The long-term averaged errors were found to be unsuitable for lidars in this terrain, where the longest time scales exceed the simulation time, therefore accuracy was assessed using two types of fields, instantaneous fields taken at the start of the scan cycle, and the cycle-averaged fields. From these results two geometries were identified as performing the best.

Improvements are still needed in the wake detection algorithm, both in distinguishing points in the wake from terrain-generated turbulence and the inclusion of more wake characteristics such as size, shape, and orientation in order to develop more accurate scan geometries, hence improving predictions of wind farm production and longevity. Other scan geometry parameters also need to be explored, including scan paths and non-uniform measurement point densities.

1 Motivation

Sustainable energy is a burgeoning focus of the world economy in both developing and developed countries. According to a study of global wind energy potential in 2012, there is enough kinetic energy available in Earth's winds to be "a primary source of near-zero-emission electric power as the global economy continues to grow through the twenty-first century" [1]. Key challenges facing the industry are, for wind turbines, lowering the levelized cost of energy (LCoE) and increasing the annual power production (AEP). This will make wind energy attractive to investors and lower government subsidies, which is essential in lessening our dependency on fossil fuel energy sources. Growth in wind power installation over the last decade is demonstrated in Figure 2, which shows a five-fold increase in worldwide installed capacity from 2007 to 2016, highlighting the rapid pace of this energy source shift.

Among other factors, the AEP depends on the turbine's electrical power curve, the percentage of time the turbine is operational, and wind distribution at the turbine site. Most of the time, a turbine is operating in the partial load region and full-load region, that is, at wind speeds around the rated wind speed and rated power. This region is shown in Figure 1, colored in gray. In the

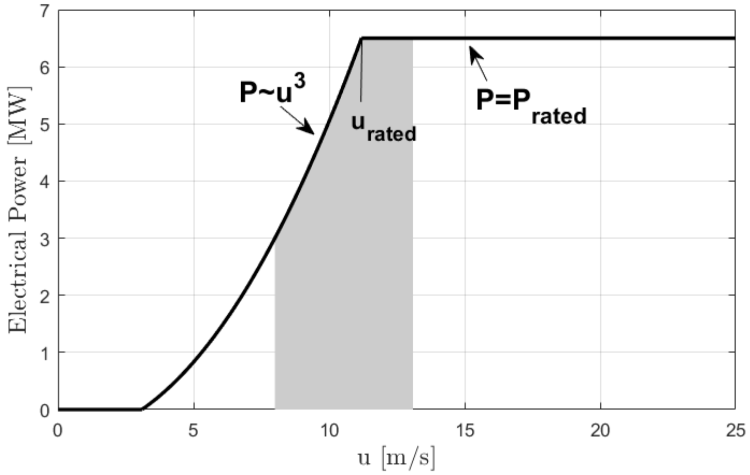

Figure 1: Example power curve for a wind turbine. The majority of operating time is spend within the gray region.

partial load region, the power scales with the cube of the wind speed, while in the full-load region, the power is controlled to be approximately constant. Consequently, the electrical power output of a wind turbine, over an average of its operational time, effectively scales with slightly less than the average wind speed cubed. Nonetheless, since the energy available in the wind scales strongly with the wind speed, predicting its mean and variability in time and space (and across a wide range of scales) are critical factors in energy capture by wind turbines. For incoming flow to a wind turbine, uncertainties of 1% in mean wind speed correspond to roughly 3% uncertainties in power generated, for example. Therefore great economical incentive exists for predicting the incoming wind speed to a wind turbine. Two major influences on mean speed for a turbine are the wakes of upstream turbines and the site conditions, i.e. terrain shape and wind climatology. As will be detailed in this study, there is ample room for improving measurement techniques to predict these effects.

1.1 Wind Farm Wakes

Driving the design of wind farms are the behavior of wind turbine wakes. At the wind turbine rotor plane, momentum is extracted from the incoming wind. A large part of this momentum is transferred to rotational kinetic energy of the rotor, from which power is generated, while the other parts go to the generation of vorticity, viscous dissipation, and structural response of the turbine, among others. This momentum extraction leaves behind a low-momentum wake with a local decrease in mean wind speed and less energy to be harvested by downstream wind turbines. Wakes also produce an increase in turbulent kinetic energy (TKE), which transfers dynamic loads onto wind turbine rotors, decreasing the turbine life-expectancy through fatigue damage and producing unwanted fluctuations in power output. Typically, the spacing between turbines in a wind farm is not large enough for the flow to recover its undisturbed velocity [3]. Therefore, predicting the characteristics of wakes in wind farms is essential in the design and placement of turbines within the wind farm. Since wakes are a key factor in wind farm power output, many engineering models exist to predict their behavior, however the vast majority of them rely on assumptions only valid

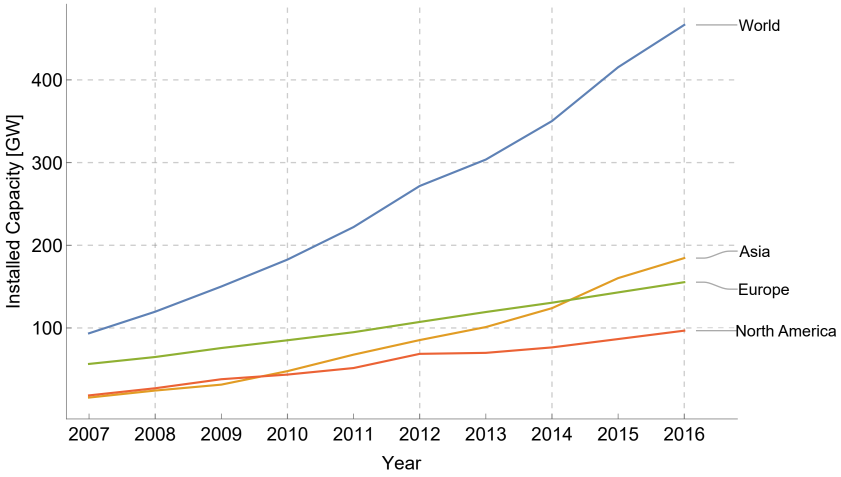

Figure 2: Installed wind energy capacity worldwide from 2007-2016. Source data taken from [2]

for flat terrain. Therefore, a compelling research area has opened for modeling wakes in complex terrain, i.e. over mountains, valleys, escarpments, etc. [4]

1.2 Complex Terrain

The definition of complex terrain in this context will be adopted as “terrain composed of randomly steep slopes” [3]. Besides the fact that the availability of windy, flat terrain sites continues to decrease, complex terrain sites are attractive for wind farm development due to the high wind speeds caused by local speed-up by sharp sloping terrain. For example, exposed ridges can have an increased wind energy content of up to 50% relative to an upstream valley [5]. However, complexity of the terrain also increases cost uncertainty levels. Unlike flat terrains, in which flows are driven by large-scale pressure gradients (synoptic flow) and natural convection by surface heating, ABL flows have the added influence of heating and cooling of the sloped terrain over the diurnal cycle (slope flows) [6]. Along with other non-linear effects, this contributes to wind resource unpredictability relative to flat-terrains. This unpredictability lowers a wind energy project’s value for investors. In 2014, the European Wind Energy Technology Platform estimated that uncertainty levels for complex terrain environments were 15%, and that with improvements in flow models, uncertainty for wind resources of a site could be reduced to as little as 3%. The internal-rate-of-return (IRR) for projects would then be reduced to 5% and the equity input reduced by 56%, subsequently lowering the LCoE [7].

Current state-of-the-art wake models lose accuracy when implemented in complex terrain. Their assumptions of spatial homogeneity generally cannot be used in complex terrain. For atmospheric boundary layer (ABL) flows, terrains with steepnesses above roughly 0.2 ([3]) produce flow separation effects, another major source of modeling error. The majority of current wake models have been developed for homogeneous terrain or no terrain, with only a few including complex terrain [4].

2 Project overview

In this project, LES data of wind flows around a complex terrain site near Perdigão, Portugal, will be sampled using a synthetic (or virtual) lidar, i.e. a single lidar placed within the LES, located downstream of a wind turbine modeled by an actuator disk. The synthetic lidar will sample the LES wind field at the spatial and temporal coordinates as an actual scanning lidar would. Synthetic lidar scans will be used to extract two wind turbine wake characterization metrics, the wake center location and wake center velocity. The values of these metrics will then be compared to those as determined using LES fields, in the form of instantaneous snapshots, fields averaged over the time it takes to complete a scan cycle, and longer time-averaged fields. By treating the LES-determined metrics as true, the accuracy of the synthetic wake metrics can be evaluated. Different scanning geometries will then be constructed with different paths through space. Comparing the accuracy of metrics from different geometries will allow for optimizing the geometry.

In this case, the task of wake characterization using only a single lidar is made challenging primarily by these facts:

- Lidar scan fields are temporally disjunct, i.e. all points in a lidar scan are not sampled at the same time. There is delay as a scanner head moves from one location to the next and therefore the points in a scan field have disjunct time coordinates, ranging from the beginning to the end of the scan period.
- Only one velocity component is available as a single lidar can only return the radial velocity. In complex terrain, the wind cannot be assumed to have negligible vertical velocities, which would allow determination of the horizontal wind speed from radial velocity.
- In complex terrain, the turbine wake interacts with terrain-generated turbulence as well as other flow phenomena particular to ridges, valleys, escarpments, etc. This makes detection of the wake characteristics especially difficult.

The project motivation is then how the tools of LES and lidar measurements can be integrated for improving wake characterization in complex terrain, especially in terms of the scan geometry. Note that this study is not an attempt to solve the full optimization problem, but instead investigates the effect of certain scan geometry parameters on wake metric accuracy.

2.1 Data provided

LES data: The Perdigão LES data has been generated prior to the current study, in support of the New European Wind Atlas's (NEWA) atmospheric flow studies in complex terrain [5]. The data includes:

- 45 fields of 30-min averaged velocities $(\overline{u}, \overline{v}, \overline{w})$
- 45 fields of 30-min standard deviation velocities $(\sigma_u, \sigma_v, \sigma_w)$
- 4000 instantaneous fields of (u, v, w), each 1.6 seconds apart

Galion lidar data: Data was also provided from a single scan taken by a Galion [8] lidar for the Perdigão field experiments in 2017 [9]. The data includes:

- 11400 scan points, with polar coordinates (r, θ, ϕ), measurement time t, radial velocity u_r.

The Galion scan geometry was centered on the turbine rotor at Perdigão, the location of which is also the actuator disk location in the LES. The Galion geometry will be used as a starting point for developing new geometries for this study, which will maintain several attributes of the Galion, including its scanner head speed, sampling rate, radial space between measurement points, and maximum radial range. Further details on the LES model and lidar data will be provided in Section 5.

2.1.1 Perdigão Field Campaign

A field campaign in the complex-terrain site in Portugal near the town of Perdigão, conducted in 2016 and 2017, collected data to characterize both mean and turbulence wind fields. An overview of the project and its goals are described in [9]. The Perdigão (Portuguese for male partridge) campaign was made possible through a European Union (EU) grant, as part of the larger ERANET+ project, which has a stated goal to "quantify error in wind resource models against benchmark datasets". Perdigão researchers used lidar systems as well as met-mast instruments and remote sensing to investigate "multi-scale processes down to the microscale", enabling "high-fidelity microscale simulations and forecasting". Mesoscale models, those with resolution on order of kilometers, give unacceptable errors in AEP estimations [9], let alone hope for terrain-induced turbulence and wake dynamics. Microscales, meaning on the order of seconds to hours in time and up to a few hundred meters in space, are where predictability is most difficult and variability the highest."The expected outcome of the parent (EU) project is the development of a unique high-resolution database at ~500-meter horizontal and ~10-meter vertical resolutions for benchmarking microscale models for wind resource assessment. [9]" The overall goal of the EU project is to improve capabilities in wind energy prospecting and the scientific study of a little known flow regime: microscale mountain meteorology. Quantitatively, one key goal is reducing the prediction of Annual Energy Production (AEP) error [...] by an order of magnitude [9].

Reasons the Perdigão site was selected, are outlined below [9]:

- The relatively mild terrain complexity is suitable for fundamental studies, with easier interpretation of results
- Mean incoming wind is nearly perpendicular to the ridges
- The double ridge is quasi-2D and mimics periodic terrain, suited for numerical models with periodic boundary conditions. This feature is demonstrated in the LES data of Figure 3, which shows the transverse velocity component v to be small compared to the streamwise.
- A met-mast has been operating at the site for several years
- The existence of a single wind turbine already (Enercon 2MW)

The terrain of Perdigão is dominated by two roughly parallel ridges separated by a valley. Photographs of the topography and turbine location are shown in Figure 4, and an overhead view of the terrain and LES domain are shown in Figure 5. In the Perdigão campaign proposal, Lundquist and Fernando [9] illustrated the flow complexities, i.e. the various flow and boundary-layer types in a valley located between two mountain ridges. These include "flow separation, collisions between flows, Coandă effect, secondary flows, convergence/divergence, internal and lee waves, roughness effects, unsteadiness, stratification, land use and directional shear". A transect of the Perdigão LES is shown in Figure 6, with an sample of lidar measurements points. This instantaneous field of the u-component (streamwise) shows flow separation on the leeward sides of the hills. Also

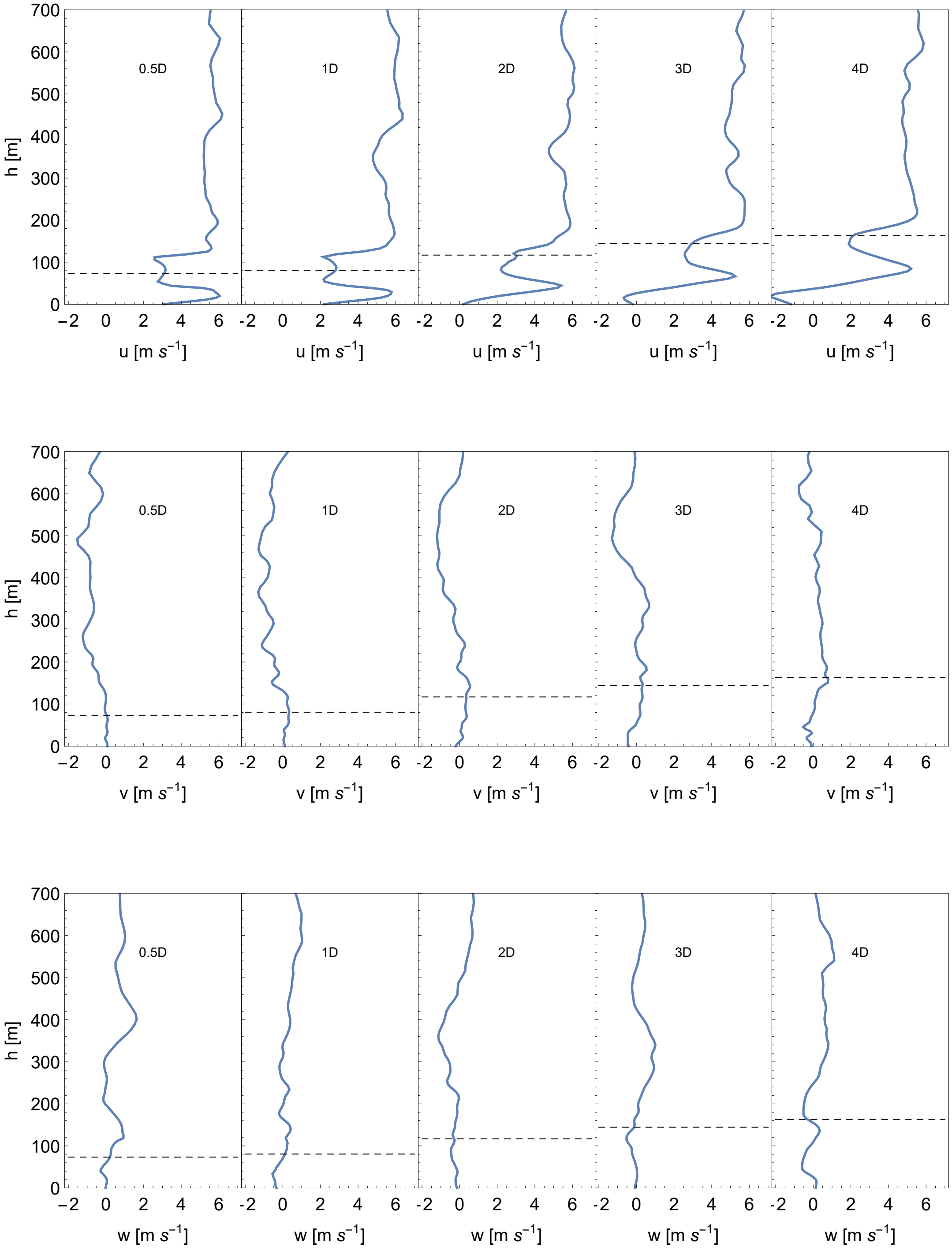

Figure 3: Perdigão LES data of four-hour averaged velocity profiles, directly downstream of the wind turbine. h is height above ground at each downstream location. Dashed line indicates turbine hub height.

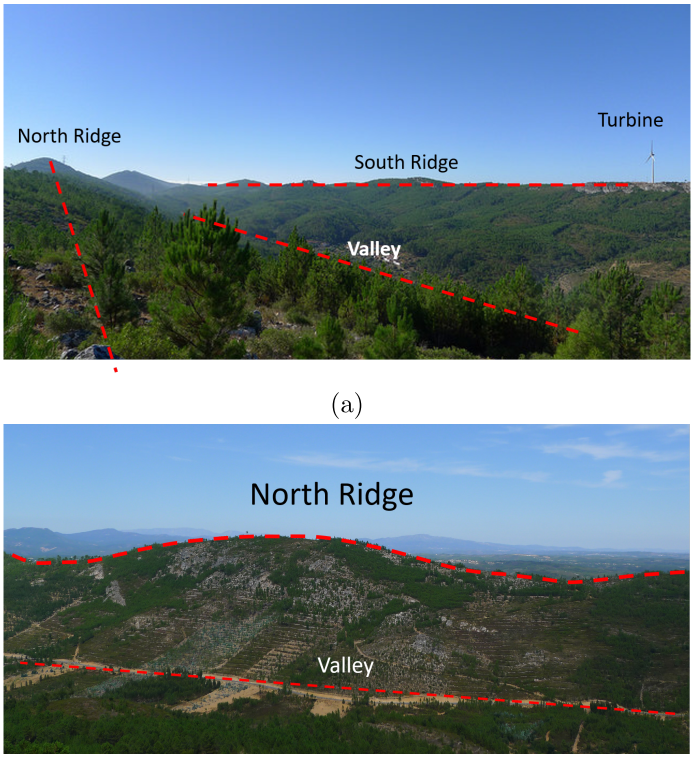

(a)

(b)

Figure 4: Views of Perdigão from the (a) north ridge and (b) south ridge. Photo courtesy of Nikola Vasiljević [10].

visible is the low-momentum wake downstream of the rotor disk, which clearly interacts with the terrain-generated turbulence. Figure 7 shows a topographic relief map of the LES domain, including position of the turbine on the South ridge and lidar in the valley between the ridges.

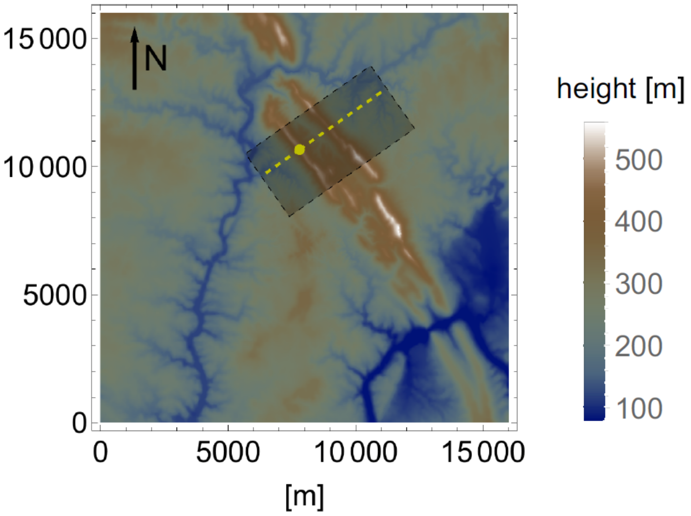

Figure 5: LES domain (shaded region) and surrounding terrain of Perdigão. The yellow dot and dashed line locate the turbine and turbine axis, respectively. Taken from [4].

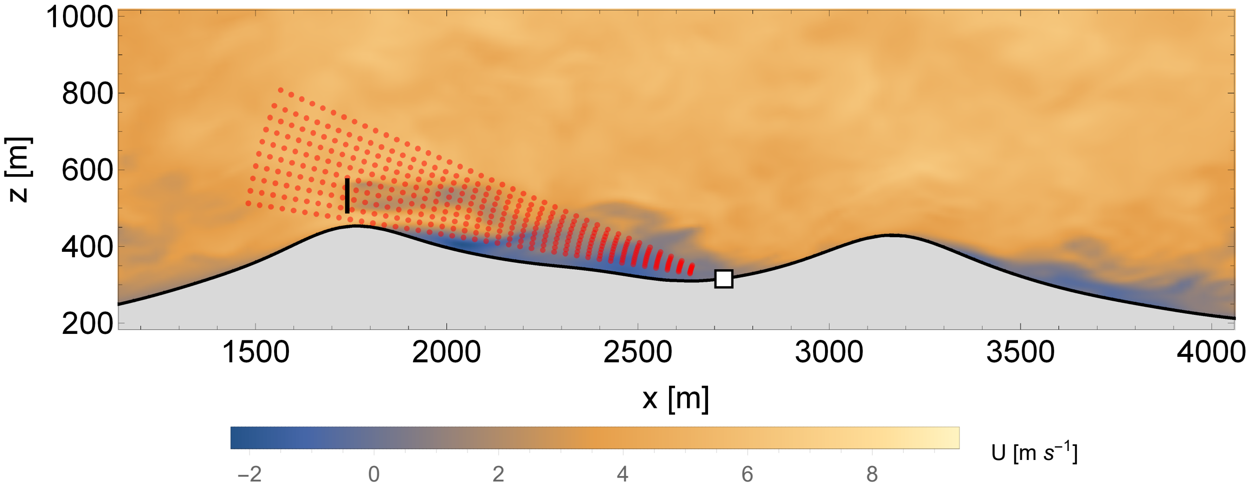

Figure 6: Transect of Perdigão along the streamwise direction. The rotor disk, lidar, lidar measurement locations, and instantaneous u (streamwise) component wind field are shown.

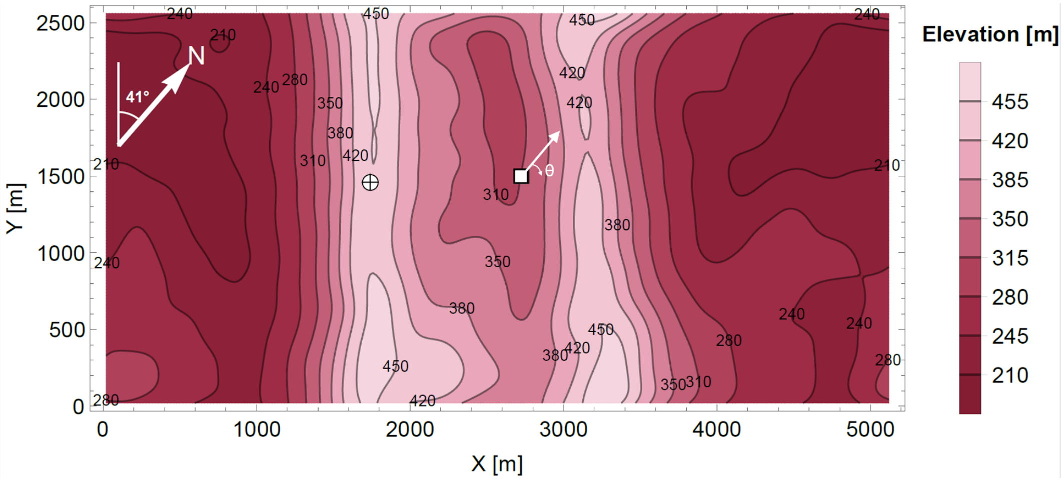

Figure 7: Elevation countours of Perdigão and lidar coordinate system orientation. White crossed circle: wind turbine in LES and field measurements; White Square: lidar location in LES and field measurements.

3 Flow Measurement and Modeling

Despite the inherent wind resources in complex terrain, the turbulent flows induced are non-linear and chaotic, so flow calculation is not possible from first principles. This necessitates numerical modeling and gathering empirical data to validate these models as well as provide new insights into the flow physics, for example, how the wake interacts with terrain-generated turbulence and how wake propagation is modulated by the terrain shape [11]. This section provides an overview of current techniques used to study ABL flows. These each have their strengths and weaknesses and must be chosen depending on, for example, the desired spatial and temporal resolution, cost of installation, and versatility of the instrument. For wind turbines in flow over complex terrain, the length and time scales of interest vary greatly with each experiment, as does the feasibility of deploying the instruments. This latter consideration determines whether remote sensing or direct, *in situ* measurements are more practical. Of course, the choice to measure the flow is usually weighed against achieving the same objective using numerical modeling. In principal, simulations take less time to generate the data and are cheaper monetarily, however models always sacrifice computational cost to the detriment of accuracy. In ABL flows, which have high Reynolds numbers and wide range of spatial-temporal scales, modeling assumptions and associated errors are the perennial bane and necessitate experimental validation.

3.1 Flow Measurement Techniques

In this section, an overview is presented of some of the flow measurement techniques often used to probe ABL flows for wind energy applications. A comparison of the strengths and weaknesses of each technique is presented in Table 1.

3.1.1 In situ measurements

Cups: Cups feature the most simple design of all anemometers. They comprise set of cups fixed to vertical axis, which are free to rotate under the force of wind. They operate on the principle that the rotational speed of the fixture is proportional to the mean wind speed. They measure the projection of the wind vector in the horizontal direction, and so do not indicate the vertical component.

Sonic Anemometers: Sonics are used when higher spatial and temporal resolution is needed. A pair of acoustic transducers, each capable of emitting and receiving acoustic signals, send acoustic waves back and forth and measure the transit time. Wind traveling parallel to the acoustic path adds to or subtracts from the speed of the signal as it moves towards or away from the detector. The temporal resolution is practically point-like with sampling rates of 10 to 20 Hz, while the spatial resolution is an order of 10 higher than a cup's [12]. Because a single pair of transducers provides no information about the wind perpendicular their acoustic path, a set of three orthogonal transducer pairs are generally used, providing the full three-component wind vector.

3.1.2 Remote Sensing

Remote sensing allows measurement of the flow at a distance from the measurement instrument. This provides several advantages— for one, it is a non-invasive technique, as the flow does not interact with the intrument itself. Also, remote sensors are generally mobile and can be readily repositioned to measure different flow locations. Presented here are the two most prevalent techniques for remote sensing in wind energy, sodar and lidar. These are used to measure the wind speed at various heights and ranges in the atmosphere. Other less common techniques such as radar scatterometry have also been used in wind energy applications.

Sodar: Sodars (Sound Detection And Ranging) are ground-based devices probe the atmosphere by emitting sound waves which scatter and are received by a detector. The observed Doppler shift of the signal is proportional to the relative velocity of the wind in the direction of the line-of-sight (LOS), or radial direction. Sound emission consists of several pulses of audible sound waves in three different direction, each slightly inclined from the others. By obtaining the radial velocity vector from three beams, the full 3D velocity vector can be reconstructed. Velocity fluctuations and temperature differences cause a small fraction of the sound energy to scatter in all directions. A small fraction of the scattered sound then reaches the detector and the time delay of the signal is then used to determine the distance from the sodar at which the sound was scattered.

Because of the loss of energy through the backscatter, the received signal strength is highly attenuated. Since sound waves refract easily in the atmosphere, waves that reach the detector can come from many sources and directions and are picked up in the detector as noise. In order to decrease the SNR to acceptable levels, several beams must be averaged. This reduces the temporal resolution to typically 10-minute mean values [3].

Lidar: Lidar (Light Detection And Ranging) is another ground-based device, also operating on the principle of Doppler shift for wind speed measurement. Instead of sound waves, lidars emit light waves. These are scattered off of aerosols (e.g. dust) in the atmosphere and return back to the lidar. As with sodars, processing the detected signal returns the LOS wind velocity at a volume of space in the air. The 3D wind vector can be determined in a similar way to sodar if three or more beams (lidars) are used to reconstruct the wind vector at various heights along a vertical profile. Since light is roughly one million times faster than sound, the sampling frequency is much higher than in sodar. Also, light refracts much less than sound in the atmosphere, so the received signals have a lower SNR [3].

Table 1 provides a starting point for assessing which techniques are most effective in studying wakes. Since wakes are dynamic flow structures, the chosen technique must be capable of capturing wake motion at the appropriate temporal and spatial scales. For example, resolving the time scales of wake meandering (movement of wake location in space and time) and velocity fluctuations associated with fatigue loads is highly important to wind farm planning and wind turbine design, as is resolving the spatial scales needed to resolve the wake edges and the velocity deficit profile. Complex terrain also introduces new, less predictable spatio-temporal scales, so it is important to achieve the spatial and temporal resolution necessary to capture this interaction. These requirements rule out fixed instruments like cups and sonics. Additionally, lidars' mobility allows relocation during a campaign to suit different areas of interest and flow characteristics. Compared with sodars, lidars' temporal resolution is much higher, and wake dynamics on the order of seconds instead of minutes can be resolved. Lidars can be used to probe the wind at a wide range of distances, from inside the rotor plane, to the near wake, to several kilometers from the turbine, making lidars apt for capturing wake interactions with a wind farm. As wind turbines are growing larger, *in situ* measurement systems are unable to probe the flow at tip heights above 200 m, whereas lidars typically reach heights up to 300 m [3]. Measurements this high above the surface are crucial to wind model validation, as typical models lose accuracy quickly after tens of meters above the ground. Additionally, investment costs are greatly reduced compared to met-masts, which have high material costs. For these reasons lidar technology is expected to be a driving force in reducing uncertainties in AEP, validating and improving flow/wake models, and reducing the LCoE [7]. The following section will give an overview of lidar's operating principles.

3.2 Lidar Velocity Retrieval

A lidar emits electromagnetic waves at infrared wave lengths, around 1.5 μm, which are backscattered from suspended particulate matter, or aerosols. The backscattered light is received at the lidar with a frequency shift of

$$\Delta f = f_B - f_E = \frac{2f_E}{c}u_r \tag{3.1}$$

where f_B is the backscattered frequency, f_E the emitted frequency, c the speed of light and u_r, the LOS velocity. This gives an estimate of u_r at the measurement point. Figure 8 shows the lidar emitting and receiving the light used to determine the target's LOS velocity. Inherent in the velocity measurement is the assumption that the aerosols are of sufficiently small size and have a density close to that of air in order to faithfully follow the local flow field.

Each velocity reading samples a measurement volume in space, the form of which is different depending on which type of lidar is used. Two main systems of lidars used today are *continous wave* (cw) and *pulsed* lidars.

Continous wave lidars: In cw lidars, the laser beam is constantly emitted. A lens on the laser head focuses the beam at a specified distance along the line of sight. This focal point is where the center of the measurement volume is located. A diagram of the measurement volume is given in Figure 9. The beam converges at a distance r from the lidar and the effective measurement

Table 1: Comparison of flow measurement techniques

Technique	**Advantages**	**Disadvantages**
Cups	• Point-like spatial resolution • Simple, robust construction • Extremely low-maintenance	• Measures at one point only • Measures only horizontal velocity component • Because of rotational inertia, does not respond to eddies $\leq$ 1-2 m [12]
Sonics	• Point-like temporal resolution • Can measure 3D velocity vector • High sampling rate • Provides measure of buoyant heat flux → Important for stability	• Measures at one point only • Cumbersome to calibrate • Instrument distorts the flow it measures
Sodar	• Portable • Cheaper than lidar	• Limited by CNR at wind speeds $\geq$ 15-20 ms^{-1} [3] • Low temporal resolution • Highly noisy
Lidar	• Portable • Higher temporal & spatial resolution than sodar • Less scatter than sodar • Can measure across entire rotor plane accurately	• More expensive than sodar • Poor estimation of wind direction in complex terrain (by a single lidar) • Lower maximum heights than sodar

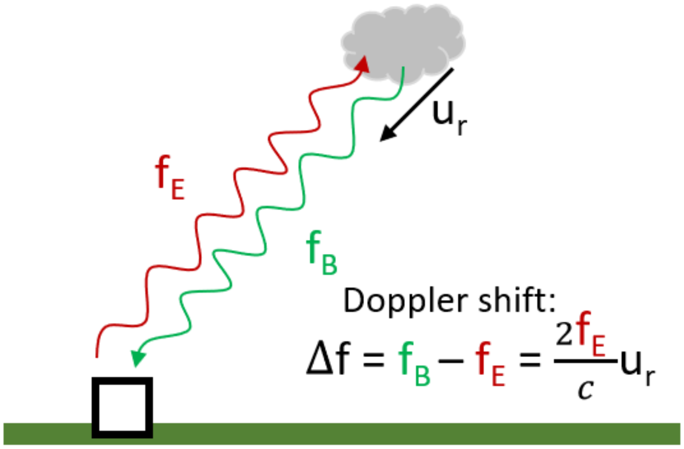

Figure 8: Lidar determination of LOS velocity via Doppler shift. Adapted from [12].

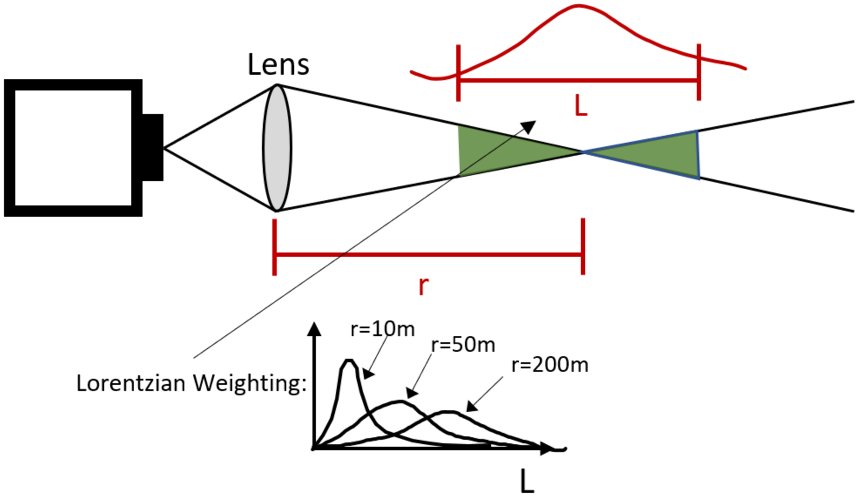

Figure 9: Operating principle of a continuous-wave lidar. Adapted from [12]

volume length along the beam is L. Focal distance then increases as measurement locations move further away. The length L is a function of r, so that as the measurement location is moved farther, the measurement volume (proportional to L) increases. Therefore, the effective spatial resolution decreases at far distances, leading to cw lidars being known as "short-range" lidars, since at longer distances the spatial resolution becomes unacceptable.

As shown in Figure 9 is a weighting or filter function which spans the measurement volume. The shape of this function, (typically a Lorentzian distribution [12]), determines how the signals from within the measurement volume are weighted in averaging the velocities. In this way, signals originating from aerosols close to the focal point (usually coincident with the center of weighting distribution) are weighted most heavily and those farther away less-so.

All signals originating from the measurement volume are used in computing a representative velocity. These are effectively a long time series of voltages read by the lidar. This long time series is then broken into shorter segments and Fourier-transformed into the frequency domain. The resulting spectrum of each segment shows the respective power contained in each of the backscattered frequencies. In order to improve the signal-to-noise-ratio (SNR), the many spectra are averaged, and a clear peak at f_B is observed. By Equation 3.1, the radial wind velocity can then be determined.

Pulsed lidars: In contrast to cw lidars, which measure at one location at a time, pulsed lidars measure several locations virtually simultaneously. Instead of sending out a continuous beam, a sequence of short pulses are emitted. Light from these pulses is backscattered and then received, and the arrival time can be used along with the speed of light to find the distance of the aerosol. Figure 10 illustrates a single pulse and the relationship between detection time and aerosol distance. Light which has an arrival time t_1 is reflected off a target at a distance of $c \cdot t_1/2$. A pulse has a finite duration T_p, so that backscattered light from a distance $c \cdot t_1/2$ will be collected from t_1 to $t_1 + T_p$ at the detector. By selecting the appropriate arrival time window, signals from a certain

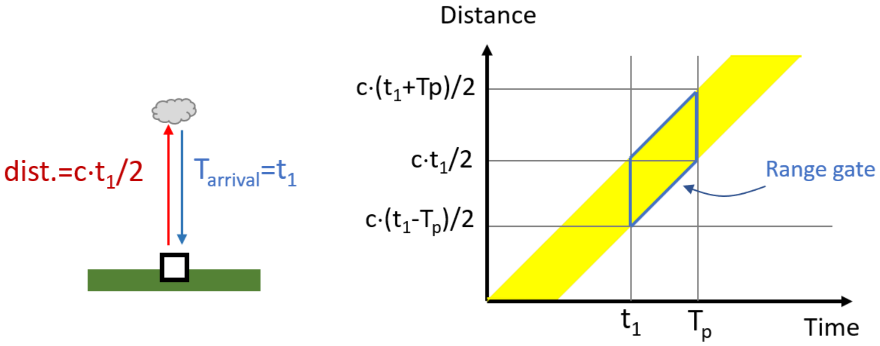

Figure 10: Aerosol distance and arrival time for a lidar pulse. Adapted from [12].

distance are analyzed. This technique is called range-gating. Therefore the length of T_p determines the size of the measurement volume. Locations of the volumes are then called "range gates", and a single pulse measures velocities at multiple range gates virtually simultaneously, limited only by the SNR at large distances. Because the size of a light pulse remains practically constant as it propagates, the measurement volume also stays constant, in contrast with cw lidar. This allows the same spatial resolution to be maintained far from the lidar, earning pulsed lidars the the moniker "long-range" lidars. Resolutions are typically around half the pulse length, so 25-40 m. While the temporal resolution is less for pulsed lidars (around 2-3 wind speed samples per second compared to 500 for cw lidars [3]), many points (range gates) are measured at the same time. Due to the relatively large distances needed to be measured for this study, a pulsed lidar is used, namely the Galion [8].

Time series of signals from each measurement volume are sampled for a period of time, usually T_p. Once the signal arrives the steps for processing are as follows [3]:

1. Separate the times series according to desired range gates
2. Compute the spectrum for each time series
3. Average the spectra for each range gate, over multiple pulses
4. Locate the peak corresponding to Doppler-shifted frequency f_B
5. Compute the LOS velocity for each range gate

3.3 Lidar Scanning Techniques

A useful feature of many lidars is a scanning mode of the laser head. With a scanning lidar, a measurement field is created and used to estimate the wind speed and/or direction. A scanning lidar features a scanning head which emits the beams and can rotate its azimuth and pitch angle. These two degrees of freedom and as well as the coordinate system used by the Galion is given in Figure 11. The Galion's coordinate system is defined as azimuth $\theta = 0^o$ pointing North, and positive clockwise; elevation angle $\phi = 0^o$ pointing parallel with the horizon and positive pitching upwards, and radial coordinate r, the distance from the scanning head. A scan pattern, or geometry,

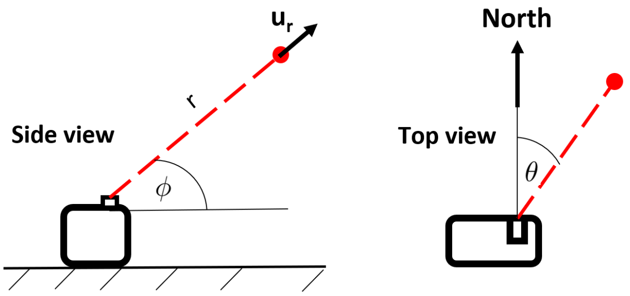

Figure 11: Schematic of the Galion scanning lidar. In lidar coordinates, $\theta = 0$ points North, and positive clockwise; $\phi = 0$ points horizontally, and positive pitching upwards, and r is the distance from the lidar scanning head.

consists of a set of points in space and the path of the lidar's scanning beam through these points. This pattern is often pre-programmed, for example, at the beginning of the day according to wind direction forecast. Then the lidar is left to run through the pattern continuously to collect data. Some scan patterns which are typical elements of scan geometries are given below, as well as illustrated in 12.

VAD Velocity azimuth display or VAD scans. These conical scans are used for determining the wind direction, and have been shown to accurately determine the vertical wind-shear profile. A common method is to emit a beam upward at a high elevation angle, and keep this angle constant while the azimuthal angle is rotated in steps of 90^o (see Figure 13). This gives four LOS velocity readings along the perimeter at one height, allowing the reconstruction of the 3D velocity vector at that height. However, combining the LOS velocities from different locations around the perimeter assumes the wind distribution is constant, i.e. spatially homogeneous, and this assumption is not accurate above complex terrain.

RHI: Range height indicator, also known as elevation scans. The azimuthal angle is held constant as elevation angle changes.

PPI: Plan position indicator, also known as sector or azimuthal scans. The elevation angle is held constant while azimuthal angle changes.

In Figure 12, the PPI and RHI scans clearly show the presence of a wake. From these data, wake characteristics can be estimated, including

- Center location
- Height and width
- Length scales
- Wake meandering
- Velocity Deficit

For the purposes of wake detection and characterization, this study will use a series of vertical cross-planes (perpendicular to the turbine axis) of velocity data downstream of the turbine. Often such planes are formed by single RHI scans, however when the mean flow direction is perpendicular to the planes of interest, as they are in the present study, the points forming these planes must be extracted from the volume of space probed by a stack of PPI scans, where θ is varied at constant ϕ for different ϕs (so-called stacked sector scans). An example of the lidar beam path for a stacked sector scan is shown in Figure 14, and an RHI path in Figure 15, where in both cases only data points at a single r are shown.

3.3.1 Lidar Uncertainty

The accuracy of quantifying wake characteristics by scanning lidars will depend on the capabilities of the particular lidar instrument. For instance, spatial and temporal resolution are a limited by scanner head speed and measurement volume size. Additionally, the geometry of the scan has been shown to be directly related to the error in wake characteristics, in particular, two parameters, the density of measurement points and the area covered by the scanned points, both of which vary with downstream distance from the lidar. Since the laser head takes time to move from point to point, there is a lag between consecutive measurements, that is to say the measurement points are temporally disjunct and the scan data represent neither an instantaneous snapshot of the flow nor a mean field, which introduces error in flow measurements compared to true instantaneous and mean fields [13]. The duration of a scan is then dependent on the choice of path through the points, which becomes an important parameter for quantifying the error. The optimal scanning geometry is expected to weigh trade-offs between spatial and temporal resolution, or measurement point density and flow area probed.

With the exception of a VAD scan, a single lidar can only ever determine the LOS component of the wind vector, while a system of three lidars with beams intersecting at a single location have been used to retrieve all three-components. In cases of horizontal homogeneity, e.g. flat terrain, single lidars can be used to estimate the 2D horizontal velocity components by assuming the vertical velocity component to be much smaller than the two horizontal components (averaged over the collection time). However, complex terrain introduces strong turbulent fluctuations and mean flow in the vertical component, and a single lidar can only estimate u_r.

3.4 Modeling Tools

Modeling allows probing of the flow when use of instrumentation is infeasible due to monetary/time costs, or physically impossible. This is especially pertinent in the ABL, where the largest length scales are in the ratio $\ell/\eta \sim R_t^{3/4}$. The turbulent Reynolds number is $R_t = u_e\ell/\nu$, where ℓ is the typical size of energy-containing eddies (and scales with the ABL height) and u_e the typical velocity of these eddies relative to the mean. In the ABL, typical R_t numbers are on the order of 10^8. This would require on the order of 10^{18} grid points, far exceeding the capacity of industrial computers [14]. Therefore a direct numerical simulation (DNS), which computes all turbulent length scales, is not feasible for ABL flows. Instead, numerical models are formulated which reduce the order of the governing equations by time/spatial averaging, neglecting smaller terms, and making assumptions to reduce complexity.

A comparison of common numerical modeling techniques is given in Table 2. These flow models have all been applied to ABL flows and can be divided into the following groups, which are in order

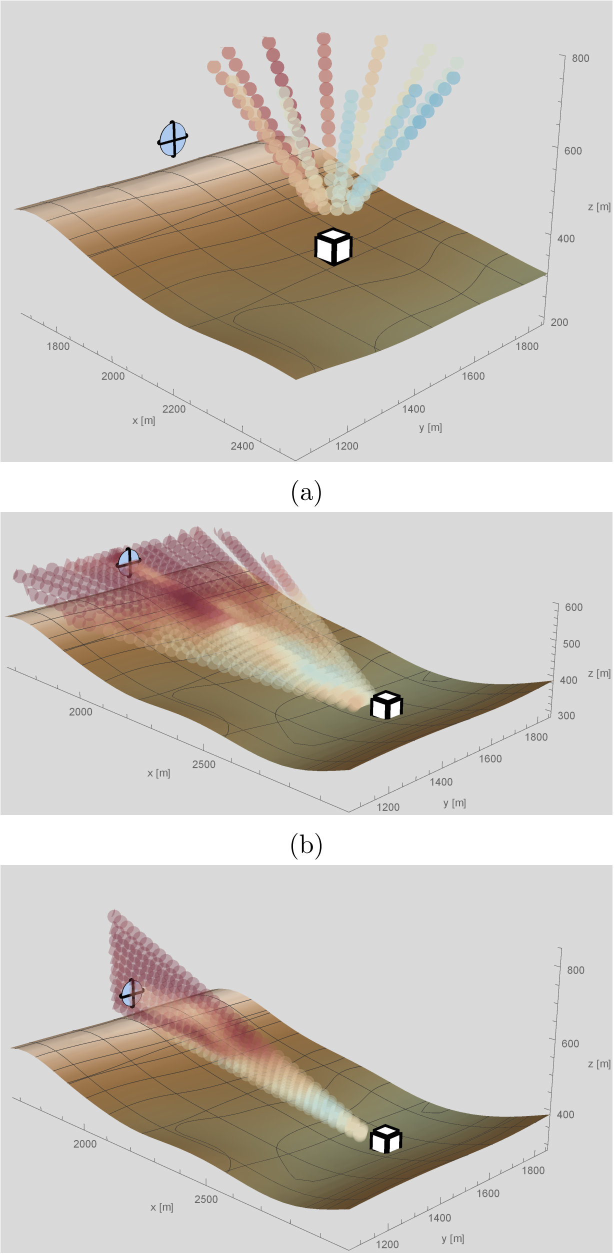

(a)

(b)

(c)

Figure 12: Scanning lidar measurement geometry for a) VAD (velocity-azimuth-display) b)PPI, and c) RHI scan patterns. Instantaneous LES data of radial velocity u_r, color-scaled with red indicating towards the lidar. The lidar (white box) and turbine locations are also indicated.

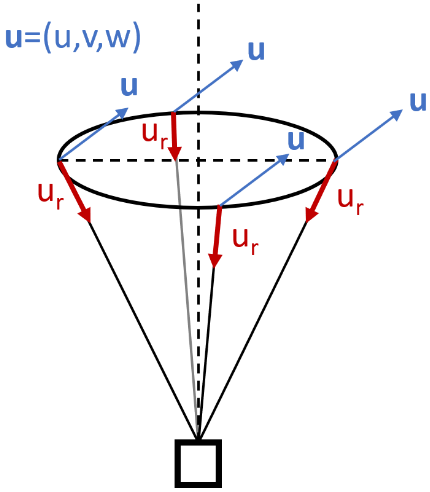

Figure 13: Lidar retrieving the 3-component velocity profile via the VAD technique

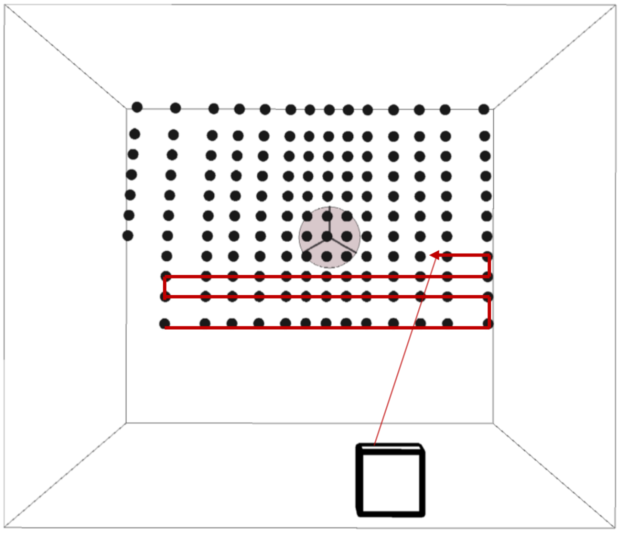

Figure 14: Example lidar beam path in a stacked sector (PPI) scan.

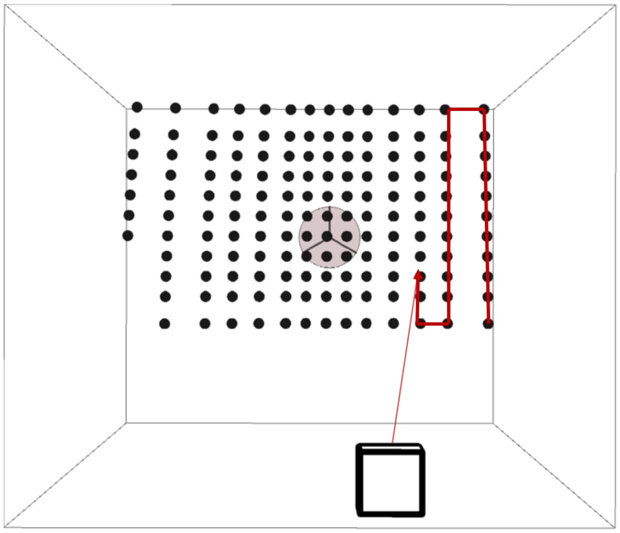

Figure 15: Example lidar beam path for an RHI scan

of increasing fidelity/computational cost.

Engineering Models: These are highly simplified models that can be solved algebraically. They can be empirically and/or theoretically derived and rely on a high number of assumptions that in reality are rarely fulfilled completely. They are so-called zero-equation models because they do not require the solution of any additional equations and are calculated directly from the flow variables.

Linearized Models: The governing equations of linear models are derived from the Navier-Stokes (NS) equations. Linearization relies on the small-disturbance assumption, and therefore holds up well near the ground or in the far wake [15].

In these models and several others it proves useful to decompose the velocity field $\boldsymbol{u} = (u, v, w)$ at point $\boldsymbol{x} = (x, y, z)$ and time t into two parts:

$$\boldsymbol{u}(\boldsymbol{x}, t) = \boldsymbol{U}(\boldsymbol{x}, t) + \boldsymbol{u}'(\boldsymbol{x}, t) \tag{3.2}$$

where $\boldsymbol{U}(\boldsymbol{x}, t)$ is the velocity, averaged in some way, and $\boldsymbol{u}'(\boldsymbol{x}, t)$ is the fluctuating part, or difference from this averaged velocity. This split is called the *Reynolds decomposition* of the velocity. In linear models, the NS equations are linearized by assuming that the fluctuating part of the velocity is small compared to the mean part, that is $\boldsymbol{u}' \ll \boldsymbol{U}$. Then higher order terms are considered small and in turn neglected.

Reynolds-Averaged Navier-Stokes Models: Here again Reynolds decomposition splits the velocity into a fluctuating and mean part, which is then plugged into the NS equations and an ensemble-averaging of the equations is performed. The resulting RANS equations look like the original NS equations but with an added term, the turbulent fluxes or *Reynolds stress* term. These equations provide information on the mean flow quantities but tell little to nothing about the instantaneous flow. To achieve problem closure, these terms are modeled. Among the best known

Table 2: Comparison of flow model types

Model	Advantages	Disadvantages
Engineering Models	• Analytical solution - no numerical artifacts • Simple, computationally cheap implementation	• Oversimplified for most applications
Linearized Models	• Captures effects of roughness change, gentle hills, and obstacles • Computationally cheaper than non-linear models	• Cannot model non-linear effects, e.g. flow separation → not suitable for complex terrain
RANS	• Computationally cheaper than LES and DNS	• Only steady flows can be computed • Less widely applicable than LES and DNS
LES	• Can model complex geometry flows • Computes mean and unsteady flow solution	• Larger computational cost than RANS
DNS	• Computes full range of turbulent fluctuations, down to Kolmogorov scales	• Largest computational cost • Infeasible tool for many applications, except simple geometries and low Re flows.

models are the k-ϵ and Reynolds stress model.

Large-Eddy Simulation In LES, instead of ensemble-averaging the NS equations, a spatial filtering is applied to the equations. This avoids the computation of eddies smaller than a chosen cut-off scale Δ. This is in contrast to ensemble-averaging in RANS, which removes all eddies. Filtering decomposes the turbulent variables into a resolved and subfilter-scale part. Unlike RANS in which all of the turbulent flux is modeled, LES resolves part of the turbulent flux and models the other (the sub-grid stresses) [14]. The solution is a time-varying, 3D, turbulent flow.

Direct Numerical Simulation Here the unsteady NS equations are solved on a grid with spatial resolution fine enough to resolve to smallest (Kolmogorov) turbulent length scales, and at time steps small enough to resolve the fastest turbulent fluctuations. The result is both the mean and fluctuating turbulent flow [16]. Since all scales are resolved, computational costs are enourmous and ABL flows are still far from suitable for DNS.

3.5 LES Governing Equations

The challenge for generation of the wind field is creating a numerical model which accurately captures the effects of turbulent flow in complex terrain, finding the balance between complexity e.g. computational costs and accuracy. For such flows, a wide range of length scales are involved, from those of the atmospheric boundary layer $\mathcal{O}$(km), to those turbulent length scales relevant to wind turbine loads $\mathcal{O}$(m). Large Eddy Simulations (LES) represent a way to compute the large-scale motions, which depend on the terrain shape and are not universal, and represent the smaller-scale motions, which are to some extent universal, through modeling. Computing small-scale motions is an enormous computational cost, which LES-based models avoid, making them an apt choice for modeling unsteady ABL flows [17].

Here the basic formulation of governing equations will be described for a typical LES. Before this, it must be mentioned that there are several types of averaging, and indeed the models of Table 2 rely on different averaging methods. Therefore it is practical to differentiate these with unique notation. We will use $\langle\cdot\rangle$ to denote an ensemble average of a random variable, i.e. its arithmetic mean over all realizations. An example of an *estimate* of the ensemble average for the streamwise velocity component u is given in Equation 3.3.

$$\langle u\rangle = \frac{1}{n}\sum_{i=1}^{n} u_i, \tag{3.3}$$

where all n realizations are independent. Realizations in this context could be separate simulations with the same control parameters set, e.g. mean wind speed and direction, terrain shape, grid resolution, etc. The *true* ensemble average is obtained by applying Equation 3.3 over an infinite amount of realizations.

The time average of u will be denoted as

$$\overline{u} = \frac{1}{T}\int_0^T u(t)\ \mathrm{d}t \tag{3.4}$$

where u is averaged over the duration $0 \leq t \leq T$.
The spatial average of u over a volume Ω will be denoted as

$$\underline{u} = \int_\Omega u\ \mathrm{d}\Omega \tag{3.5}$$

In LES, this spatial averaging is done over a small volume with sides $\Delta_x, \Delta_y, \Delta_z$ through the application of a filter function G, as discussed below. This function determines the weighting distribution of the average within the volume. For cases when u is stationary in time, the time average in a single realization will converge to the ensemble average as the average time T increases, i.e. $\overline{u} = \langle u\rangle$ as $T \to \infty$. Similarly when u is homogeneous in direction x, for example, the spatial average in a single realization converges to the ensemble average as the averaging distance L increases, i.e. $\underline{u} = \langle u\rangle$ as $L \to \infty$ [14].

Depending on the type of averaging being performed, the two components of the Reynolds decomposition in Equations 3.2 are interpreted in different ways, i.e. $\boldsymbol{U} \equiv \langle\boldsymbol{u}\rangle, \overline{\boldsymbol{u}}$, or $\underline{\boldsymbol{u}}$. For ensemble averaging, $\boldsymbol{U}$ is the ensemble mean and $\boldsymbol{u'}$ is the fluctuating (turbulent) part. For time averaging, the same is true but for the time mean. For spatial averaging, the decomposition is into a resolved and unresolved (or subgrid-scale) part.

The basic steps in performing an LES are given by Wyngaard [14] and outlined below.

1. A spatial filter is applied to the velocity (or other flow variable) field to obtain the filtered velocity

$$\underline{\boldsymbol{u}}^f(\boldsymbol{x},t) = \iiint_{-\infty}^{\infty} \boldsymbol{u}(\boldsymbol{x}+\boldsymbol{x}',t)G(\boldsymbol{x}-\boldsymbol{x}')dx_1'dx_2'dx_3' \tag{3.6}$$

   where the filter function G can take any number of desired forms. This can be thought of a *local average* around the neighborhood of point $\boldsymbol{u}(\boldsymbol{x},t)$, with weighting function G [14]. In LES, this amounts to low-pass filtering of the flow variable field, allowing the field to be resolved on a relatively coarse grid, with grid spacing proportional to filter width Δ.

   Since the governing equations' solution will be computed on a grid, it is natural to decompose the turbulent variable into a spatially filtered component with $()^r$, which is computationally resolvable, and that which is not, that is, the subgrid-scale part $()^s$. Then,

$$\boldsymbol{u} = \underline{\boldsymbol{u}}^f + (\boldsymbol{u} - \underline{\boldsymbol{u}}^f) = \boldsymbol{u}^r + \boldsymbol{u}^s \tag{3.7}$$

2. The spatial filtering is then applied to the Navier-Stokes equations. A derivation of the following equations can be found in [14]. Here is assumed a Newtonian fluid, of constant density (incompressible) and viscosity, a safe assumption in the ABL. An inertial reference frame is used, so the Coriolis force is neglected. Einstein notation will be employed, and $u_i \equiv \boldsymbol{u}$.

   The continuity equation is filtered as

$$\begin{aligned} \frac{\partial u_i}{\partial x_i} = \frac{\partial u_i^r}{\partial x_i} + \frac{\partial u_i^s}{\partial x_i} &= 0 \\ \frac{\partial u_i^r}{\partial x_i} = \frac{\partial u_i^s}{\partial x_i} &= 0 \end{aligned} \tag{3.8}$$

   Consider the unfiltered momentum equation

$$\frac{\partial u_i}{\partial t} + \frac{\partial u_i u_j}{\partial x_j} = -\frac{1}{\rho}\frac{\partial p}{\partial x_i} + \nu \frac{\partial^2 u_i}{\partial x_j \partial x_j} \tag{3.9}$$

   where p is the pressure and ν the kinematic viscosity. The spatial filter is applied and, neglecting the viscous term on account of the high Re in the surface layer, this yields

$$\frac{\partial u_i^r}{\partial t} + \frac{\partial (u_i u_j)^r}{\partial x_j} = -\frac{1}{\rho}\frac{\partial p^r}{\partial x_i} \tag{3.10}$$

   The filtering has created the quantity $(u_i u_j)^r$ which, in turbulent flow, is different than $u_i^r u_j^r$ and is therefore unknown. We can write this as

$$(u_i u_j)^r = u_i^r u_j^r + \left[(u_i u_j)^r - u_i^r u_j^r\right] = u_i^r u_j^r - \frac{\tau_{ij}}{\rho} \tag{3.11}$$

   In filtering the momentum equation, the Reynolds stress τ_{ij} appears. It is shown in [14] to have both a subfilter-scale part and a resolved part, and is called the subfilter-scale Reynolds stress. It is responsible for the transfer of kinetic energy from the resolved to the subfilter scales, modeling the universal property in turbulence of energy cascade [14]. Equation 3.10 rewritten in terms of this stress yields

$$\frac{\partial u_i^r}{\partial t} + \frac{\partial}{\partial x_j}\left[u_i^r u_j^r - \frac{\tau_{ij}}{\rho}\right] = -\frac{1}{\rho}\frac{\partial p^r}{\partial x_i} \tag{3.12}$$

3. The continuity and momentum equations provide four equations, but unknowns in the subfilter-scale Reynolds stress leave the equations unclosed. Therefore a model is needed for τ_{ij}; often an eddy-viscosity model is chosen.

4. The filtered N-S equations are solved numerically for the u_i^r and p fields at one realization of the flow.

Comparing this spatial filter (or averaging) to an ensemble average of the NS equations, as one uses in a RANS formulation, reveals insights about the degree to which each technique relies on modeling. Ensemble averaging Equation 3.12, and comparing to the Ensemble-averaged unfilterd NS equations reveals the relationship

$$\langle u_i^r u_j^r \rangle - \left\langle \frac{\tau_{ij}}{\rho} \right\rangle = \langle u_i u_j \rangle \tag{3.13}$$

This indicates that of the total kinematic momentum flux $\langle u_i u_j \rangle$, the spatially filtered equations resolve a part $\langle u_i^r u_j^r \rangle$ and model a part $\left\langle \frac{\tau_{ij}}{\rho} \right\rangle$. Typically, the spatial cut-off scale is in the inertial range, so that the energy-containing eddies which contribute to $\langle u_i u_j \rangle$ are mostly made up of the resolved part, hence the modeled part is much smaller. For a RANS model, $\langle u_i u_j \rangle$ is completely modeled; no part is resolved.

4 State of Literature

Analytical studies of topographical flows began in the 70s with linear models over gently sloping hills [18]. Indeed historically, linear models have been the basis for commercial CFD codes, e.g. AMDS, WAsP,MSFD, and MS3DJH [9]. In 1975, Jackson and Hunt [19] observed a lack of attempts to relate the wind velocity measurements with the local topography. This motivated a model formulation based on a division of the flow into any outer, inviscid layer and an inner layer, where turbulent transfer processes are significant. This linear theory (so-called Jackson-Hunt theory) for terrain-induced flow perturbations over 2D hills was extended to 3D terrain in 1979 by Mason and Sykes, who took surface wind measurements over Brent Knoll, a circular-shaped hill in Somerset, England [20], marking the first experimental study over non-flat terrain. The development of non-linear models began in the mid-70s with 2D and 3D solutions over gently sloping terrain [18]. The Askervein hill project in 1982-83, comprised of two field experiments over a 116 m high hill on the island of South Uist, Scotland. To date, this experiment provides a benchmark case for testing numerical and analytical models for flow over topography [21]. In addition to field experiments, wind tunnel tests of topographical flows continued through the 80s using simple shapes, 2D hills, triangular ridges, and surface roughness elements. Then in the 90s, 3D hills were explored.

LES has been around since the 1960s but computational resources have only facilitated its practical applicability as of fairly recently [16]. In the 90s, LES gained popularity in simulating atmospheric boundary layer (ABL) flows, including investigations into wake dynamics. In 1991, Taylor and Smith [22] performed wind tunnel studies on wakes in ABL flow over a 2D hill. Then in 2014, an LES by Yang et al. modeled flow through a wind farm situated downstream of complex terrain. Although extensive studies have addressed wakes in flat or gently sloping terrain, very few have included complex terrain, and even less have been validated with experimental data [18]. However, one recent study of Shamsoddin and Porté-Agel performed an LES over a 2D hill with and without wind turbines and compared the results to wind tunnel experiments of the same terrain, with promising agreement between the two. Still, further investigations into more realistic terrain are needed [18].

Combining lidar with numerical models has been around since the mid-90s, however more recently, LES and lidar measurements have been integrated to study the turbine near-wake flow and quantify uncertainties [13]. In 2015, Mirocha *et. al* placed virtual lidars within an LES with a turbine actuator disk representation [23]. Different weighting functions within the probe volume of the beam were investigated and their effect on wake parameter estimates. Their results showed reasonable agreement with field data for some of the wake parameters, while others were mis-estimated. They argue that sources of error are due to the coarseness of the LES, limitations of the actuator disk representation, and the lidar sampling approach. Finally, lidar scanning uncertainty has been investigated in an LES by Doubrawa *et al.* in 2016, with the error of wake characteristics quantified by comparing those characteristics determined by temporally disjunct synthetic lidar scans to those determined by LES mean fields and instantaneous fields. The same study investigated scan geometry and found that the scan area (coverage) was important in estimating the wake center, orientation and length scales, while the scan point density was important in determining the velocity deficit [13]. This provides a logical starting point for the present project to begin testing scanning geometries while providing direction on how to quantify uncertainty.

5 Setup

In this section the formulation of the LES code and processing of Galion data is introduced, as well as the steps in obtaining synthetic lidar fields from the LES.

5.1 LES

Figure 16 shows the extent of the LES domain along a streamwise transect passing through the turbine axis. The wake is visible, as well as recirculation zones downstream of the ridges. Figure 17 shows a sub-region of this transect, which formed the domain used for wake analysis throughout the rest of this study. Reducing the size of the domain greatly reduced computational times. Although due to turbulent mixing, the wake is only studied at downstream distances less that four diameters, a view of the wake extending 7 diameters downstream is given in Figure 18, illustrating the turbulent mixing of the wake with the terrain-generated turbulence. Figures 19 and 20 show plan views of the full domain and sub-domain, respectively. The standard deviation of the streamwise component in Figure 19 clearly identifies two ridges and the resulting increase in turbulence intensity. The ensemble-average of 8 30-minute averaged u fields in Figure 20 also highlight the low-momentum region behind the ridge.

The LES wind is driven by a constant pressure gradient $dP/dx = -u_*^2/z_{max}$, set to act in the direction perpendicular to the two ridges, and generate high wind speeds to simulate neutrally stable atmospheric conditions. z_{max} is the domain height of 3000 m, and u_* is the friction velocity, taken as 0.6 ms^{-1}.

5.1.1 LES Code

The LES uses the NCAR pseudo-spectral code of Patton [24]. Subgrid-scale stresses are parameterized according to Deardoff's model [25], utilizing eddy viscosity for the momentum and temperature fluxes, and Lilly-Kolmogorov model for viscous dissipation. Dynamic time stepping is performed with fixed Courant–Fredrichs–Lewy (CFL) number. The LES flow variables of interest to this study are u (streamwise),v (transverse), and w (vertical).

5.1.2 Mesh

The terrain surface forms the lower boundary of the domain and has height $h = h(x, y)$. Terrain shape has been smoothed from its true value using an exponential filter in wave number space, as in [4], with maximum slope ≤ 0.77. This greatly reduces the number of iterations to solve the Poisson equation for pressure and keeps computational times manageable. Terrain-smoothing has shown to strongly affect the size and position of the recirculation zone behind the first ridge [4], and is thus a major candidate for inaccuracies of the LES, however for the purposes of comparing wake characterization methods it is deemed acceptable.

In order to properly compute the derivatives in the filtered LES equations, a mapping of the physical space coordinates $x_i = (x, y, z)$ to the computational domain coordinates $\xi_i = (\xi, \eta, \zeta)$ is performed. The computational grid is terrain-following and non-orthogonal. The x and y gridlines are regularly spaced and $\Delta x = \Delta y$. Horizontal gridlines are squeezed near the surface and stretched moving upwards, so that resolution is highest near the surface. Figure 21 illustrates the stretching of horizontal gridlines, i.e. lines of constant ζ, shown at every four lines for visualization. Properties of the domain including number of cells N_i in each direction and physical domain size

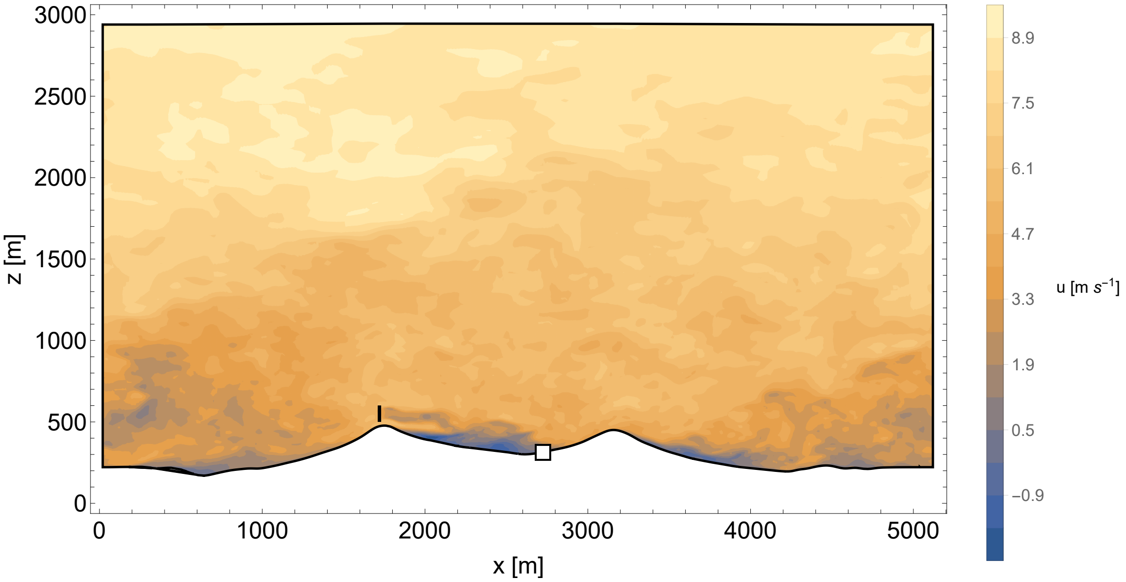

Figure 16: Instaneous LES u field, covering the extent of the domain in the x (streamwise) and z (vertical) directions. The lidar and turbine rotor positions are marked by a white square (enlarged) and vertical black line, respectively.

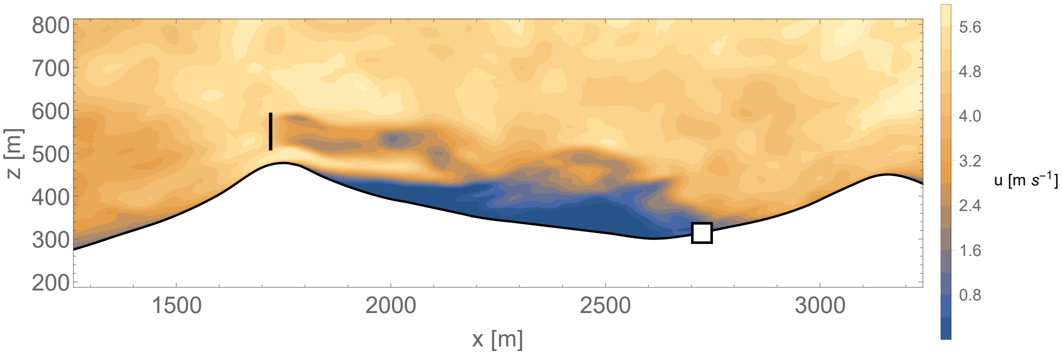

Figure 17: Wake visualization using instantaneous LES u data. The lidar and turbine rotor positions are marked by a white square (enlarged) and vertical black line, respectively.

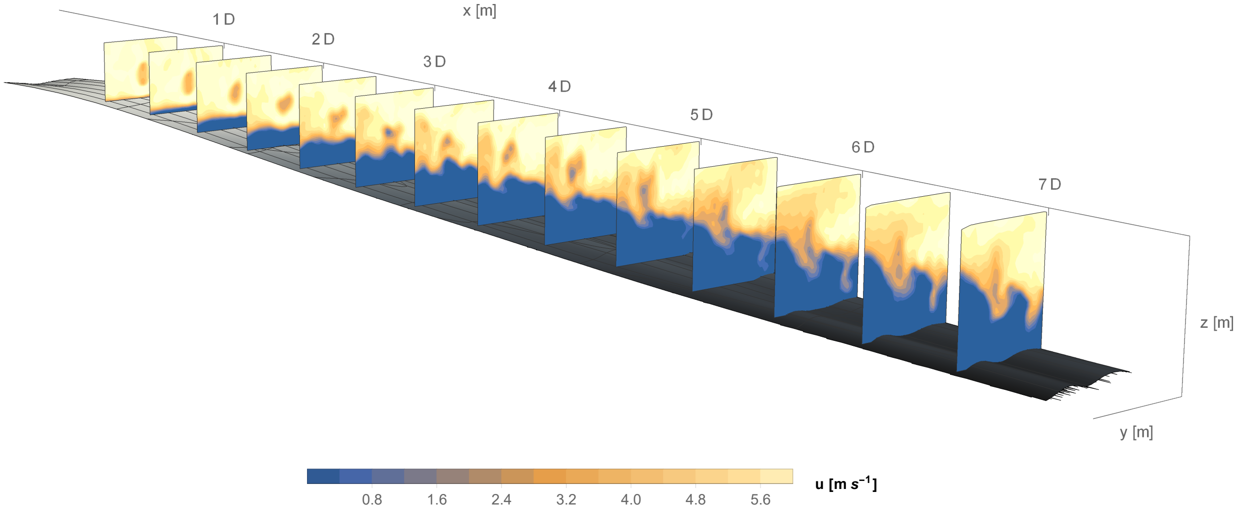

Figure 18: Cross-planes of instantaneous LES field data downstream of the turbine

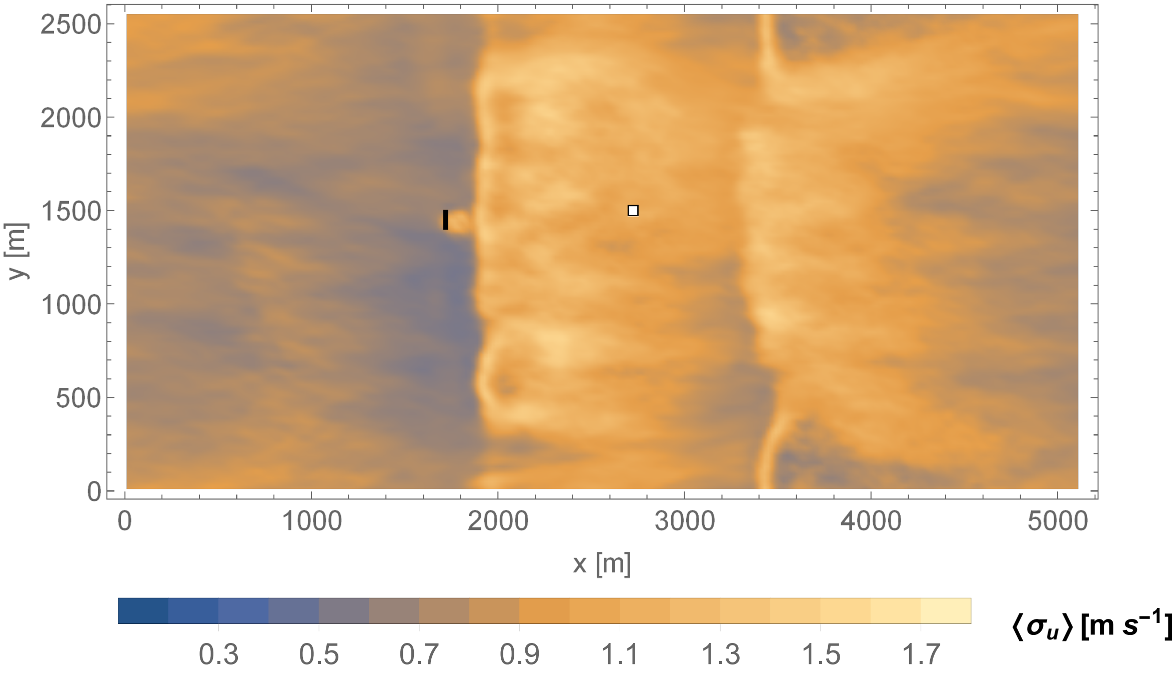

Figure 19: Ensemble average of 8 30-minute σ_u fields at hub height

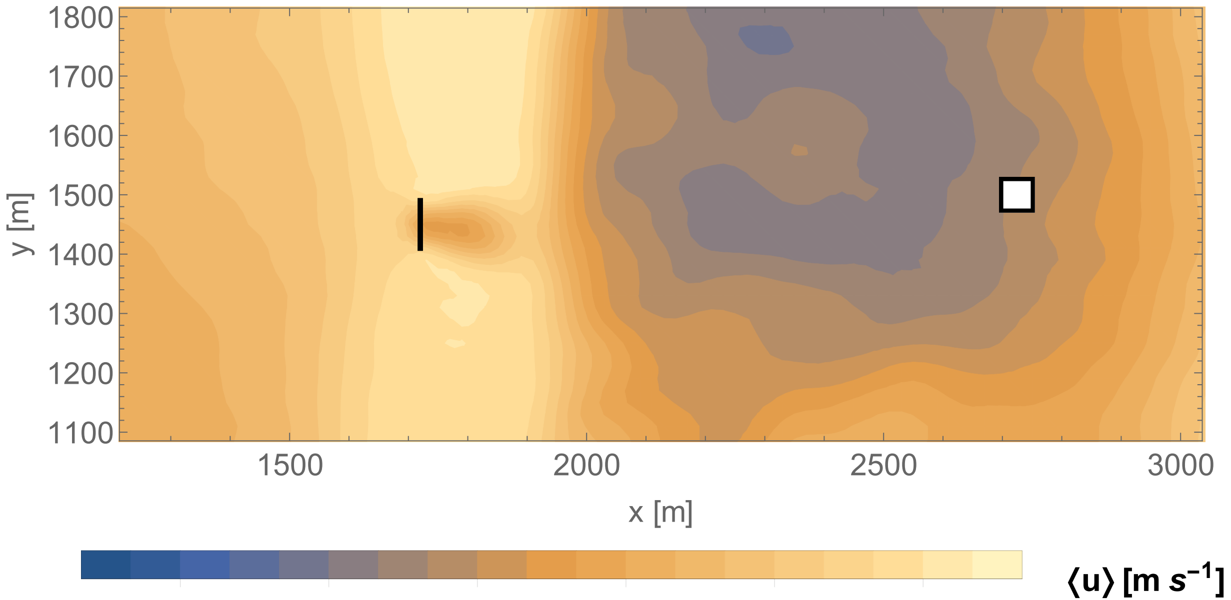

Figure 20: Ensemble average of 8 30-minute averaged u fields at hub height

are given in Table 3. The arrangement of variables within a computational cell is shown in Figure 22. The Cartesian velocity components (u,w) are located at the cell center and (v) is pointing into the page. Also pictured are the pressure p^*, potential temperature θ, subgrid-scale energy e, and contravariant flux velocities U and W.

5.1.3 Spatial filter

The filter function G, mentioned in Section 3.5, takes the form of a sharp cut-off filter in wave number space and the filter width Δ is computed from the cell volume $\Delta^3 = (3/2)^2(\Delta\xi\Delta\eta\Delta\zeta/J)$ where J is the Jacobian and $3/2$ is the factor accounting for de-aliasing. Because of the grid stretching, Δ varies with cell position.

5.1.4 Boundary conditions

Horizontally periodic boundary conditions are maintained by adding a buffer zone to the edges of the domain [4]. At the upper boundary, a no stress condition is enforced, where gradients in the horizontal velocities are equal to zero and there is no vertical velocity component.

5.1.5 Turbine model

The turbine is modeled as an actuator disk, non-rotating, and with constant yaw angle so that the axis is aligned with the x (streamwise) direction. The turbine radius is 40 m and hub height 80 m. The following description follows that of Berg *et. al* 2017 [4]. The thrust force the disk exerts on the wind is

$$F_t = -\frac{1}{2}\rho C_T' \langle\overline{u}\rangle_d^2 \frac{\pi}{4} D^2.. \tag{5.1}$$

Table 3: LES computational domain properties

N_x	256 cells
N_y	128 cells
N_z	128 cells
Phys. x range	5120 m
Phys. y range	2560 m
Phys. z range	3000 m
$\Delta x = \Delta y$	20 m
Temporal Resolution	0.8 s
Sampling Rate	$\Delta t = 1.6\ s$
Number of 30 min. time-averaged fields	45
Number of 30 min. standard deviation fields	45
Number of instantaneous fields	$N_s = 4000$
Total Simulation time	$T_{LES} = N_s \times \Delta t = 1.78$ hours

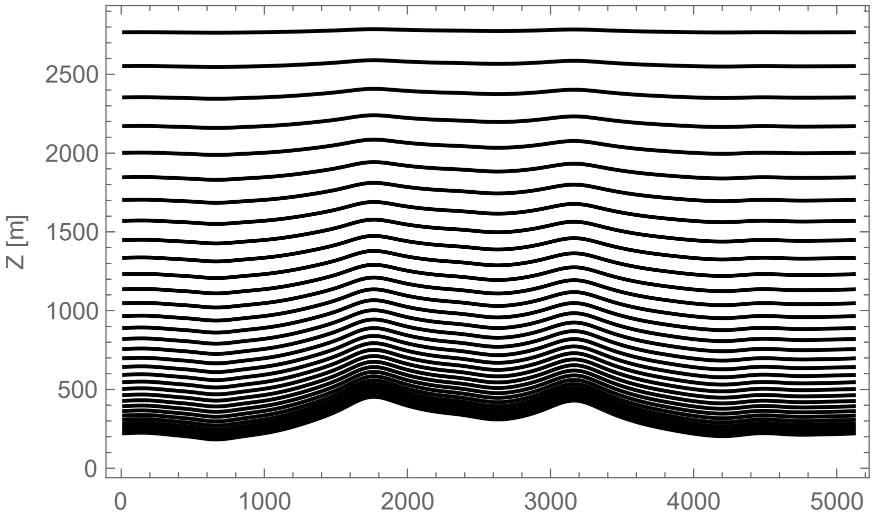

Figure 21: LES domain, lines of constant ζ, shown every fourth line for visualization.

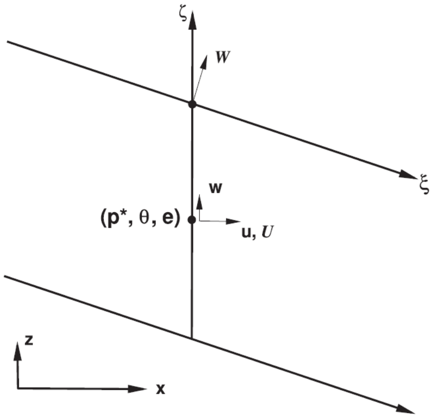

Figure 22: Location of flow variables on an LES computational cell

where D is the rotor diameter, $\langle \overline{u} \rangle_d^2$ is the streamwise wind speed, averaged over the rotor area. C_T' is related to the thrust coefficient by 1D momentum theory by

$$C_T' = \frac{C_T}{(1-a)^2} = \frac{4a}{1-a} \tag{5.2}$$

where a is the axial induction factor, chosen to be 1/4.

5.1.6 Coordinate System

As shown in Figure 7, the x and y directions are chosen so as to be approximately perpendicular and aligned with the ridges, respectively and right-handed $x - y - z$ coordinate system has its origin at the bottom corner of the domain. The positive y-direction runs 41^o west of due North. As a consequence of the pressure gradient of Section 5.1.1, the mean wind flows in the positive x direction.

5.1.7 Additional assumptions & limitations

- No stability effects such as surface heating or cooling are modeled, so that the field most closely simulates neutrally stable conditions.
- Compared to the ridge sizes, the LES domain is small (seen in Figure 5) and doesn't capture the surrounding orography, roughness changes, etc.
- As mentioned in Section 3.5, Coriolis and buoyancy forces are neglected.

5.2 Lidar

5.2.1 Galion data

The Galion data consists of a single lidar scan, around 10 minutes, and was selected from a larger set of scans from different times and different days. Data from a Perdigão met-mast, located 200 meters from the turbine location, was available for each day of Galion measurement, and at multiple times during day. This allowed selection of a scan with high wind speeds (8.3 ms^{-1} at 100 m) to approximate neutral stability conditions, and a mean wind direction approximately perpendicular to the ridges at 235.6^o (south-westerly).

5.2.2 Additional assumptions & limitations

As mentioned in Section 3.3, lack of spatial homogeneous conditions in complex terrain do not allow for determination of wind direction from a singe lidar. It should be noted that spatial homogeneity is also an implicit assumption of the data acquisition of real lidars, which sample the wind field inside the measurement volume over a period of time to get an average speed. This assumes the wind speed distribution is equal everywhere in the volume (spatially homogeneous). However in practice, this volume is small and is therefore not considered a significant source of uncertainty. Furthermore in this study, the synthetic lidar simply samples individual points in the LES, linearly interpolating the LES velocity from neighboring points (detailed in Section 6). A filter function is then not used on account of insufficient LES spatial resolution.

Design of scan geometries is constrained by the range of possible azimuthal and elevation angles achievable by the Galion, as well as the scanner head speed and sampling rate, which were kept constant for all geometries tested.

5.3 Coordinate Transformations

The coordinate system used by the lidar is given in section 3.3. In order to transform lidar scan point locations to LES coordinates, one first needs the lidar location in LES coordinates. The information given in Table 4 is utilized for this transformation.

$$\begin{bmatrix} \cos(\psi) & \sin(\psi) \\ -\sin(\psi) & \cos(\psi) \end{bmatrix} \begin{bmatrix} x_{L,T} \\ y_{L,T} \end{bmatrix} = \begin{bmatrix} x_L - x_T \\ y_L - y_T \end{bmatrix} \tag{5.3}$$

where $\{x_L, y_L\}$ is the lidar position and $\{x_T, y_T\}$ the turbine position in LES coordinates.

To find lidar scan point locations in the LES coordinate system, first the points are transformed from polar θ, ϕ, r to cartesian coordinates $\hat{x}, \hat{y}, \hat{z}$ in the lidar coordinate system, where the positive $\hat{x}$-axis aligns with the $\theta = 0, \phi = 0$ direction, given as

$$\hat{x} = r\cos(\phi)\sin(\theta) \tag{5.4}$$

$$\hat{y} = r\cos(\phi)\cos(\theta) \tag{5.5}$$

$$\hat{z} = r\sin(\phi) \tag{5.6}$$

The lidar measurement locations can be transformed from lidar to LES coordinates as

$$\begin{bmatrix} \cos(\psi) & \sin(\psi) \\ -\sin(\psi) & \cos(\psi) \end{bmatrix} \begin{bmatrix} \hat{x} \\ \hat{y} \end{bmatrix} = \begin{bmatrix} x - x_L \\ y - y_L \end{bmatrix}, \qquad z = \hat{z} + z_L, \tag{5.7}$$

where z_L is the lidar vertical position in LES coordinates, taken to be equal to the ground height at (x_L, y_L).

5.4 Verification of LOS Speed Retrieval

A verification was performed of the algorithms written for retrieving synthetic lidar measurements. These algorithms consist of coordinate system transformation of position and velocity from LES to lidar coordinates, and subsequent projection of the velocity onto the LOS direction to calculate the radial velocity (seen by the lidar). This verification is carried out by the generation of several

Table 4: Turbine and Galion information

Galion Location WRT Turbine $\{x_{L,T}, y_{L,T}\}$	[717, 676] m Easting, Northing from turbine
Turbine Location $\{x_T, y_T\}$	[1720, 1460] m
Turbine Hub Height	80 m
Turbine Radius	40 m

fictitious wind fields, which are uniform and/or varying in time and space. These fields are imposed within the LES environment, i.e. the terrain, lidar position are kept, but without any simulation of the real flow (see Figure 23).

The verification consists of the lidar retrieving LOS speeds u_r at five points in the flow, and for three test cases. This is carried out in the following steps:

1. First, four cases of uniform flow fields are generated. In LES coordinates:

$$\{u, v, w\} = \begin{cases} \{1,0,0\} & \text{Case 1.1} \\ \{0,1,0\} & \text{Case 1.2} \\ \{0,0,1\} & \text{Case 1.3} \\ \{3,2,1\} & \text{Case 1.4} \end{cases} \tag{5.8}$$

   To test the lidar retrieval in a spatially varying wind field, a logarithmic wind shear profile was applied at every (x, y) location in the domain. The log-law profile, given in Equation 5.9 has a stream-wise component only.

$$\text{Case 1.4:} \qquad u(z) = \frac{u_*}{\kappa} \log \frac{(h)}{z_0} \tag{5.9}$$

   To test a time and space-varying velocity field, a time-varying log profile is applied through Equation 5.10

$$\text{Case 1.5:} \qquad u(z) = \cos(\omega t) \frac{u_*}{\kappa} \log \frac{(h)}{z_0} \tag{5.10}$$

   where $u_* = \sqrt{-\langle u'w' \rangle}$ is the friction velocity (taken as 0.6 ms^{-1}), κ the von Kármán constant (0.4), h is the height above ground, and z_0 the roughness length, taken as 0.5 m.

2. Select 5 different points in the flow to probe. The locations of these points with respect to the terrain, lidar, and rotor disk are give in Figure 23.

   - Points **(1-4)** are distance d from the lidar, measured along the x and y axes, and at a height l above the lidar. Therefore a constant elevation angle $\phi = \beta$ is kept.

   - Point **(5)** is directly above the lidar ($\phi = 90^o$), at a height l.

   For each case, perform Steps 3-6.

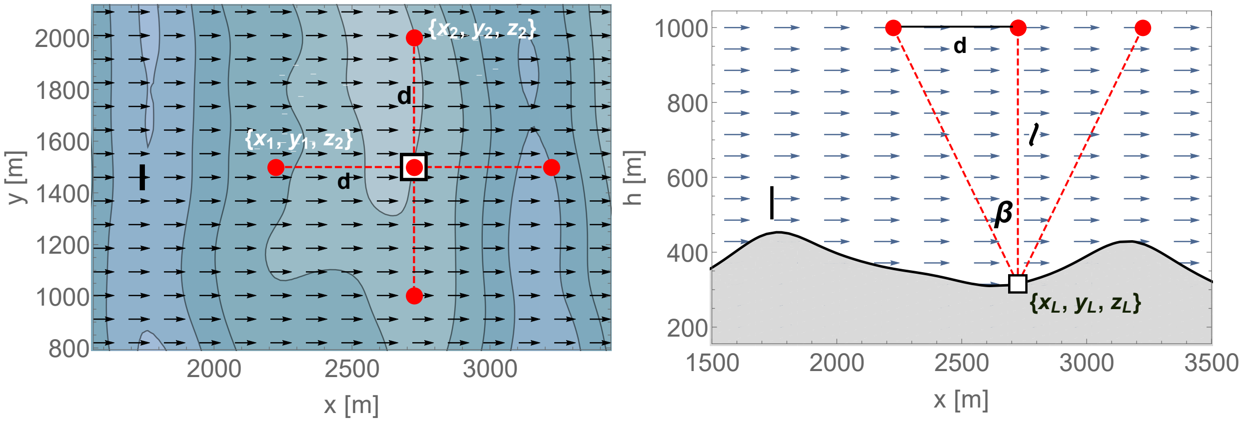

Figure 23: Scanning locations within verification wind field with $\{u, v, w\} = \{1, 0, 0\}$ from top view (left) and side view (right).

3. Transform Cartesian velocity of scan points in LES coordinates to Cartesian velocity in lidar coordinates $\{\hat{u}, \hat{v}, \hat{w}\}$ by solving the matrix equation

$$\begin{bmatrix} \cos(\psi) & \sin(\psi) \\ -\sin(\psi) & \cos(\psi) \end{bmatrix} \begin{bmatrix} \hat{u} \\ \hat{v} \end{bmatrix} = \begin{bmatrix} u \\ v \end{bmatrix}, \qquad w = \hat{w}, \tag{5.11}$$

   where the rotation matrix rotates points in the xy-plane by $\psi = 41^o$, counter-clockwise. This corresponds to the angular displacement of the domain from the cardinal directions (see Figure 7), in which lidar coordinates are aligned.

4. Transform scan point locations in LES coordinates to Cartesian lidar coordinates via Equation 5.7.

5. In lidar coordinates, compute the scalar projection of the velocity onto position vector to get the magnitude in the radial direction, or LOS speed, defined positive away from the lidar.

$$u_r = \frac{\{\hat{u}, \hat{v}, \hat{w}\} \cdot \{\hat{x}, \hat{y}, \hat{z}\}}{|\{\hat{x}, \hat{y}, \hat{z}\}|} \tag{5.12}$$

6. Compare this with the result of using only LES coordinates, that is projecting the LES velocity onto the LES position vector from lidar to scan point, $\{x - x_L,\ y - y_L,\ z - z_L\}$.

$$u_r = \frac{\{u, v, w\} \cdot \{x - x_L,\ y - y_L,\ z - z_L\}}{|\{x - x_L,\ y - y_L,\ z - z_L\}|} \tag{5.13}$$

This procedure verified that for all 4 cases and 5 scan points, both the transformations produced equivalent LOS speeds.

5.5 Galion data conditioning

The lidar data collected by the Galion at Perdigão has several spurious readings, which can be caused by hitting hard targets such as the turbine and terrain, or cloud water, for example [13]. These spurious readings can be seen at the far tails of the velocity distribution, shown for a single scan in Figure 24. Therefore, readings of $-20 \geq u_r \geq 20$ m s^{-1} were considered unphysical and filtered out prior to processing.

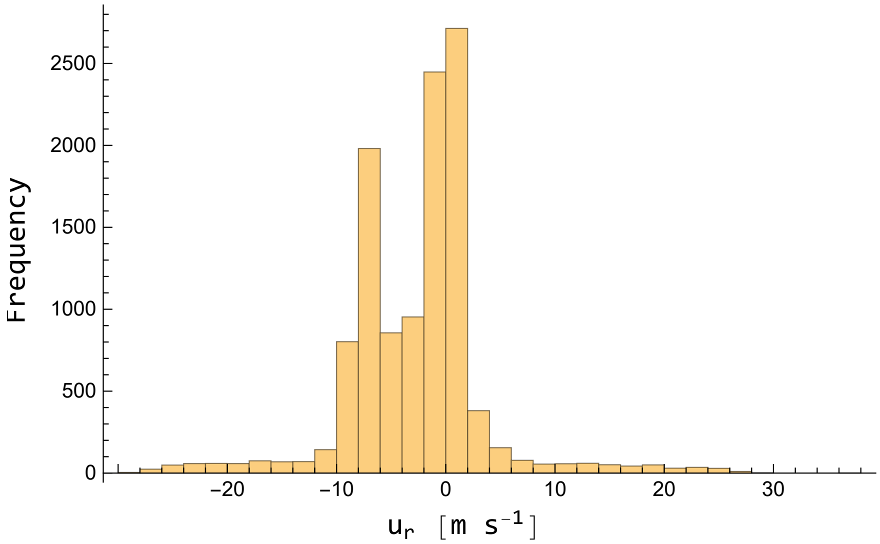

Figure 24: Histogram of LOS velocity from the Galion over a single scan

5.6 Retrieval of Synthetic Lidar Velocities

This algorithm is key to the process of retrieving the velocities seen by the lidar. For this process, the LES data must be sampled at times t_s corresponding to lidar measurement times and only at the locations at which the lidar is measuring at time t_s. The steps are outlined as follows:

1. **Calculate u_r from LES Velocity Field:** For each LES snapshot (at time t_L), calculate u_r from the LES velocity field via Equation 5.13.
2. **Interpolate LES Fields in Space:** For each LES snapshot, calculate a function to interpolate in space and find the velocity u_r at the lidar scan point locations.
3. **Interpolate In Time:** Now each instantaneous LES field is interpolated linearly in time. The interpolation function interpolates u_r at a lidar scan time t_s, from the already determined u_r values at LES times t_L. Each interpolation is performed only for the lidar scan points with temporal coordinate t_s falling between the consecutive LES snapshot times t_{L-1} and t_{L+1}.

The resulting cloud of synthetic lidar measurements is visualized in Figure 25.

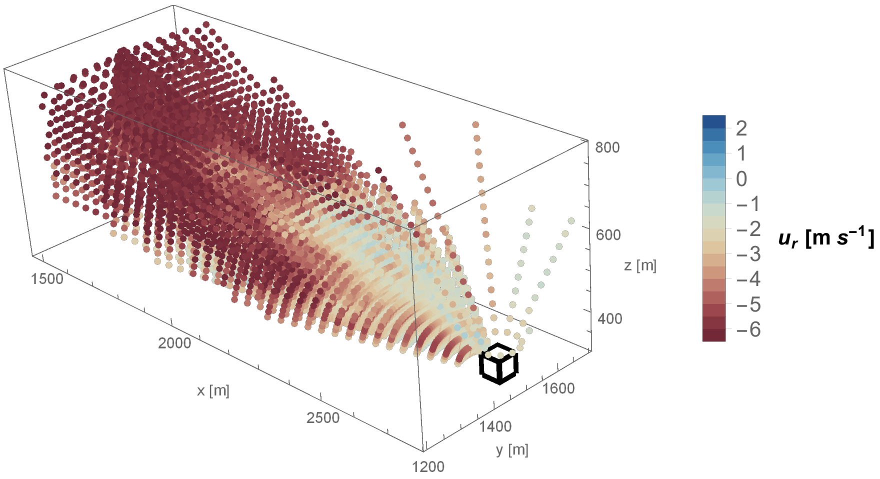

Figure 25: Visualization of synthetic lidar data points and lidar position (lidar size exaggerated for visualization)

6 Wake Detection

In order to determine the shape and location of a wind turbine wake, a method is needed to distinguish the points lying within the wake from those in the undisturbed flow. A typical wake characterization is to use the horizontal wind speed $U = \sqrt{u^2 + v^2}$ and compute the velocity deficit as

$$U_d = 1 - U(y, z)/U_\infty(z) \tag{6.1}$$

where the undisturbed velocity profile $U_\infty(z) = \sqrt{u_\infty^2 + v_\infty^2}$ is usually taken at a location far away from the turbine, in horizontally homogeneous terrain, and so $U_\infty(z)$ is approximately logarithmic. U_d is calculated along a profile extending vertically (z-direction) or horizontally (y-direction) through the wake (perpendicular to the turbine axis) or in vertical cross-sections (yz-planes) at several downstream distances. The shape of the U_d distribution across the wake is then typically fit with a Gaussian curve to locate the wake center. The center can be defined as the maximum of the Gaussian, for example, or, as in [13], the center of gravity of the U_d distribution. The wake edge location is often determined by where the wind returns close to its undisturbed speed, by applying the criteria of $U(y, z)/U_\infty(z) = 0.95$ for example, or by using the 95% confidence interval ($2\ \sigma$) of the Gaussian fit [13]. Alternatively, a finite difference scheme could used to calculate the velocity gradients $dU/dx, dU/dy, dU/dz$ and the vicinity of the wake center searched to find where their magnitudes are highest.

6.1 In Complex Terrain

The aforementioned methods become more challenging with the influence of complex terrain, wherein steep gradients induce turbulence that mixes into the wake, and wherein the wake deflects away from the turbine as it follows the slope. The former makes wake edges more challenging to identify, as the velocity deficit due to the wake is not clearly differentiable from that of the terrain, while a wake which follows the terrain also makes the wake center location less predictable.

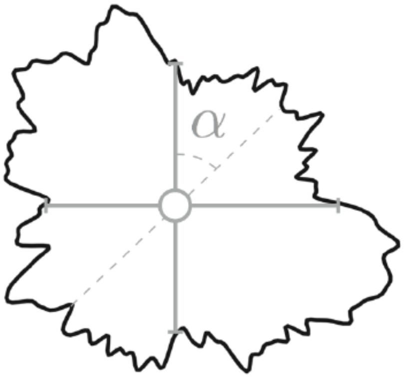

Figure 26: Taken from [13]. Schematic of wake metrics, including width and height, center, and orientation (angle α from vertical).

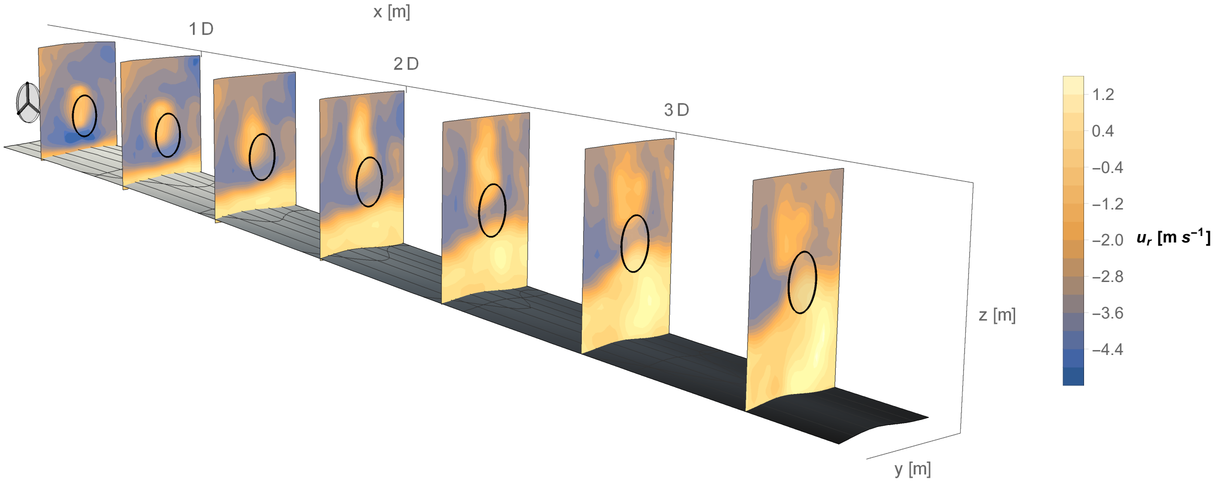

Figure 27: Instantaneous LES data of u_r. Black circles indicates (y, z) location of turbine rotor.

Both effects also distort the shape of the wake, making a Gaussian fit less accurate. This can be observed with an instantaneous field from the LES data in Figure 27. Downstream slices taken every $0.5D$ show the low-momentum air of the wake above that of terrain turbulence. After approximately $2.5D$, these low-momentum regions mix together. Also evident is the distortion of the wake shape from nearly circular close to the turbine to vertically-elongated downstream at $1.5D$

6.2 By A Single Lidar

In addition to distortion from the terrain, using a single lidar adds a significant challenge to accurately determining wake characteristics. Compared to the Perdigão LES, the Galion scan geometry has a lower resolution by $0.125D$ in the lateral directions and $0.3125D$ in the vertical (at hub height). In terms of temporal resolution, as mentioned, a lidar scan is temporally disjunct, and the measured wake shape is distorted by this effect. In this respect, the geometry of the scan is of critical importance. Geometries with more points will have higher spatial resolution, but the

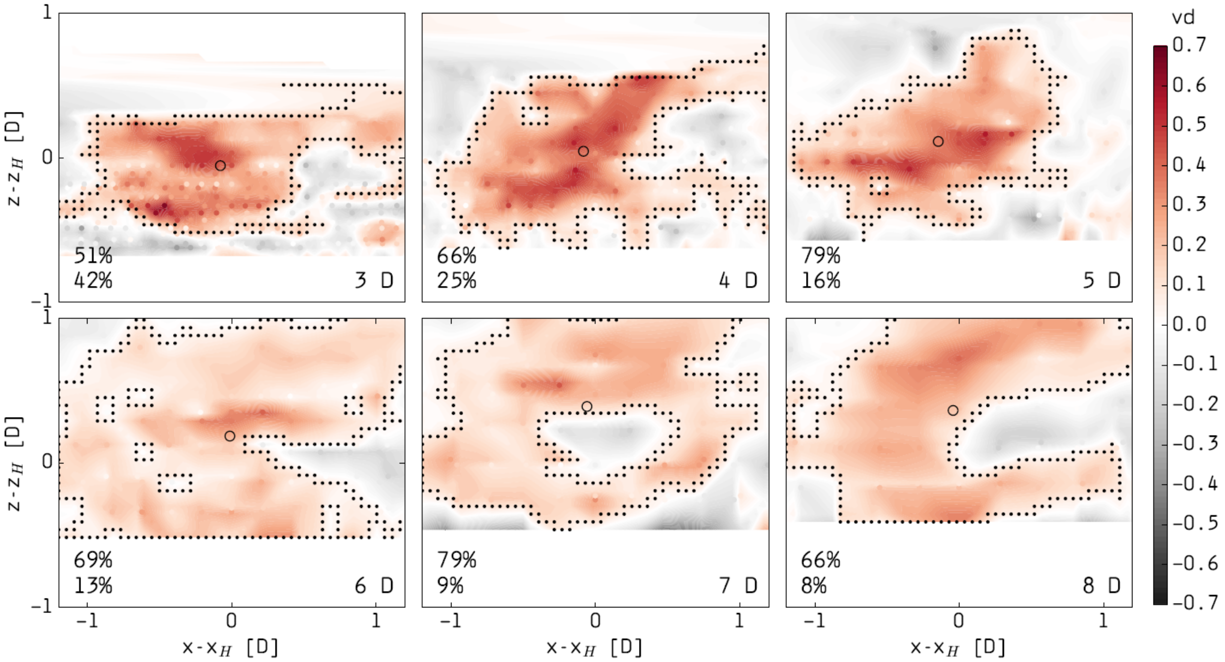

Figure 28: Taken from a previous study [13]: velocity deficit for field measurements (colored dots) and their linear interpolation onto a rectangular grid (shaded contours) at different downstream distances. The wake edges (black dots) and center (circle) are marked.

added scan time distorts the wake shape further. Conversely, geometries with less points are better resolved in time but with less spatial resolution, a trade-off crucial in determining wake shape and location.

6.3 Previous Studies

Previous studies have used single lidars to characterize the wake however, to the best of the author's knowledge, not in complex terrain environments. Doubrawa, Barthelmie, Wang, Pryor and Churchfield (2016) [13] performed a study in non-complex terrain, benefiting from a negligible vertical velocity component to determine both horizontal wind components. To characterize the wake in that study, vertical slices of lidar points were obtained at specific downstream distances by selecting all points lying at the selected distance and falling within a buffer Δx in the streamwise direction. These points were then interpolated onto a rectangular grid to form yz-planes in which the wake could be measured. The velocity deficit was then calculated, along with the wake center and edges. Fitting an ellipse to the wake edges, a wake orientation was defined, shown in Figure 26. An example of wake edge and center detection from U_d by [13] is shown in Figure 28, with the outline of the wake shape visible, along with the wake center.

As will be shown in the following sections, the addition of sloping terrain will necessitate other methods to differentiate the low-momentum air of the wake from that of the terrain-induced turbulence.

6.4 Interpolation Methods

The lidar scan points are scattered in space and need to be interpolated onto a regular grid, oriented perpendicular to the mean wind direction. Several options are available for interpolating, including nearest neighbor (zeroth order interpolation), linear interpolation (first order), and higher-order splines. For the sake of simplicity, only nearest neighbor and linear interpolation were compared.

6.4.1 Location of Interpolation Planes

Before the interpolation is carried out, the location of each yz-plane to be interpolated onto is determined as well as the resolution of the plane grid. The vertical and cross-stream coordinates of the planes were chosen to be held constant, and were selected (as were the downstream locations) based on predicted wake positions from inspecting the ensemble-averaged fields. Figures 29 to 34 show the four-hour ensemble-averaged LES field of u and u_r and their standard deviations. These informed the positioning of the interpolation planes shown in dashed lines in each figure, with only every other plane shown, for visibility.

Figures 29 and 30 show the ensemble-averaged u fields of the LES. The vertical transect of Figure 29 shows the ensemble-averaged position of the wake in the vertical and streamwise coordinate, as well as the ensemble-averaged low-momentum wake of the ridge. The cross-stream planes in Figure 30 provide information on the average lateral dimensions of the wake and deflection from the turbine axis.

In addition to the averaged position of the wake, LES fields of σ_u were used to estimate the spatial variability of the wake. The vertical transect of Figure 31 was used to observe the spatial variability of the wake in the vertical and streamwise direction, and the cross-stream planes of Figure 32 to observe the same in the lateral direction.

Although the streamwise component u is a reliable indicator of wake position, the lidar measures only the radial component u_r, and so the ensemble averaged u_r fields (Figures 33 and 34) were also used for positioning the interpolation planes. These plots show agreement with the u fields in terms of wake position, while the flow at higher altitudes and closer to the lidar (higher lidar elevation angles) shows the effect of visualizing the radial component only. This occurs because at high elevation angles, the angle between the wind vector (u, v, w) and lidar position vector (r, θ, ϕ) becomes large and less of the wind vector is able to be projected onto the LOS direction.

From these fields, the locations and dimensions of the interpolation planes were chosen as given in Table 5, where (y_t, z_t) are the cross-stream and vertical coordinates of the turbine hub. For the purposes of locating downstream planes, a new coordinate has been invoked, x^+, which is parallel to x but with origin at the turbine hub. Figure 29 shows these interpolation planes as well as a slice of lidar points of constant azimuth for one of the geometries tested. Note that for this geometry, at $(x^+/D \geq 3)$, the coverage of lidar points does not extend higher than the top third of the interpolation plane, rendering this region of the plane inadequate for wake measurement using synthetic lidar. A grid of points to be interpolated covers each plane with separation $\Delta y = \Delta z = 10$ m

With the interpolation planes defined, the two interpolation methods are described below:

Table 5: Position and dimensions of interpolation planes for wake parameterization

Downstream Locations	$x^+/D = 0.5, 0.75, 1, 1.25, .., 3.5$
Cross-stream Dim.	$y_t - 2D$ to $y_t + 1.5D$
Vertical Dim.	$z_t - 0.7D$ to $z_t + 2D$
Interpolation Grid Resolution	$\Delta y = \Delta z = 10$ m

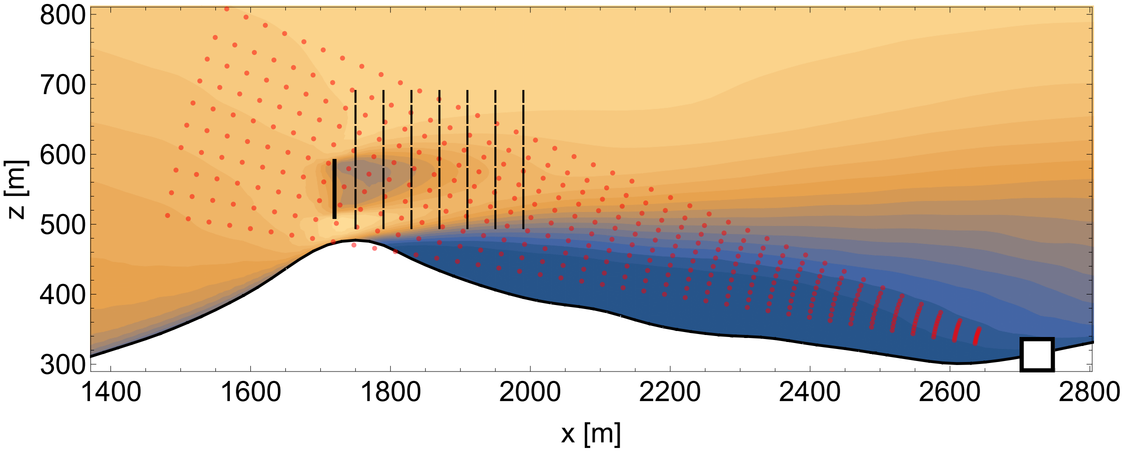

Figure 29: Turbine axis aligned four hour ensemble-averaged u with interpolation plane locations (only every other plane is shown)

Nearest Neighbor: For each grid point in the plane, calculate the distance to every lidar scan point. Find the closest (Euclidean distance) scan point and its velocity, then adopt that velocity at the grid point.

Linear Interpolation: Linear interpolation of the scatterd 3D lidar points is performed with *Mathematica*'s [26] "Interpolation" function, which uses Delaunay triangulation to interpolate at each location. In this method, each query point (point to be interpolated) is enclosed in a triangle, the vertices of which are the 3 closest known data points. Then the weighted sum of the values of the three vertices are computed at the query point. This is repeated for all query points in the plane.

A comparison of these two methods is given in Figure 35, which shows interpolation planes of synthetic lidar data. Similar shape and velocity deficit of the near wake is observed in the two cases, as is the location of the maximum velocity deficit (marked with an "X"), although the linear interpolation better preserves the rounded wake edges, as it uses more data in computing each query point. For this reason, the linear interpolation method is used in the remainder of the analysis.

6.5 Determination of Reference Velocity

Also, in order to compare the wakes in the LES with those of the Galion field data, a suitable reference velocity is needed by which the velocity can be normalized. Since an undisturbed velocity profile such as $U_\infty(z)$ in Equations 6.1 doesn't exist at Perdigão, another reference velocity is needed

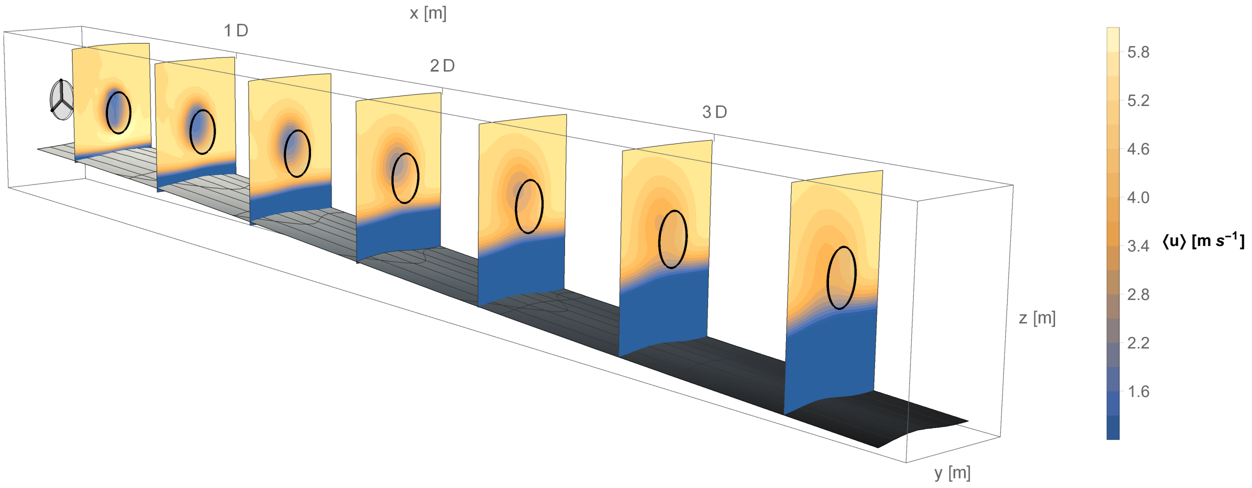

Figure 30: Cross-stream slices of four hour ensemble-averaged u

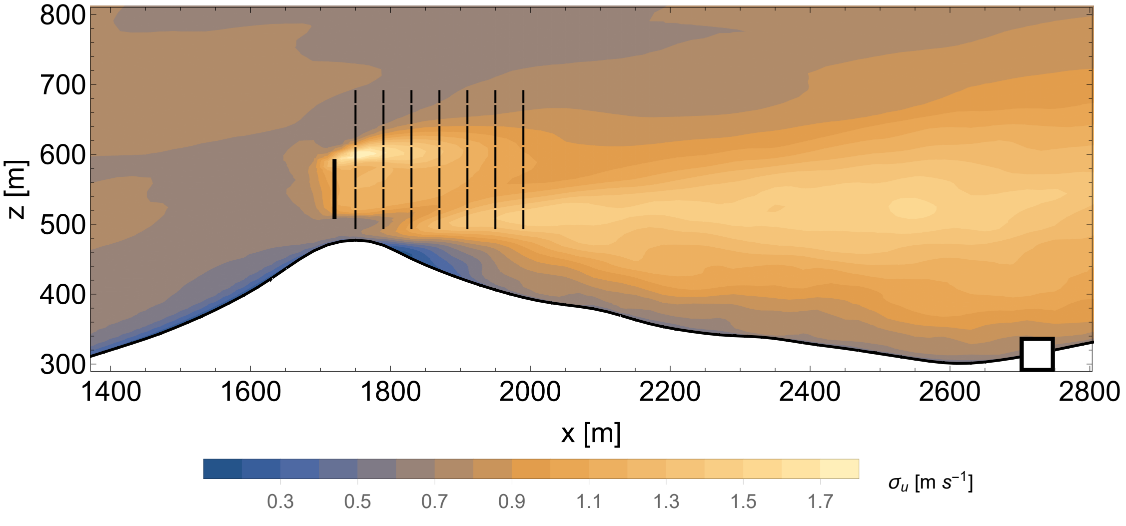

Figure 31: Turbine axis aligned transect of four hour ensemble-averaged σ_u

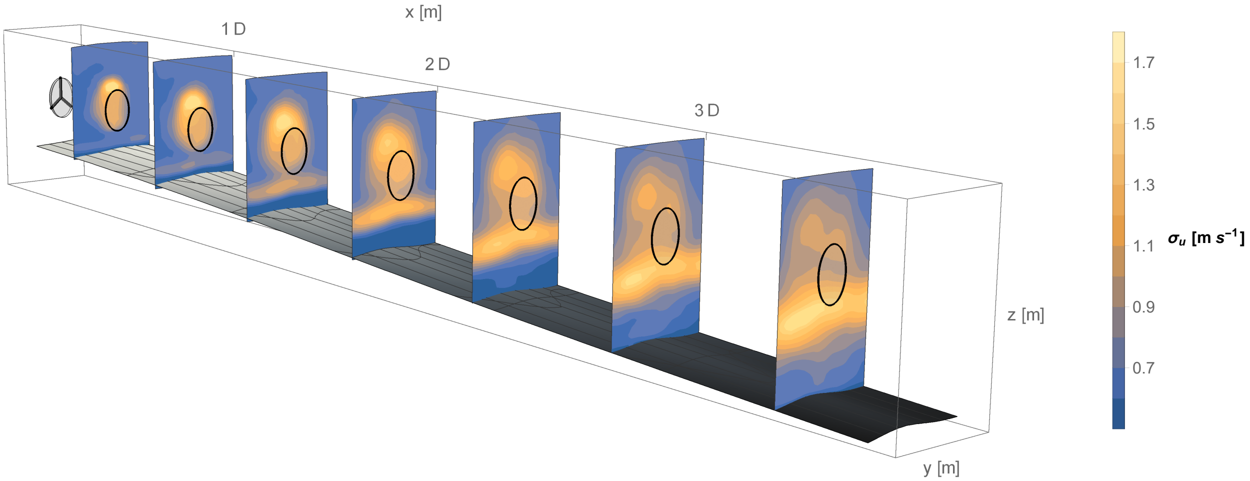

Figure 32: Cross-stream slices of four hour ensemble-averaged σ_u

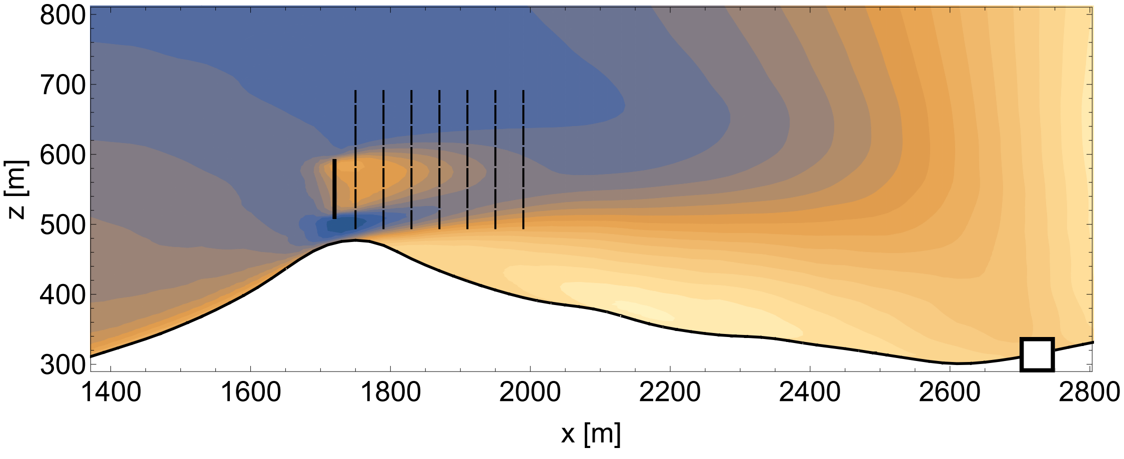

Figure 33: Turbine axis aligned transect of four hour ensemble-averaged radial velocity with interpolation plane locations (only every other plane is shown)

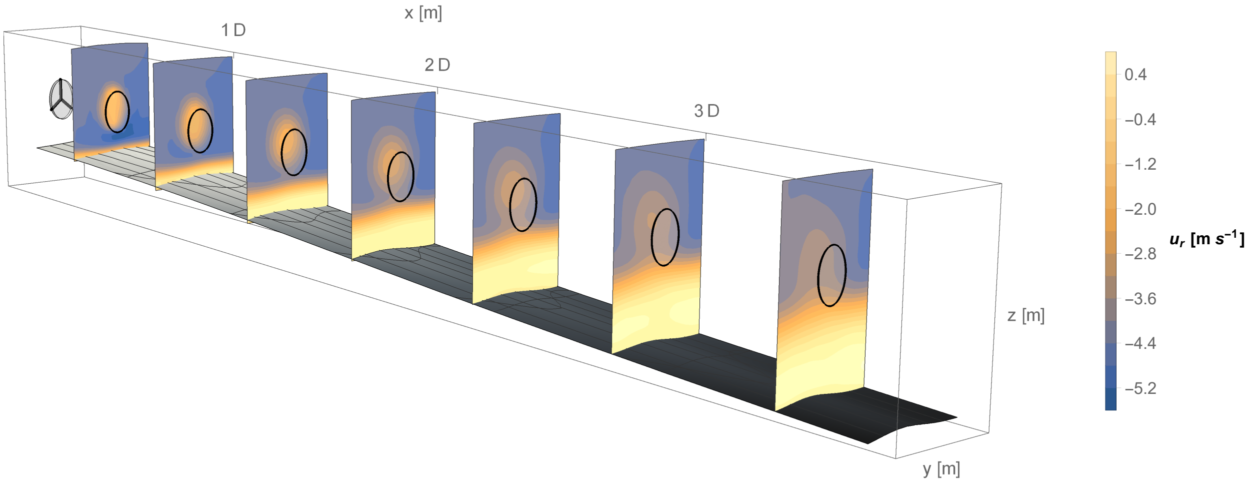

Figure 34: Cross-stream slices of four hour ensemble-averaged radial velocity

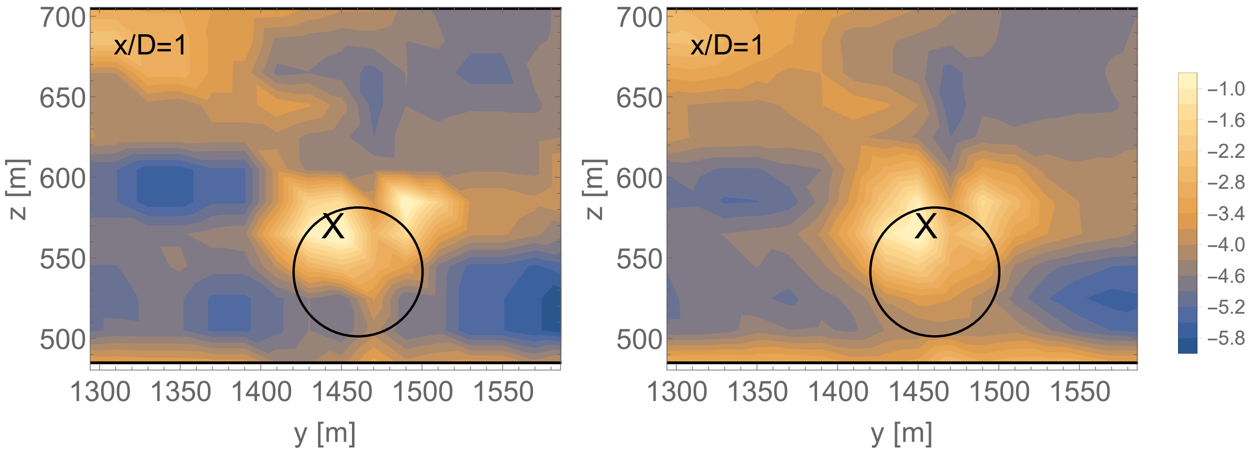

Figure 35: Comparison of interpolation methods for synthetic lidar. Left: nearest neighbor; Right: linear interpolation

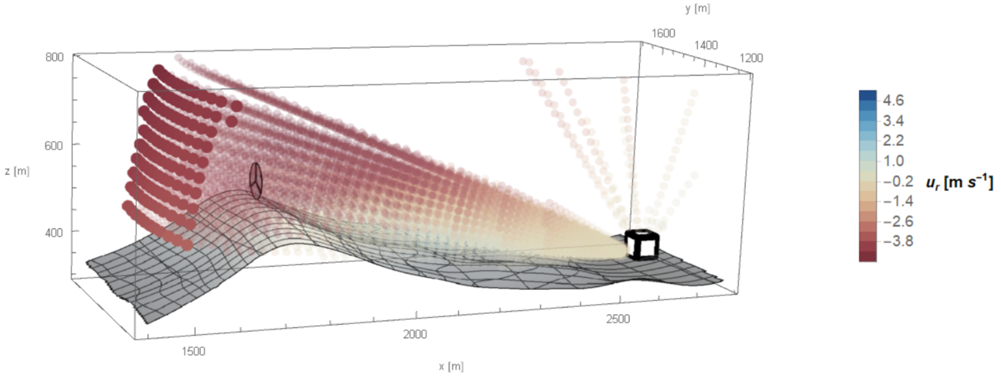

Figure 36: Scan point locations (solid dots) used to determine reference velocities $u_{\infty,LES}$ and $u_{\infty,GAL}$ for the geometry shown.

for normalization. Normalizing the velocities in the LES and Galion data make the wake characteristics less dependent on modeling errors. In flat terrain, a point far upstream or downstream of the turbine is typically chosen as representing the undisturbed or free-stream wind speed. In complex terrain, the flow is always influenced by the local terrain shape, at least at low elevations, while higher above the turbine is more susceptible to discrepancies in the stability conditions between the LES and field data. Since the LES does not include buoyant forces, choosing a high altitude point would magnify this discrepancy. Furthermore, the choice of locations is limited in that it must lie within the Galion scanning geometry. The scan points furthest upstream of the turbine, shown in Figure 36, are least under the influence of the aforementioned effects, and are chosen to determine the reference velocity. This is achieved in the LES by sampling a four-hour averaged u_r field at these points, then spatially averaging the points to obtain the value given in Equation 6.2. Therefore the LES data fields and synthetic lidar measurements are normalized by reference velocity $u_{\infty,LES}$, given in Equation 6.3. Similarly with the Galion data, these points were spatially averaged to determine $u_{\infty,GAL}$, using the data for a single scan, which was all that was available. In Equation 6.3, the absolute value $|u_\infty|$ is used for normalization to preserve the sense of negative towards the lidar and positive away.

$$
\begin{aligned}
u_{\infty,LES} &= -4.10 \text{ m s}^{-1} \\
u_{\infty,GAL} &= -3.94 \text{ m s}^{-1}
\end{aligned}
\tag{6.2}
$$

$$
u_r^* = u_r/|u_\infty| \tag{6.3}
$$

6.6 Wake Center Detection

A simple method to define the wake center was implemented, which locates the point of maximum velocity deficit within the wake, at several downstream locations from the turbine. The location of this maximum velocity deficit (typically defined via the mean streamwise component) is assumed to coincide with the maximum u_r point, where the flow is moving toward the lidar (away from the turbine) most slowly. This assumption is considered fair since the mean flow direction is aligned with the turbine axis, and the lidar is situated nearly directly downstream of the turbine, so that maxima and minima in u_r should follow those in u.

6.6.1 Wake Search Region

As described in Section 6.4.1, yz-planes of data (LES,synthetic, and Galion data) have been interpolated onto to measure the wake (see Figure 29). Within each of these planes, a smaller subplane, or "search plane", (see Figure 37) is defined in which the wake center location will be "searched" for, meaning that of the points lying in this search plane, the point with maximum velocity $u_{r,Max}$ (biggest velocity deficit) is selected to be the wake center.

The size of this plane must be selected so as to enclose the wake at all times, yet small enough for reasonable computational times. Choosing the dimensions of this region therefore requires some inspection of the wake beforehand, by observing ensemble-averaged velocity and standard deviation LES fields, as well as the synthetic and Galion scan data. The dimensions were also chosen to avoid the terrain-generated turbulence, which typically occupies the bottom quarter of the interpolation plane. This was achieved by raising the bottom of the region above most of this terrain turbulence, as shown in Figure 38. As will be demonstrated, a major setback of this method is its inability to avoid locating $u_{r,Max}$ within this turbulence. As with the interpolation planes, the search plane yz dimensions were chosen to be constant with downstream distance for computational simplicity, even though the elevation drops drastically downstream of the turbine (which lies on top of the ridge), and the growth of the terrain's turbulent boundary causes it to extend further into the search region for the downstream planes.

Two methods were explored to track the location and value of $u_{r,Max}$. Method 1 uses a fixed search plane, shown in Figure 38, while Method 2 uses a smaller search area which moves based on the location of $u_{r,Max}$ in the nearest upstream plane, while still remaining within the larger, fixed search plane. The second method was implemented after observing that Method 1 was selecting locations for $u_{r,Max}$ which were clearly far away from the wake. The following steps outline these two approaches to locating the wake center in the LES, synthetic lidar, and lidar field (Galion) data:

Method 1: Fixed Search Region

1. For each downstream plane, the entire search plane is used to determine the location and value of $u_{r,Max}$

Method 2: Moving Search Region

1. For the plane closest to the turbine, all points with distance from the turbine axis less than a diameter ($\sqrt{y^2+z^2} \leq 2R$) are used to locate $u_{r,Max,1}$.
2. For the next plane downstream, all points with distance ($\sqrt{y^2+z^2} \leq 1.5R$) from the yz coordinates of $u_{r,Max,1}$ from the previous upstream plane are used to locate $u_{r,Max,2}$.
3. Similarly for the i^{th} downstream plane, the region near $u_{r,Max,i-1}$ is used to locate $u_{r,Max,i}$.

The distances of $2R$ and $1.5R$ in Step 1 and 2 were chosen after observing the results from both methods on an instantaneous and 1-cycle-averaged LES field, as well as single synthetic lidar and Galion scans, shown in Figures 38, 39,40, and 41, respectively.

The results of Figures 38, 39,40, and 41 show the wake center as identified by both methods, with a black "+" for Method 1 and a red "X" for Method 2. The data used are from the LES, synthetic

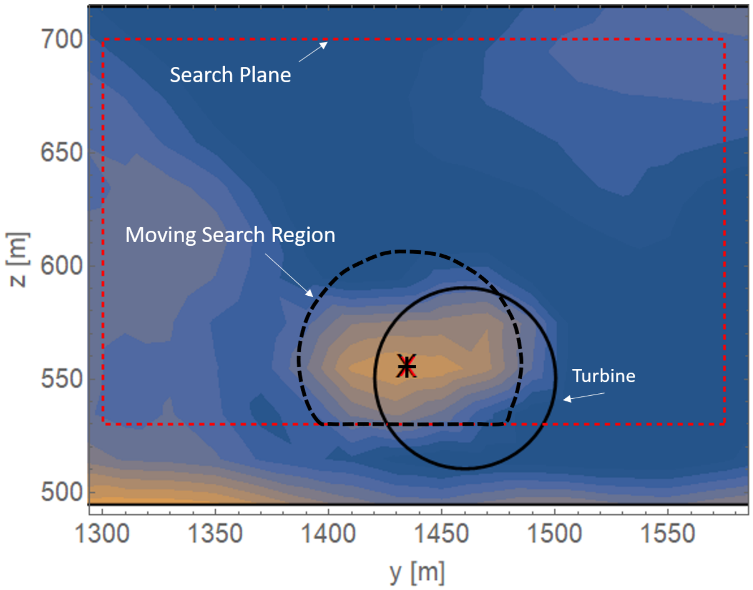

Figure 37: Search plane and moving search region for wake center identification.

lidar, and Galion data and for one geometry only, i.e. the scan geometry used in the Galion field measurements. Figures 38, 39 show the LES field, averaged over the duration of one scan cycle ($t_{cycle} = 9.8$ minutes), and an instantaneous field, taken at the beginning of the first cycle, i.e. at $t = 0$. For both fields, Methods 1 and 2 place the wake center at the same location, however, for the averaged field, the wake center is identified in the terrain turbulence instead of the wake. This occurs at planes of $x^+/D \geq 3$, where the terrain turbulence grows to extend to the bottom of the search plane, in close proximity to the actual wake, which is clearly visible. For the instantaneous field, the wake center is identified as lying within the wake for all planes, although it is clear from the wake's oblong shape that the actual wake center is located further in the $+y$ direction. Also evident is the merging of the wake with the terrain turbulence from approximately $x^+/D = 2$ to 3.

Both synthetic and Galion lidar interpolation planes show data cut-out from the top of the plane. This is because the planes further downstream start to extend outside of the cloud of lidar points, as seen previously in Figure 29, and so cannot be interpolated onto in that region. The single-scan synthetic lidar data of Figure 40 samples the same LES data as Figures 38 and 39. It is evident that the wake shape is distorted as compared to the LES, likely due to lower spatial resolution and most strongly by the temporally disjunct nature of the scan data. In this geometry, PPI (or stacked sector scans) is used, which scans from low ϕ to high, so that the bottom row of the plane is roughly 7-8 minutes older than the top. To illustrate the temporal variability of the wake shape and velocity over one cycle, instantaneous planes at $x^+/D = 0.5$ of the same LES data are shown in Figure 42, taken each minute of the cycle. A view of this variability at different downstream locations is given in Figures 39 and 43, taken at the first and last instantaneous LES fields of the scan cycle, respectively. Compared to the $t = 0$ field, the wake at $t = t_{cycle}$ is stretched vertically, displaced towards $-y$, and the surrounding velocity field is slower (less negative). These effects account for the vertical wake "deformation" and displacement in the $-y$ direction observed in the synthetic scan with respect to the $t = 0$ field, as well as the more positive flow field observed at the top of the plane, a region more representative of the end-of-cycle flow field. In addition to this distortion making wake center determination less accurate, Method 1 (fixed search area) identifies $u_{r,Max}$ in the terrain turbulence for $x^+/D \geq 3.25$ instead of the wake. Method 2 avoids this issue by restricting displacement of the wake center as it moves downstream, although for both cases the lack of data coverage in planes $x^+/D \geq 3$ disallows tracking the full wake.

The single-scan Galion data of Figure 41 retains some features of the LES and synthetic scan data, such as an identifiable wake and a growing boundary layer of terrain turbulence, while in general wind speeds are faster and the wake shape less elongated compared to the synthetic case. However, a matching of wake shape and speeds is not to be expected, as the Galion data was selected only on the basis of high wind speeds (for more neutral conditions) and wind direction. From $x^+/D = 0.5$ to 1, Method 1 identifies the wake center in some small regions of slow air, which are evidently not part of the wake, and from $x^+/D \geq 2$, both wake center detection methods locate $u_{r,Max}$ in the terrain turbulence.

Based on these observations, the moving search area method more consistently identifies the wake center and will be used for the remaining analysis in the study. The performance of the wake center detection algorithm in relation to assessing the synthetic scan accuracy will be addressed in Section 9.1.

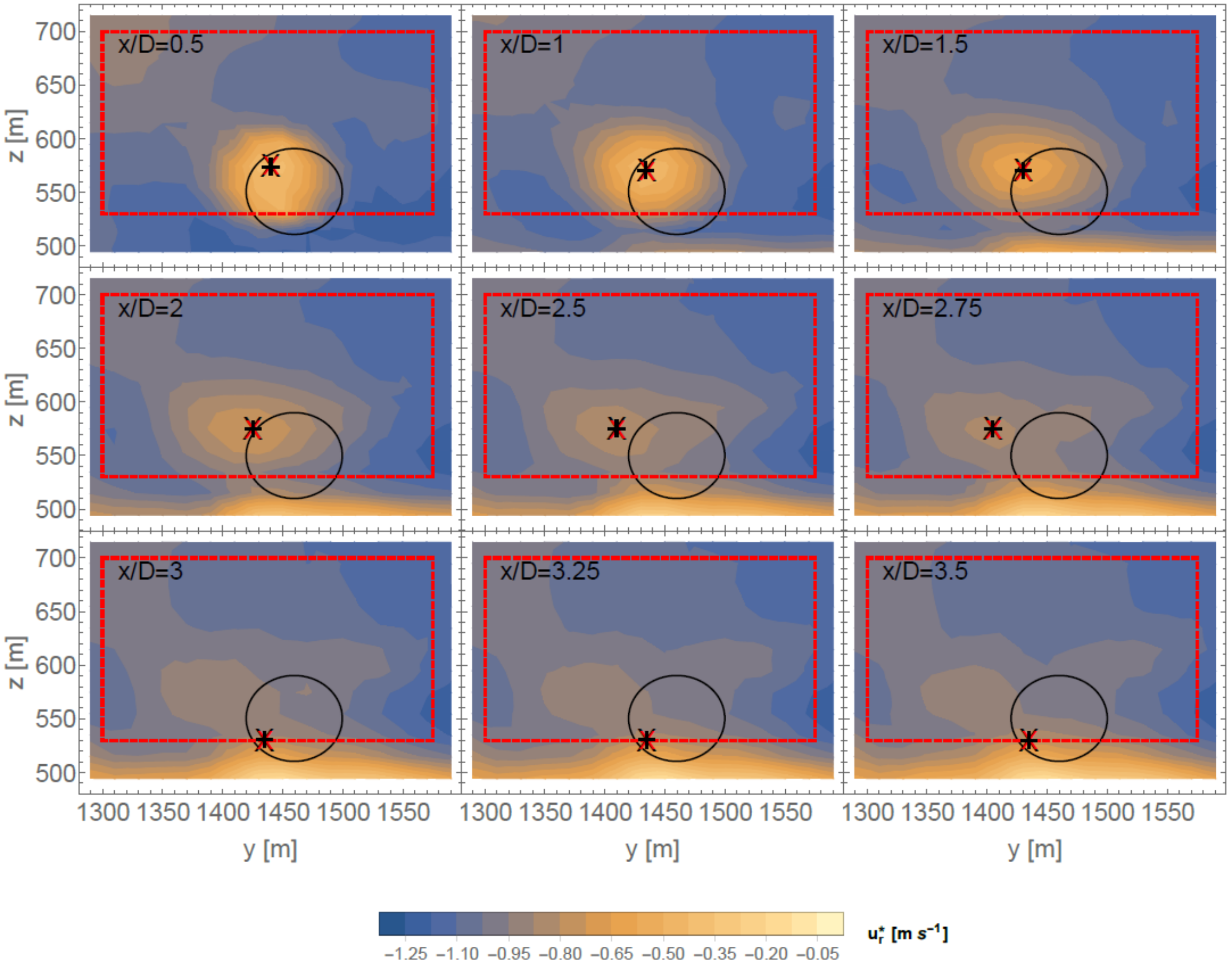

Figure 38: Planes of LES data downstream of the turbine, averaged over one scan cycle. Red box: wake search region; red "X": Maximum u_r location (moving search area); black "+": Maximum u_r location (fixed search area)

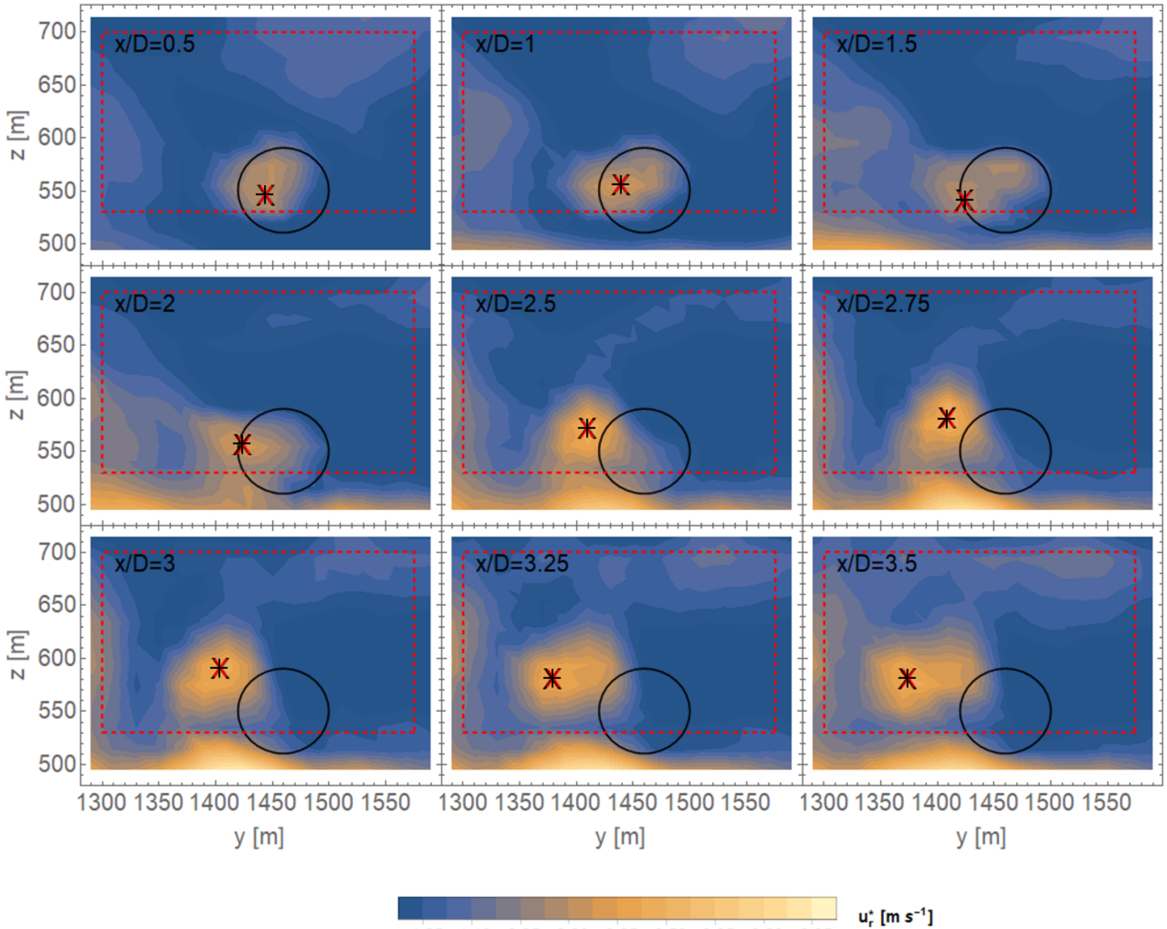

Figure 39: Planes of LES data downstream of the turbine, taken at $t = 0$. Red box: wake search region; red "X": Maximum u_r location (moving search area); black "+": Maximum u_r location (fixed search area)

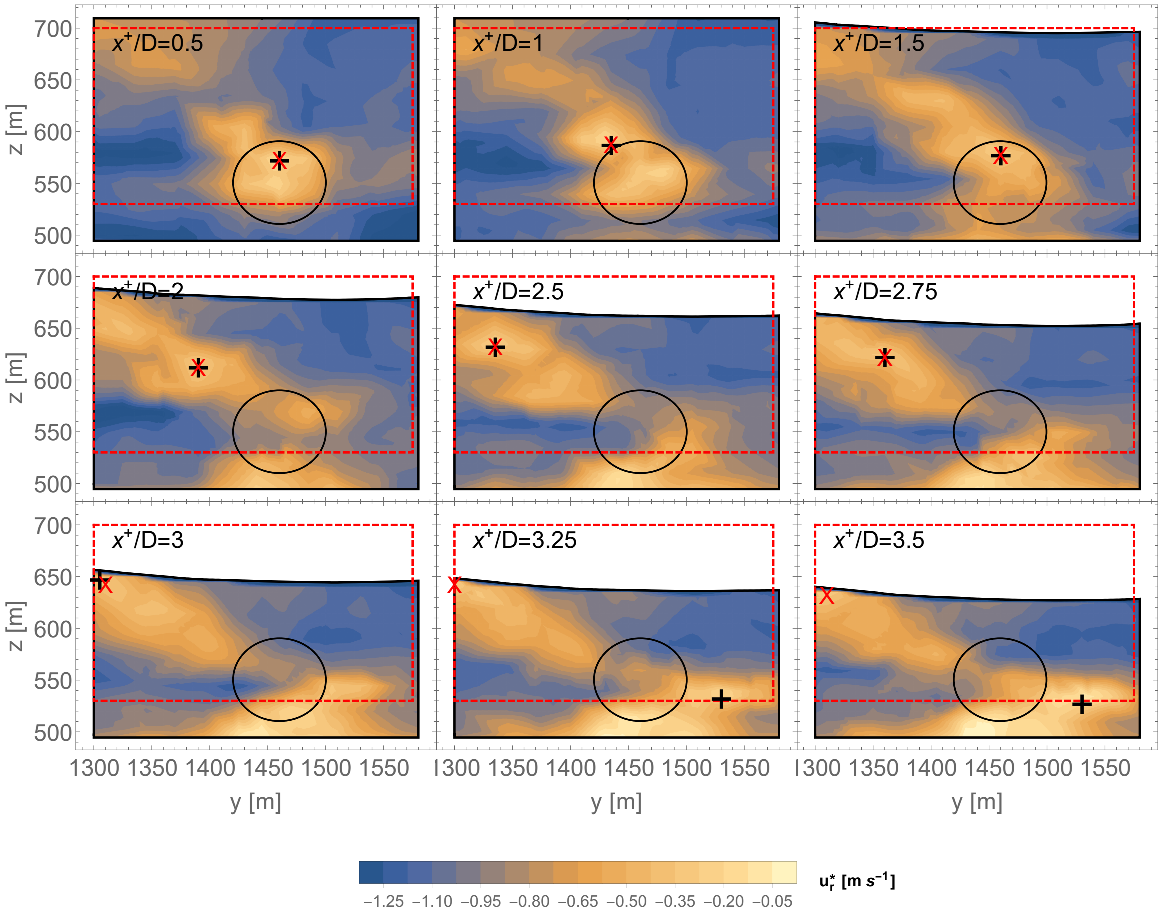

Figure 40: Planes of synthetic lidar data downstream of the turbine. Red box: wake search region; red "X": Maximum u_r location (moving search area); black "+": Maximum u_r location (fixed search area)

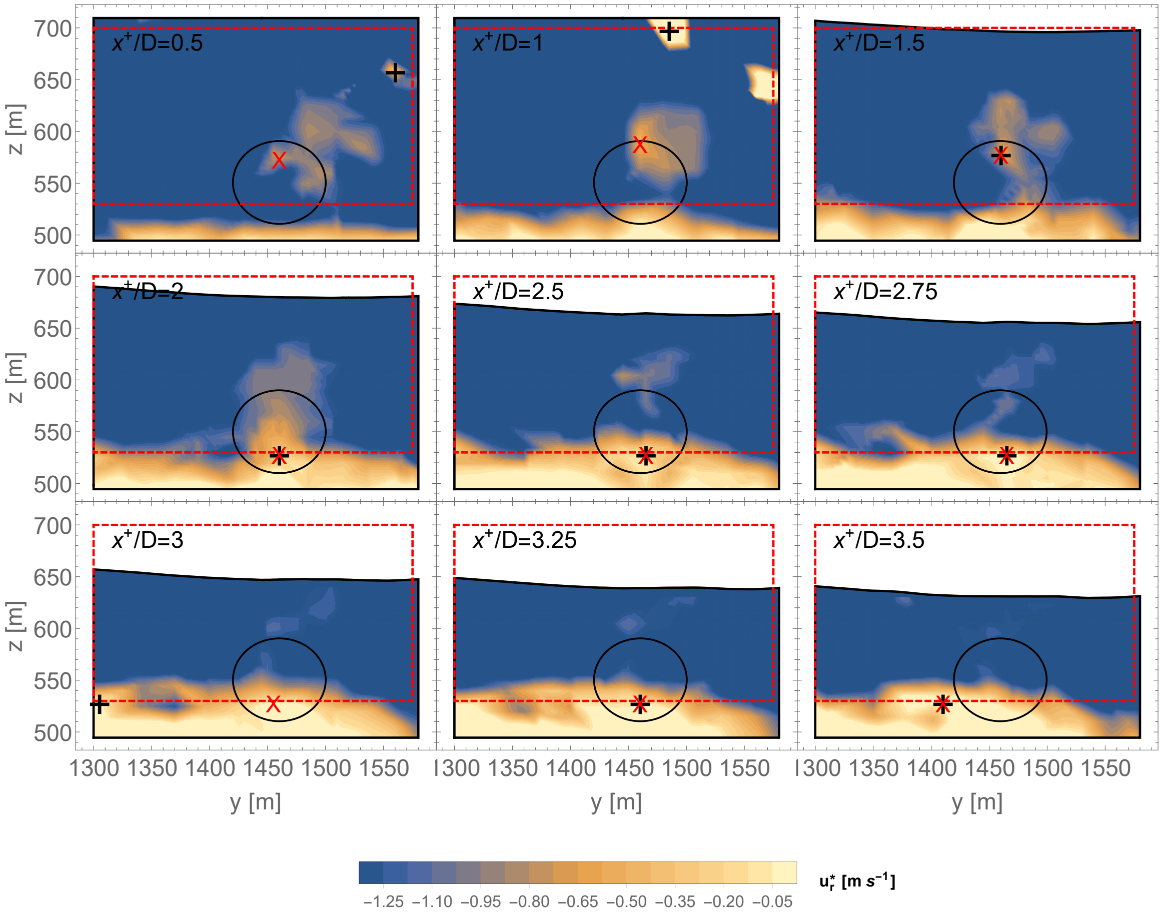

Figure 41: Planes of Galion data downstream of the turbine. Red box: wake search region; red "X": Maximum u_r location (moving search area); black "+": Maximum u_r location (fixed search area)

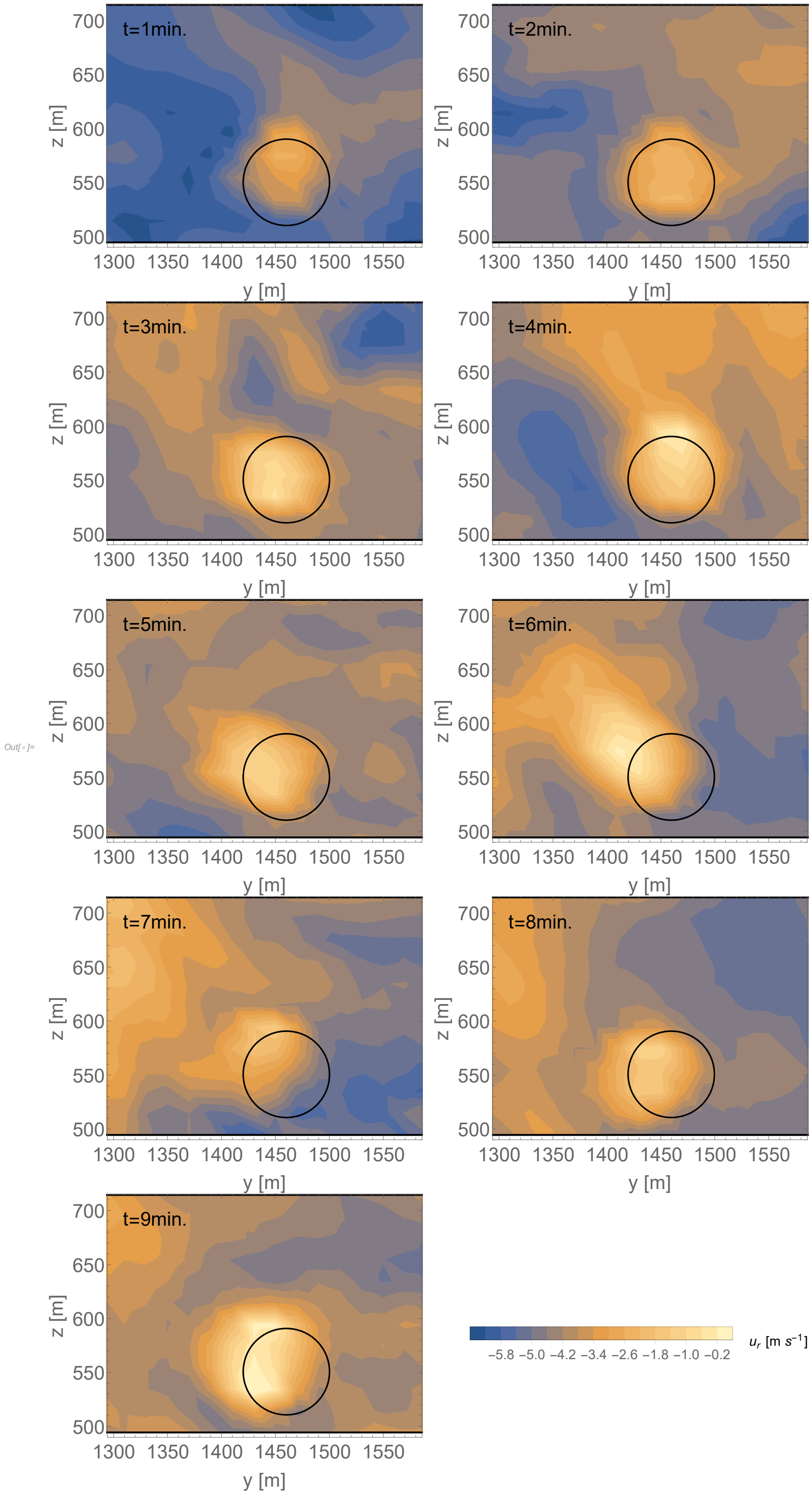

Figure 42: Instantaneous LES fields at $x^+/D = 0.5$, take each minute of a scan cycle

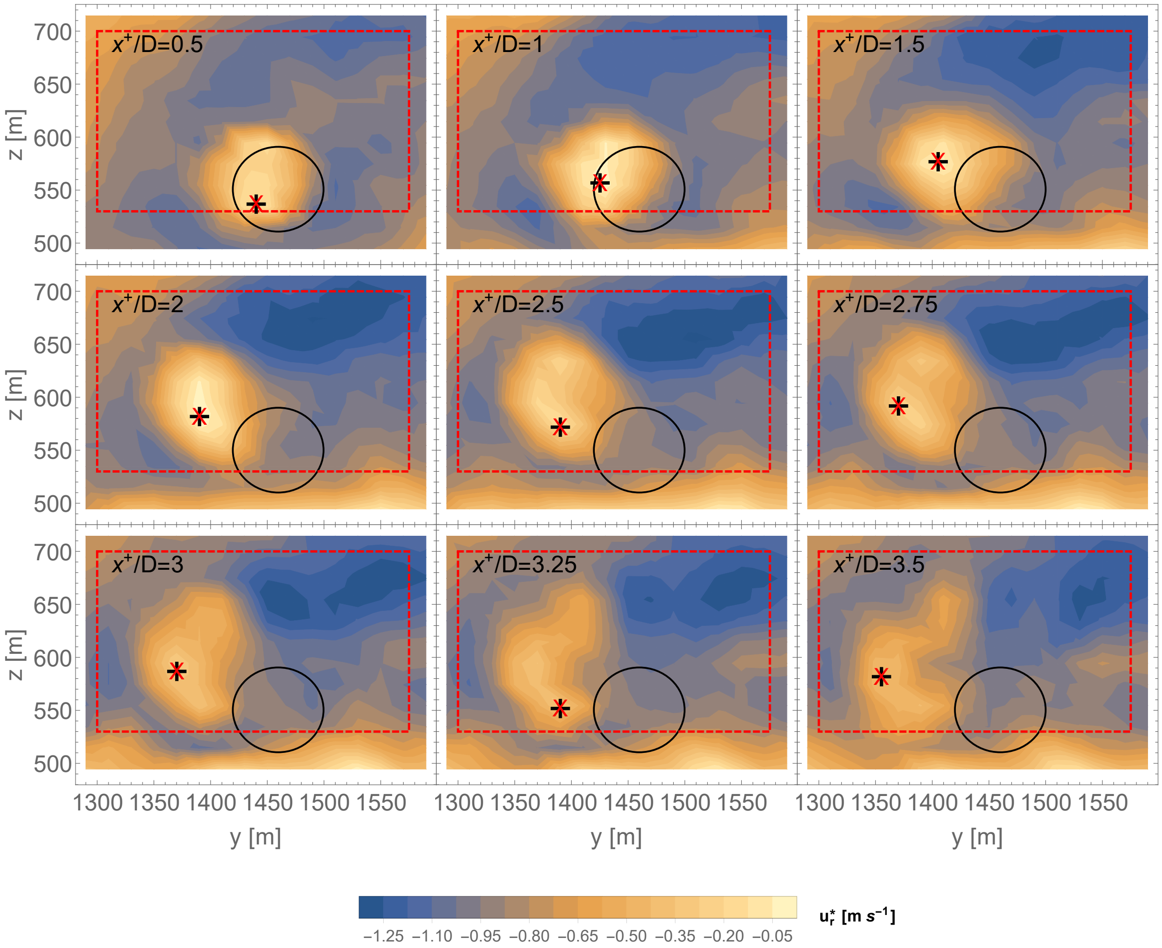

Figure 43: Planes of LES data downstream of the turbine, taken at $t = t_{cycle}$. Red box: wake search region; red "X": Maximum u_r location (moving search area); black "+": Maximum u_r location (fixed search area)

7 Geometries Tested

Now that an algorithm has been developed which extracts the wake center location and maximum deficit, the results of the algorithm can be compared using a set of different scanning geometries. In addition to the geometries created for this study, the geometry provided as part of the Galion data taken at Perdigão in 2017 will be tested.

Constructing a scan geometry consists of defining the range gate size (radial distance between two neighboring scan points on the same LOS), number of range gates along each beam N_{rg}, and a time sequence of azimuth-elevation angle pairs, defining the direction of each beam, and the time between successive beams Δt_s, which is effectively the sampling rate of the LES field.

The parameters which were kept constant in all geometries tested are given in Table 6, and where chosen to equal those from the Galion data. Also, the location of the lidar for any geometry was not changed from the Perdigão experiment. Although the Galion geometry (from here on called GAL), does not hold the angular separation between successive beams $\Delta\theta$ and $\Delta\phi$ constant, the time between each beam is still constant at $\Delta t_s = 1.95$ s. Presumably the scanner head speeds up accordingly to keep this constant, and so this interval was also kept for all geometries tested. The Galion also discards first two range gates, i.e. at 30m, and 60m, because of unacceptably high SNR and therefore were also discarded for all geometries created, so that all range gate locations are $r \in [90\text{ m}, 1260\text{ m}]$.

Parameters which were varied for the geometries include the spatial resolution (measurement point density), the scan path, and the scan area.

Table 6: Parameters common to all scan geometries

Range gate size	30 m
Number of range gates per beam	$N_{rg} = 40$
Time between beams	$\Delta t_s = 1.95$ s
Range gate locations	$r \in [90\text{ m}, 1260\text{ m}]$

7.1 Resolution

All wake characteristics in the current study are functions of space, and therefore characterization is sensitive to spatial resolution. The choice to vary the resolution of each geometry was motivated by the findings of Doubrawa *et al.* [13], which observed a dependence of the velocity deficit statistics on the density of measurement points in the planes used to characterize the wake. In the current setup, wake characteristics are determined at the interpolation planes of Section 6.4.1, the spatial resolution at these planes being a critical parameter. For the LES data, the resolution at these cross-planes is fixed by the model at $\Delta x = \Delta y = 20$ m (see Table 3), while Δz stretches from 5 m at the bottom of the planes to 11 m at the top. For synthetic lidar, the points are essentially scattered, with the density of points (and spatial resolution) increasing closer to the lidar. A *nominal* resolution of a scan geometry will be defined here by the distance between neighboring points on a vertical "slice" $r = 1020m$, which passes through the rotor plane (see Figure 44). Several resolutions were tested for the geometries, from 20 m on the high end, to match the LES

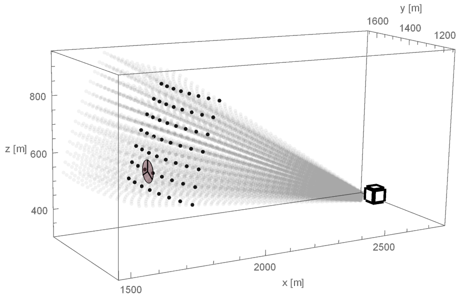

Figure 44: Points at $r = 1020m$ used to define nominal resolution of a scan geometry

resolution, to 70 m to show the results at an extremely low resolution. Resolutions lower than 80 m are larger than the rotor diameter, and so are not suitable for measuring wake length scales. A list of the nominal resolutions and their corresponding resolutions at the first and last wake detection planes (defined Section 6), is given in Table 9.

7.2 Scan Path

Two types of common scan patterns were tested, PPI and RHI, depicted previously in Figures 14 and 15, respectively. Typically RHI patterns are used to obtain vertical wind speed profiles and moment fluxes [27], therefore may be of interest to include in addition to a wake measurement campaign. PPI patterns have been used to measure large-scale horizontal flow structures in complex terrain [27], and could be used for example to characterize inflow conditions ins non-homogeneous in horizontal direction.

For PPI, the bottom and top edges of the planes are represent approximately the beginning and end of the scan cycle, respectively, while for RHI the same is true for the left and right edges. The temporal disjunction of the two scan patterns is visualized in Figure 45, which marks the time along the beam path and highlights the difference in this disjunction pattern between the two. One would expect that if there is an asymmetry in the horizontal and vertical wake dynamics, e.g. the spatial and time scales of horizontal and vertical meandering are different, that the type of scan pattern becomes more important in determining wake characteristics. These scales are can be dependent on the wind direction distribution, yaw misalignment, local terrain, etc.

7.3 Scan Area

The area covered by the scan points in the plane of interest has been shown to be important in characterizing the wake center [13]. Of course this coverage area is a function of distance from the lidar. Figures 46 and 47 show the change in coverage area in the vertical and horizontal directions, respectively, with distance from the lidar. In general there is a trade off between scan area and cycle time which needs to be considered and depends on the spatial and temporal variability of the wake.

7.4 Description of Geometries

The GAL geometry follows a PPI pattern, and has the characteristics given in Table 7. The PPI and RHI geometries created for this study (Table 8), have different resolutions, the values of which were chosen with using the GAL resolution as a starting point. Notice the decrease in cycle time

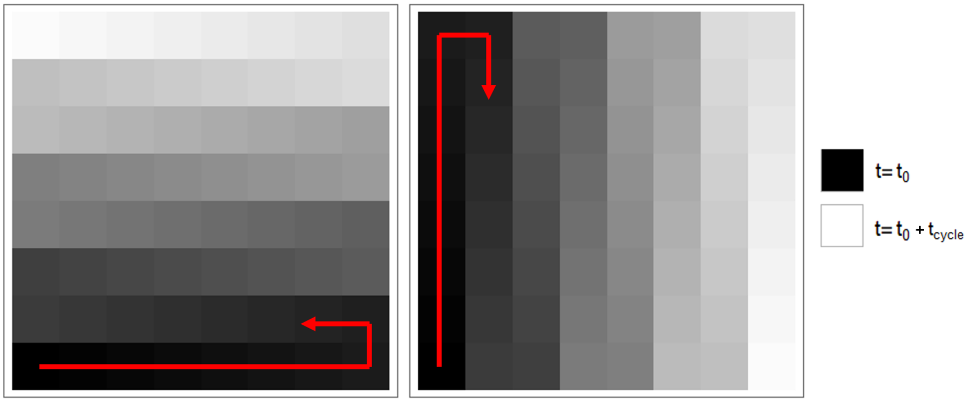

Figure 45: Temporal map for PPI (left) and RHI (right) scan paths over one cycle.

t_{cycle} with decreasing resolution. As mentioned in the previous section, the separation $\Delta\theta$ and $\Delta\phi$ between beams varies for the GAL geometry, however it is kept constant for the others, and chosen to achieve the desired resolution.

As seen in Figure 46, the GAL geometry does not completely cover all the planes of interest in the vertical direction, starting from $x^+/D = 1.5$ (5th plane downstream), while the coverage extends horizontally far beyond the planes, shown in Figure 47. All of the geometries created for this study (see table 8) were chosen to achieve complete coverage in all downstream planes while minimizing the coverage outside of these planes, where the wake rarely extends. Minimizing unnecessary scan coverage reduces the scan cycle time, so that a single scan more closely represents an instantaneous field, and allows more scans cycles to be completed (and averaged) over the course of the available simulation time T_{LES}. Of course, narrowing the scan range required prior knowledge of the location of the wake, from the averaged fields of Section 6. In a study where less is known about the wake location, it is not possible to narrow this range as much. The choice to do so in this study was based on completing more scan cycles, of which the individual wake estimates could be averaged over and therefore produce a more reliable gauge of a geometry's performance compared to the others.

Both geometries have their azimuthal range approximately centered on the turbine, while the elevation range was shifted upward for those geometries created for the study (given in Table 8) relative to the GAL geometry, as shown in Figure 46. This shift was made because the GAL geometry intersects the ground near the turbine, leading to useless data points, and does not extend high enough for coverage in the furthest downstream planes.

Geometry	**Res.**	**Az. Range**	**El. Range**	t_{cycle}	**# cycles in** T_{LES}
GAL	26.7 m	$\theta \in \{199.5^o, 253.5^o\}$	$\phi \in \{7.0^o, 23.0^o\}$	9.8 min.	$N_c = 10$

Table 7: Galion geometry

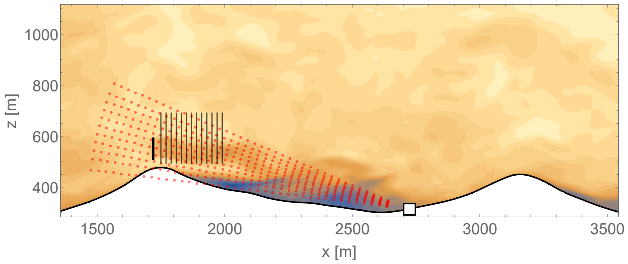

(a) GAL geometry

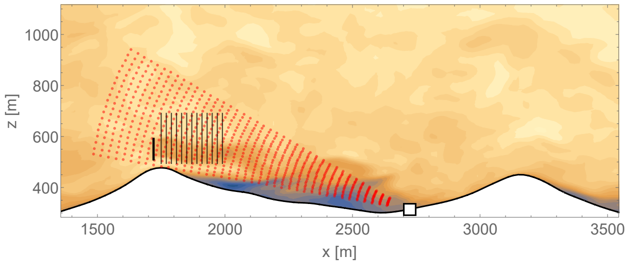

(b) PPI, resolution = 20 m

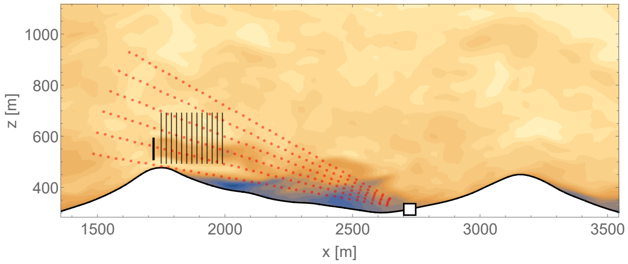

(c) PPI, resolution = 70 m

Figure 46: Streamwise transect of GAL, PPI20 and PPI70 geometries, including wake detection planes.

Geometry	**Res.**	**Az. Range**	**El. Range**	t_{cycle}	**# cycles in** T_{LES}
PPI20 & RHI20	20 m	$\theta \in \{212.6^o, 237.3^o\}$	$\phi \in \{9.9^o, 29.9^o\}$	14.2 min.	$N_c = 7$
PPI30 & RHI30	30 m	$\theta \in \{212.6^o, 237.3^o\}$	$\phi \in \{9.9^o, 29.9^o\}$	6.3 min.	$N_c = 16$
PPI40 & RHI40	40 m	$\theta \in \{212.6^o, 237.3^o\}$	$\phi \in \{9.9^o, 29.9^o\}$	3.9 min.	$N_c = 27$
PPI60 & RHI60	60 m	$\theta \in \{212.6^o, 237.3^o\}$	$\phi \in \{9.9^o, 29.9^o\}$	1.8 min.	$N_c = 57$
PPI70 & RHI70	70 m	$\theta \in \{212.6^o, 237.3^o\}$	$\phi \in \{9.9^o, 29.9^o\}$	1.3 min.	$N_c = 78$

Table 8: PPI and RHI geometries

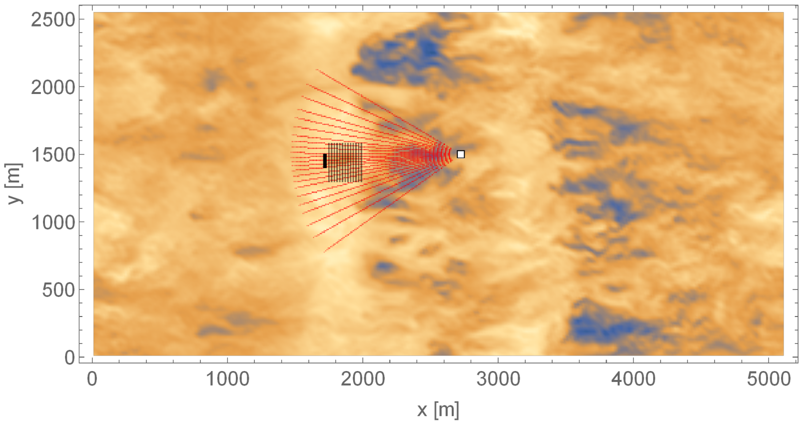

(a) GAL geomtery

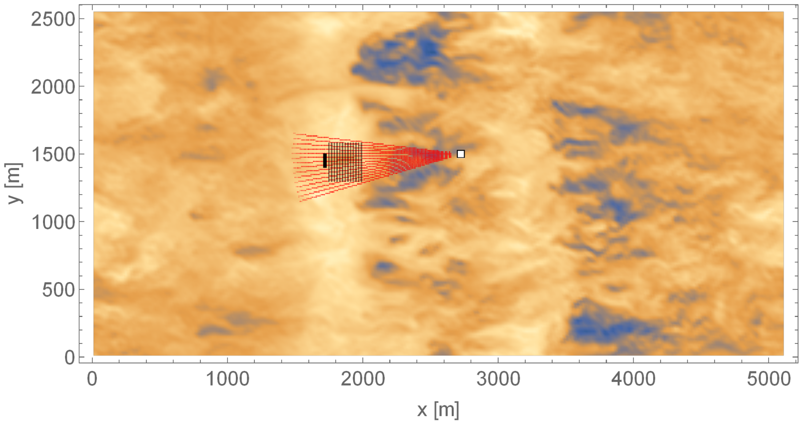

(b) PPI, resolution = 30 m

Figure 47: Plan view of wake detection planes and a) GAL geometry and b) PPI30 geometry.

Nominal Res. [m]	**Res. at $x^+/D = 0.5$ [m]**	**Res. at $x^+/D = 3.5$ [m]**
20	19.7	15.3
26.7	26.1	20.3
30	29.5	22.9
40	39.4	30.6
60	59.0	45.9
70	68.9	53.5

Table 9: Nominal resolutions and corresponding resolutions on wake detection planes.

8 Results

This section will present the results of the characterization of two wake metrics (as defined in Section 6), the wake center location, and the velocity at the wake center location, by the synthetic lidar scans. This is performed for all geometries listed in the previous section. The values of these metrics are then compared against those determined from the LES data. For all cases, the metrics will be determined using data interpolated onto the $y - z$ cross planes defined in Section 6. The current section will detail how the LES data is processed in order to make meaningful comparisons to the synthetic lidar scans, then will show the variability of these metrics for each scan geometry, and finally assess their accuracy using the LES characteristics as the ground truth. The goal is to show how certain geometry parameters affect the accuracy and precision of these two wake metrics.

8.1 Data Averaging & Notation

Since the LES data is regarded as true, it is important that the wake characteristics are determined by the LES data in a way that they can be meaningfully compared to the synthetic wake characteristics. The synthetic lidar data does not give the properties of wake at a particular instant, nor over an averaging time, so when comparing it to the LES fields it is not expected to match the instantaneous field or an averaged field. Therefore it must be considered how this LES data should be processed in terms of ensemble and time averaging.

In addition, comparing a single scan gives wake characteristics associated with the scan period only, and the error of that scan only. For this reason, scans for each geometry are completed as many times as possible within the simulation time T_{LES}, so that average values of the wake position and maximum deficit can be computed (and compared to LES-derived metrics), as well as an average of the errors of each individual synthetic scan. Averaging errors over multiple scans gives a better estimate of how accurate a scan geometry really is. The following will give an overview of the notation for the synthetic scan data as well as the LES fields they will be evaluated against, and the three different ways the LES data is processed.

8.1.1 Synthetic Scans

The velocity field for a single scan cycle (10th cycle out of 16) is shown in Figure 48, while the field for the ensemble average of all N_c cycles for the same geometry is shown in Figure 49. The notation

$$u_r^*(\boldsymbol{x}, t)$$

has been used to denote the synthetic lidar velocity field of a single scan and

$$\langle u_r^*(\boldsymbol{x}, t) \rangle$$

the ensemble average of that field over all scans, where t spans the duration of the scan, i.e. $t_o \leq t \leq t_o + t_{cycle}$, and t_o is the first instant of the cycle. The location of the maximum velocity deficit $\text{Max}[u_r^*(\boldsymbol{x}, t)]$ for a synthetic scan will be denoted $\boldsymbol{X}_s$. Note that for the ensemble-averaged field of Figure 49, the location of the maximum velocity deficit on the plot is the ensemble-averaged location of this point over the individual scans, that is $\langle \boldsymbol{X}_s \rangle = \langle \text{Max}[u_r^*(\boldsymbol{x}, t)] \rangle$. The velocity at the wake center $\boldsymbol{X}_s$ for a single synthetic scan is then denoted by shorthand $u_s = \text{Max}[u_r^*(x, t)]$, and its ensemble-averaged value $\langle u_s \rangle$. The reason that the maximum is taken of each individual scan

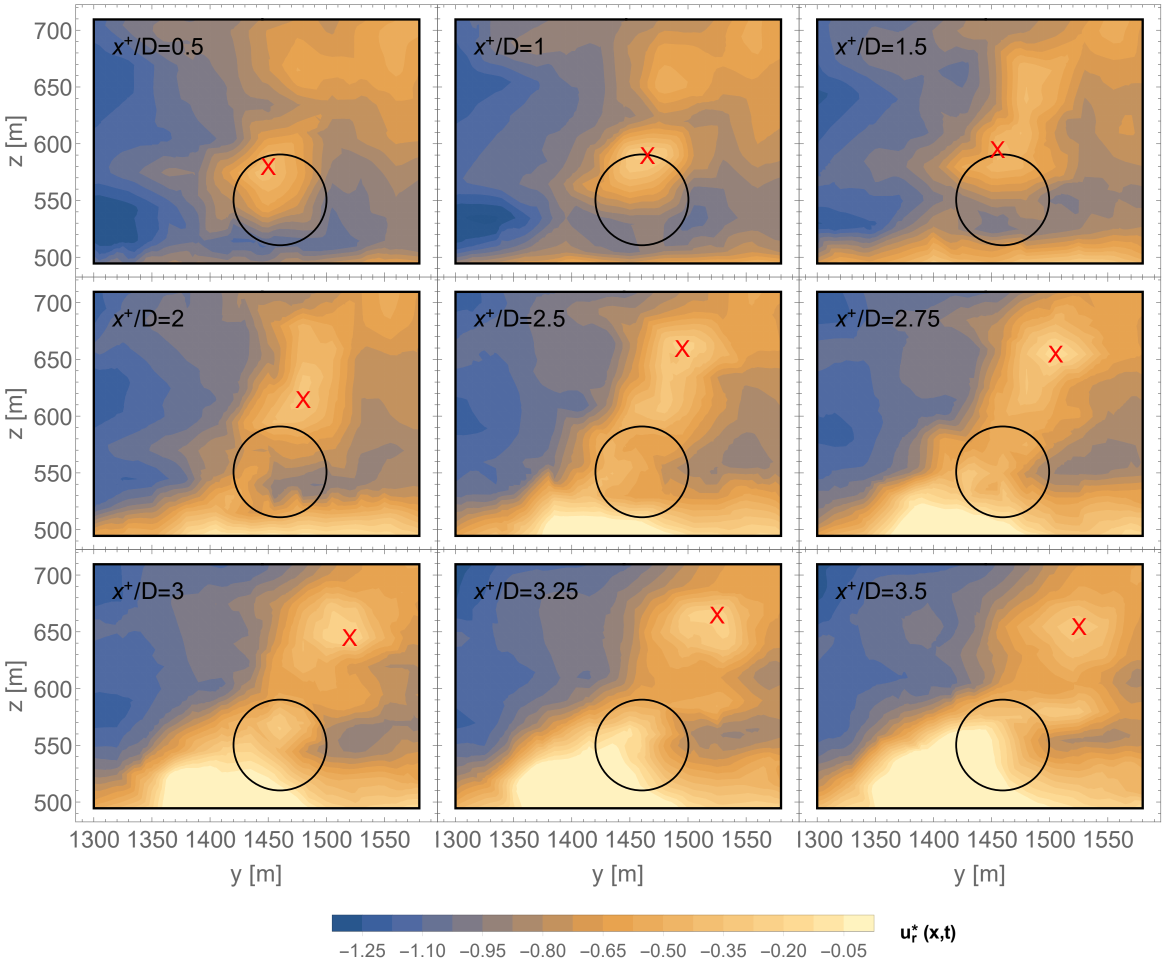

Figure 48: Synthetic lidar velocity field for the 10th scan, with geometry PPI30. Black circle: turbine rotor $y - z$ position. Red 'X': location of maximum velocity deficit.

instead of the ensemble-average, Max$[\langle u_r^*(\boldsymbol{x}, t)\rangle]$, is that if the error is a random error, given sufficiently large number of samples the ensemble-averaged synthetic and LES fields should converge, producing zero error and a meaningful error should not be dependent on sample size. The effect of using long-term averages as an indicator of error is discussed in Section 9.3.2.

8.1.2 LES 1st instantaneous fields

Each synthetic scan is compared to the first instantaneous LES field of each scan cycle, denoted

$$u_r^*(\boldsymbol{x}, t_o).$$

The ensemble average of all N_c 1st fields is denoted

$$\langle u_r^*(\boldsymbol{x}, t_o)\rangle.$$

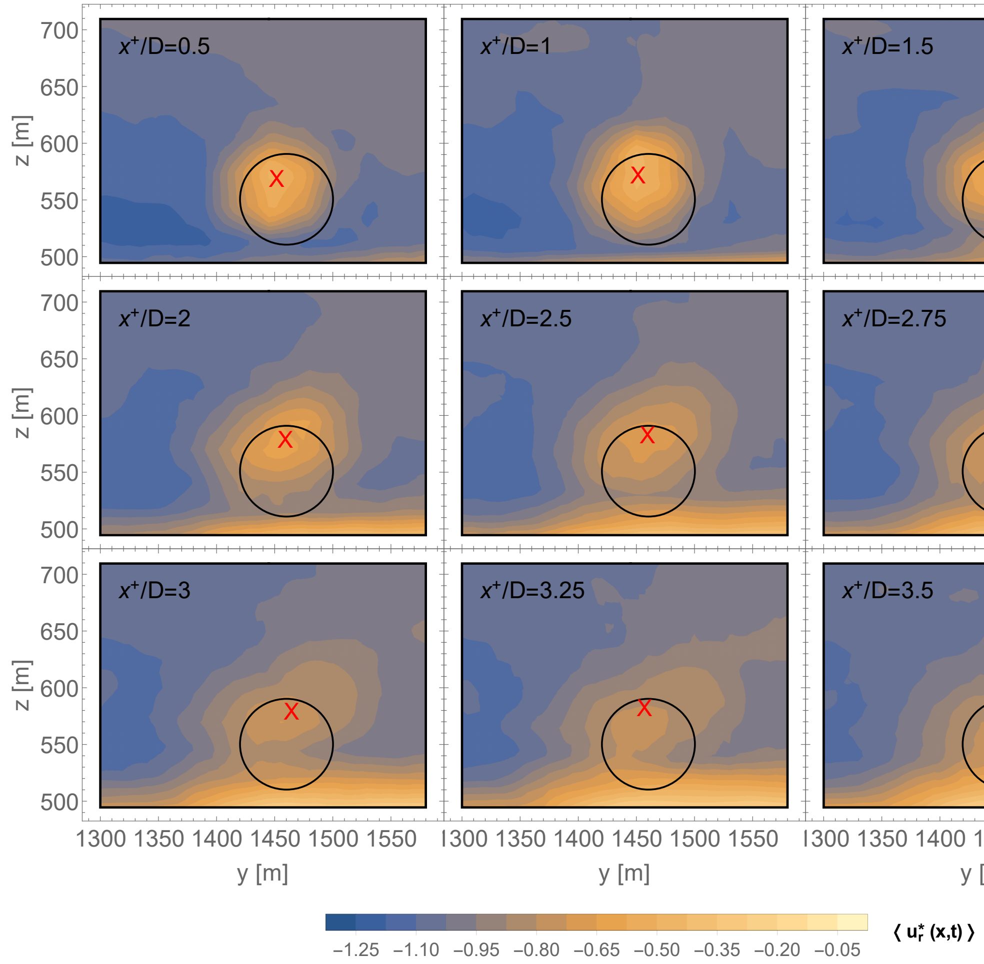

Figure 49: Synthetic lidar velocity field, ensemble-averaged over all cycles, with geometry PPI30. Black circle: turbine rotor $y - z$ position. Red ‘X’: location of maximum velocity deficit.

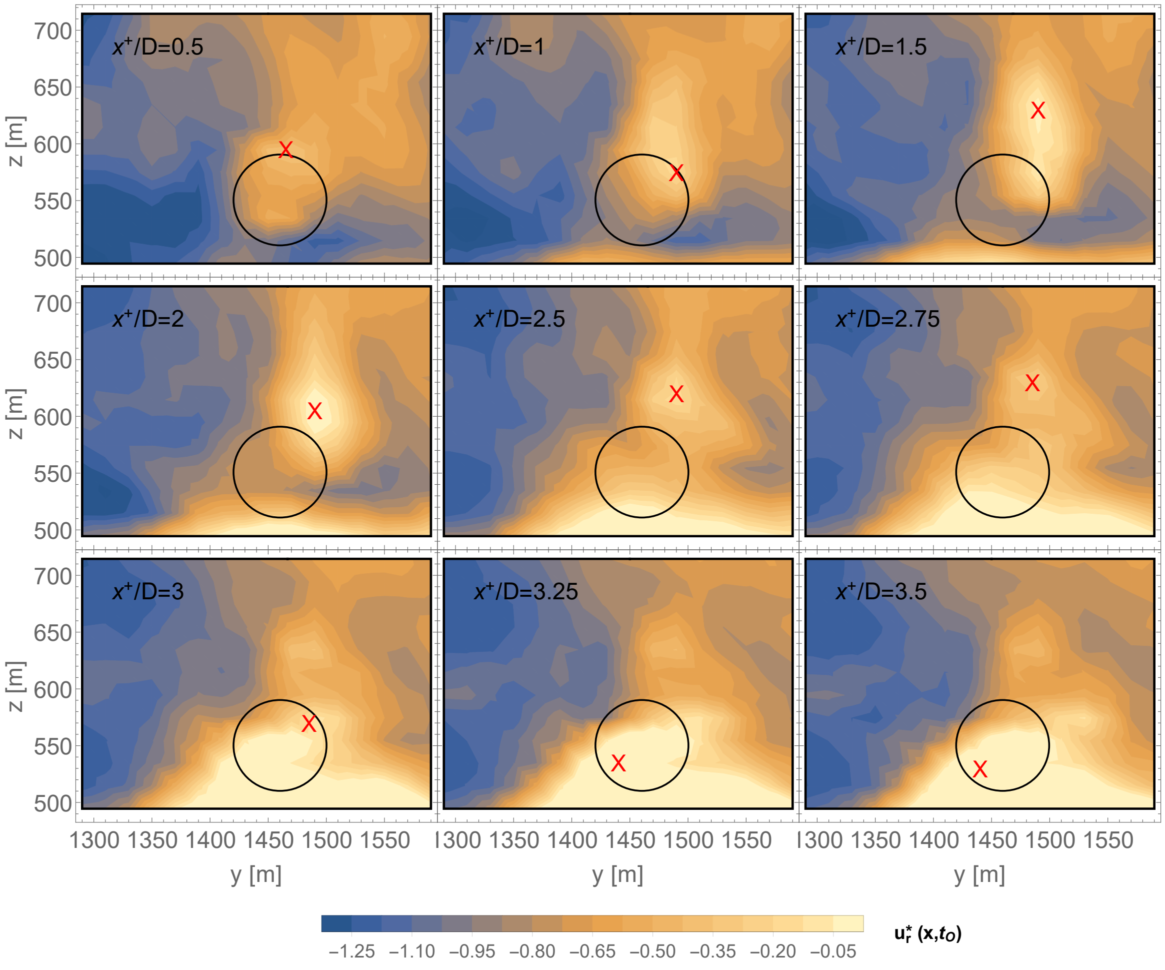

Figure 50: First instantaneous LES velocity field of the 10th cycle for geometry PPI30. Black circle: turbine rotor $y-z$ position. Red 'X': location of maximum velocity deficit.

As with the synthetic scans, the location of the maximum velocity deficit $\text{Max}[u_r^*(\boldsymbol{x}, t_o)]$ for each field will be denoted $\boldsymbol{X}_{LES,1^{st}}$ and the ensemble-averaged location $\langle \boldsymbol{X}_{LES,1^{st}} \rangle$. Similar to the above definition, the velocity at the wake center for each field is denoted $u_{LES,1^{st}} = \text{Max}[u_r^*(x, t_o)]$, and its ensemble-averaged value $\langle u_{LES,1^{st}} \rangle$. The corresponding first field of the synthetic scan shown in Figure 48 is shown in Figure 50. Notice that unlike the corresponding synthetic field, the search algorithm locates the wake center within the terrain-generated turbulence instead of the wake, which is undesirable.

8.1.3 LES Cycle-averaged fields

Each synthetic scan will be compared to an LES field which has been averaged over the corresponding scan period. This cycle-averaged LES field will be denoted

$$\widetilde{u_r^*}(\boldsymbol{x}),$$

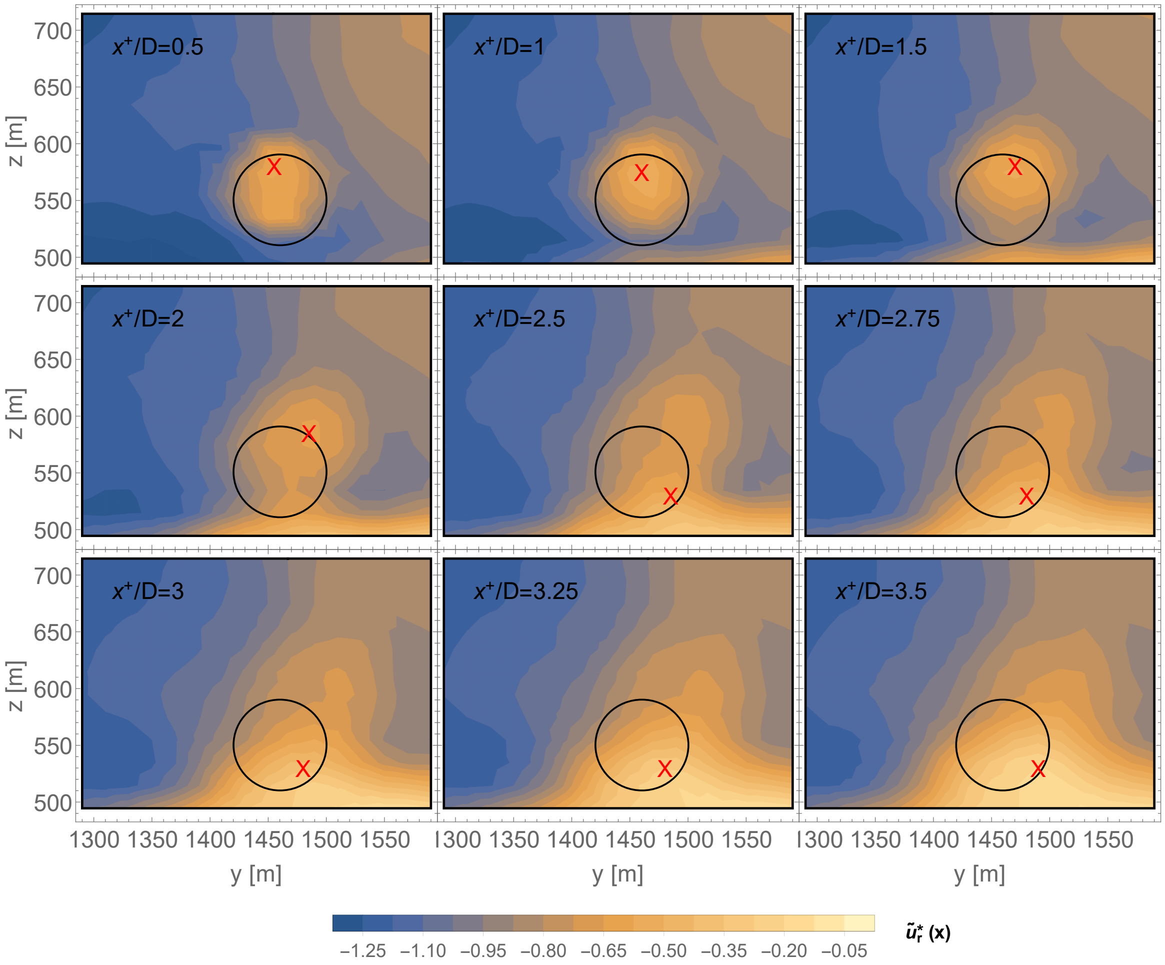

Figure 51: LES velocity field, averaged over the 10th cycle using geometry PPI30. Black circle: turbine rotor $y - z$ position. Red ‘X’: location of maximum velocity deficit.

and its ensemble-averaged field by

$$\langle \widetilde{u_r^*}(\boldsymbol{x}) \rangle,$$

while $\boldsymbol{X}_{LES,c}$ and $\langle \boldsymbol{X}_{LES,c} \rangle$ denote the location of the maximum velocity deficit and its ensemble average, defined similarly to the LES 1st instantaneous fields. Also similarly, the wake center velocity for each cycle-averaged field is denoted $u_{LES,c} = \mathrm{Max}[\widetilde{u_r^*}(x)]$, and its ensemble-averaged value $\langle u_{LES,c} \rangle$. The cycle-averaged field, again corresponding to the cycle of Figure 48, is shown in Figure 51.

8.1.4 LES time-averaged fields

Finally, each synthetic scan will be compared to a time-averaged LES field, in which each instantaneous field of the LES is averaged over the total simulation time. This field is denoted

$$\overline{u_r^*}(\boldsymbol{x}) \equiv \overline{u_r^*(\boldsymbol{x}, t)} \text{ where } t = 0 \leq t \leq T_{LES},$$

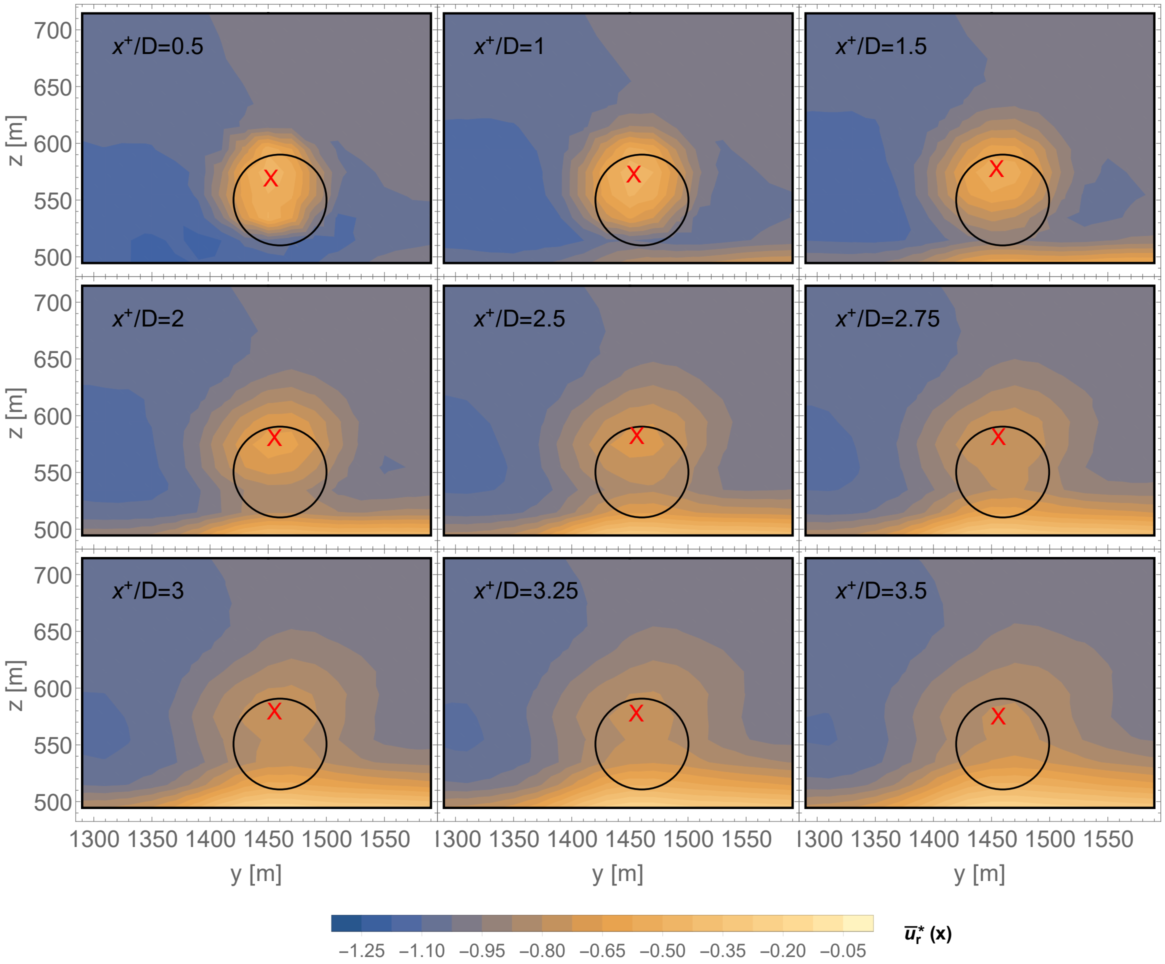

Figure 52: LES velocity field time-averaged over T_{LES}. Black circle: turbine rotor $y-z$ position. Red 'X': location of maximum velocity deficit.

and is shown in Figure 52. The location of the maximum deficit for a single instantaneous LES field is denoted $\boldsymbol{X}_{LES,t}$, and the time average of these locations $\overline{\boldsymbol{X}_{LES,t}}$, while the wake center velocity for each instantaneous field is denoted $u_{LES,t} = \mathrm{Max}[u_r^*(\boldsymbol{x},t)]$, and its time-averaged value $\overline{u_{LES,t}}$.

The procedure for averaging and detecting the wake in each field is depicted in Figure 53. This shows the fields which are inputs to the wake detection algorithm, the output of the algorithm, and subsequent averaging of the two wake metrics. It is important to note the order in which these operations are performed, as it differs according to the LES field type used. In particular, for the cycle-averaged fields, the wake detection algorithm is applied to a mean field, while in the other two types the fields, instantaneous fields are inputs to the algorithm. This has significant implications in the differences in wake metric values observed in the following section.

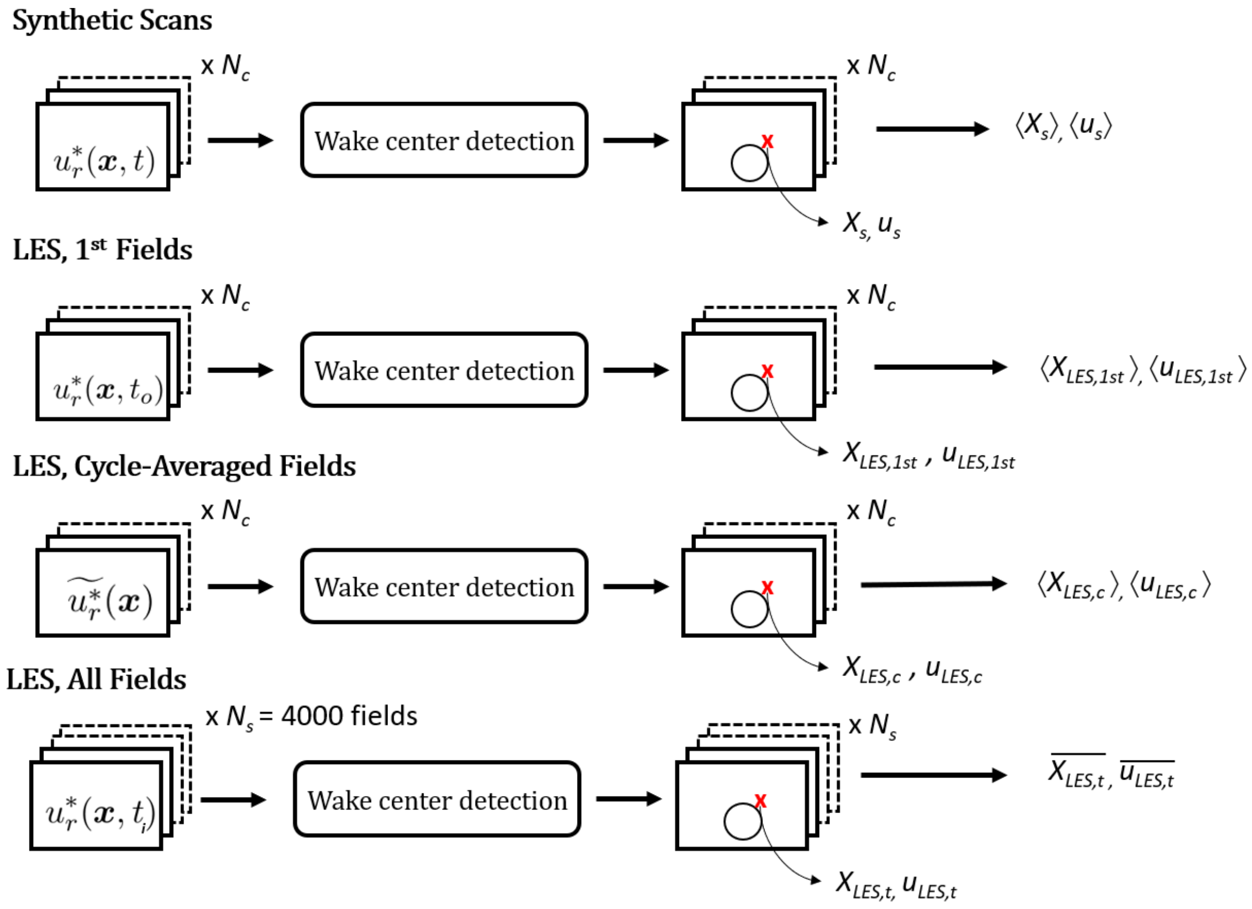

Figure 53: Procedure for field averaging, wake detection, and wake metric calculation

To better visualize the number of scan cycles for different geometries, Figure 54 shows timelines of the scan cycles over the simulation time T_{LES} for two geometries, PPI20 and PPI30. Note that t_0 marks the beginning of each scan cycle, so that for each geometry there are N_c instances of t_0.

In the following section, synthetic wake metrics will be compared to those determined from the three types of LES fields. When interpreting these results, it is important to consider what a time-averaged and ensemble-averaged wake represent in reality, and how averaging changes the values of these wake metrics. When fields are ensemble-averaged or time-averaged, the resulting field does resolve the fast turbulent fluctuations in and outside the wake, i.e. they are smoothed out. This directly impacts the wake center detection algorithm of Section 6, which searches for local maxima and so is sensitive to these velocity fluctuations. Also, averaging the fields is expected to make the wake area larger but reduce the velocity deficit, showing a temporal dependency of the wake metrics. Following the presentation of results, these questions will be addressed as well as their relationship to the potential goals of wake characterization.

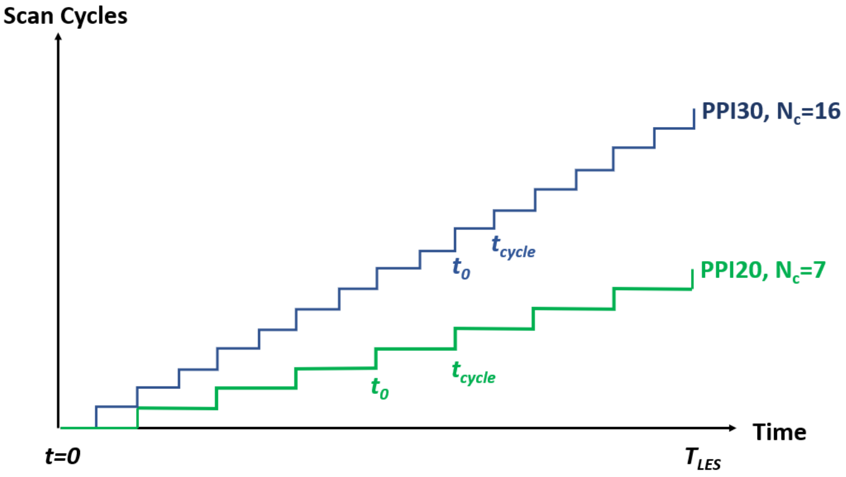

Figure 54: Number of scan cycles over the simulation time T_{LES} for geometries PPI20 and PPI30

8.2 Comparison of synthetic and LES wake metrics

This section will first compare the wake metrics of synthetic scans to the LES fields as processed by three different methods, followed by a discussion of the appropriateness of using each method for wake prediction/characterization. The single-scan Galion field data is also briefly presented. Again, all analysis is performed within the near-wake planes defined in Section 6.4.1, ranging from 0.5 to 3.5D downstream of the turbine. Comparison of the metrics will make use of the notation defined in Section 8.1.

8.2.1 Wake center location

The location of the wake center for different synthetic scans resolutions (defined in Section 7.1) and their variability is compared in Figure 55, shown for PPI scan geometries. Generally, the spread of $\langle X_s \rangle$ between the different geometries increases moving downstream, as does the variability in $\langle X_s \rangle$ for each geometry, indicated by its standard deviation in cross-stream and vertical direction. Wake center locations for the extreme high and low resolutions diverge from the others, and increasingly so further downstream. However, apart from the extreme resolutions, the estimated wake center location for each resolution lies within a standard deviation in both the cross-stream and vertical directions.

As a comparision to the PPI scans, Figure 56 shows variability in wake center location for the RHI geometries. Similar wake locations and diverging behavior is observed, however there is increased spread in the lateral position of $\langle X_s \rangle$ between the different resolutions. Interestingly, at the furthest downstream planes, the resolutions with highest standard deviations differ between PPI and RHI scans, which are 20 m and 30 m, respectively.

The ensemble-averaged wake center locations for the synthetic scan and three LES fields are shown in Figure 57 for a single resolution. Average awake center locations $\langle X_s \rangle$ show close agreement with $\langle X_{LES,1^{st}} \rangle$ and $\overline{X_{LES,t}}$ fields, which are both ensemble-averages of instantaneous fields , while cycle-averaged fields $\langle X_{LES,c} \rangle$ depart, placing the wake center slightly lower. Looking at the results for other resolutions in Figures 66 through 69 in the appendix, the higher resolutions place $\langle X_{LES,c} \rangle$

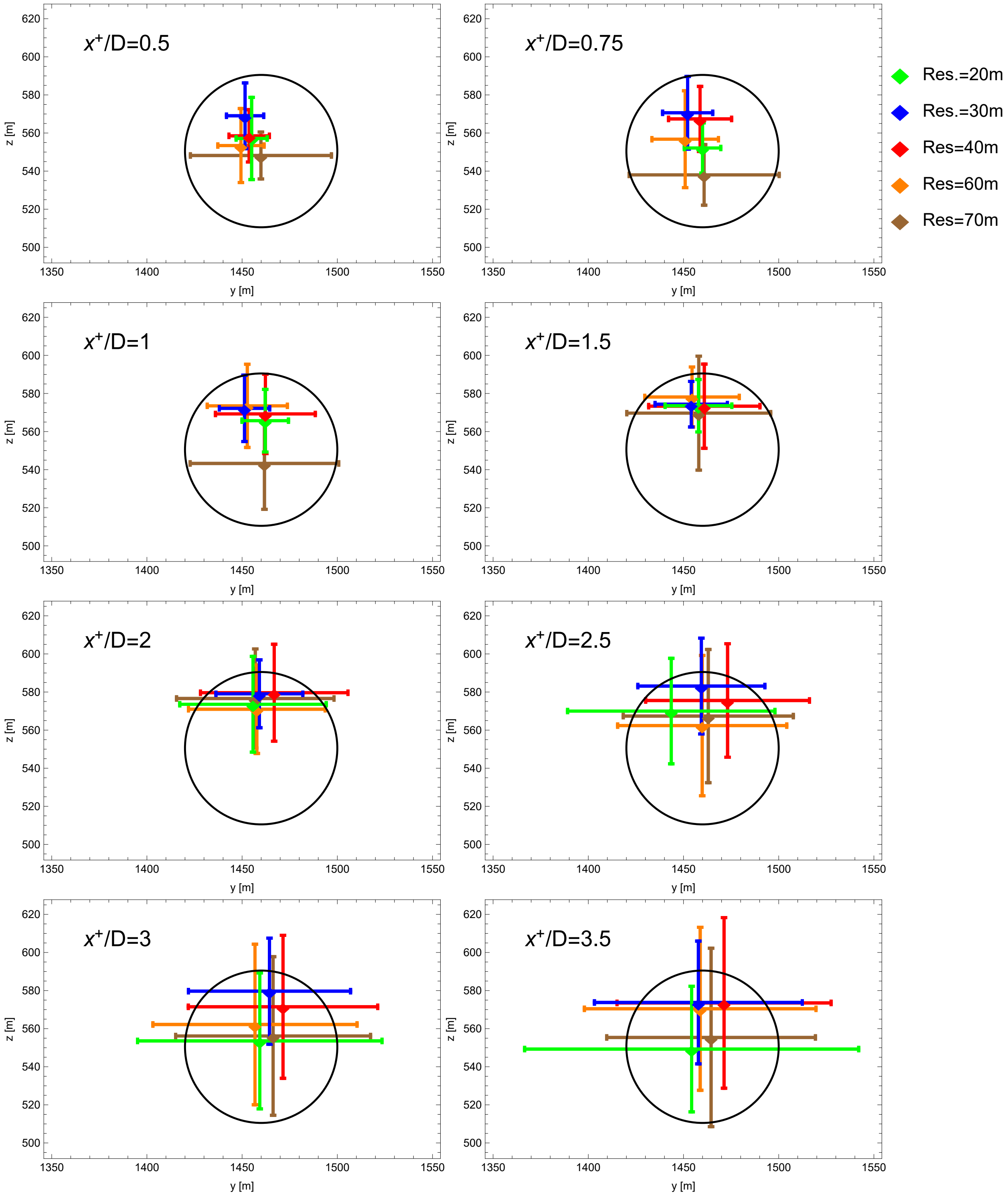

Figure 55: Ensemble-averaged wake center location $\langle X_s \rangle$ for PPI scan geometries. Error bars indicate a single standard deviation.

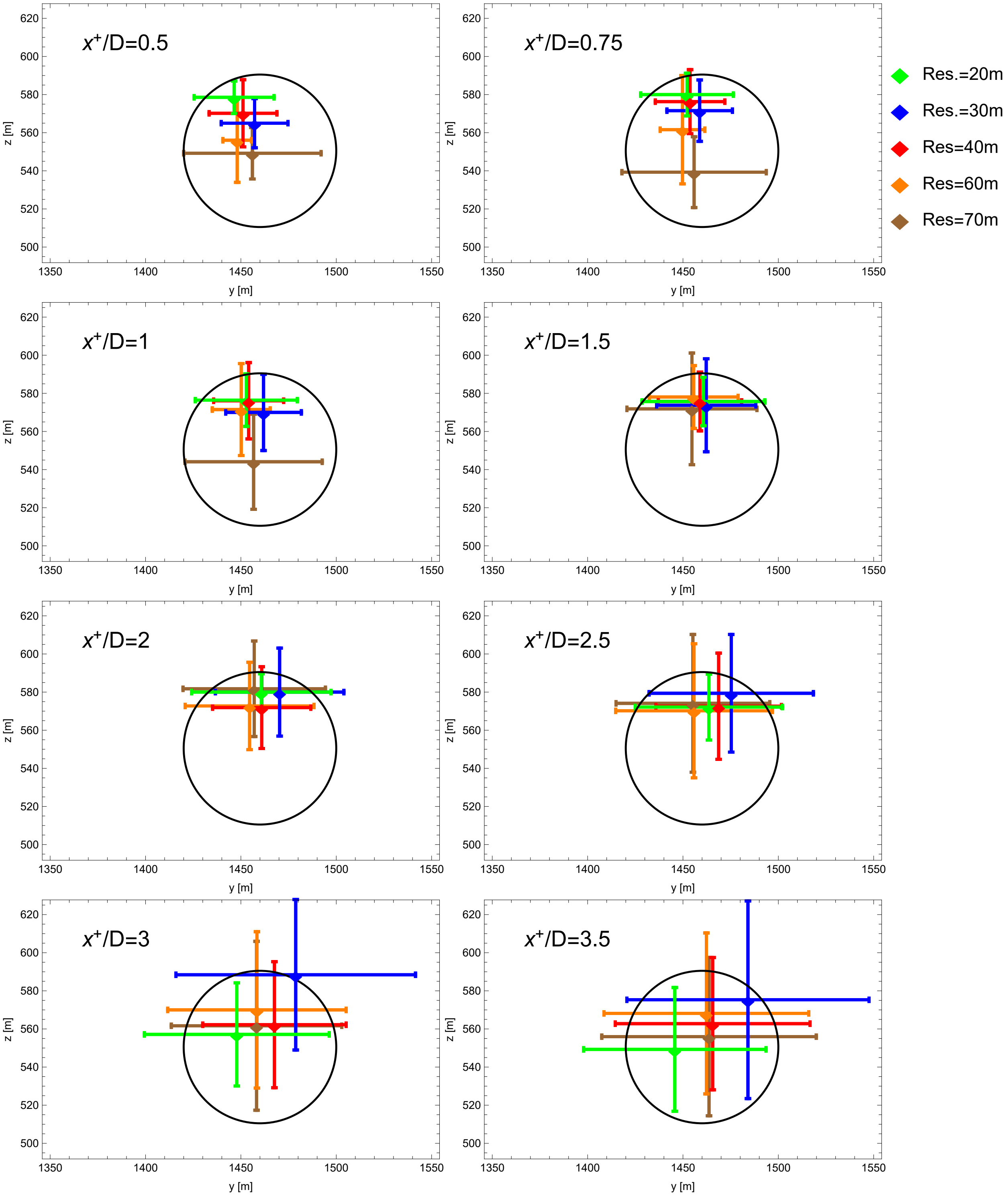

Figure 56: Ensemble-averaged wake center location $\langle X_s \rangle$ for RHI scan geometries. Error bars indicate a single standard deviation.

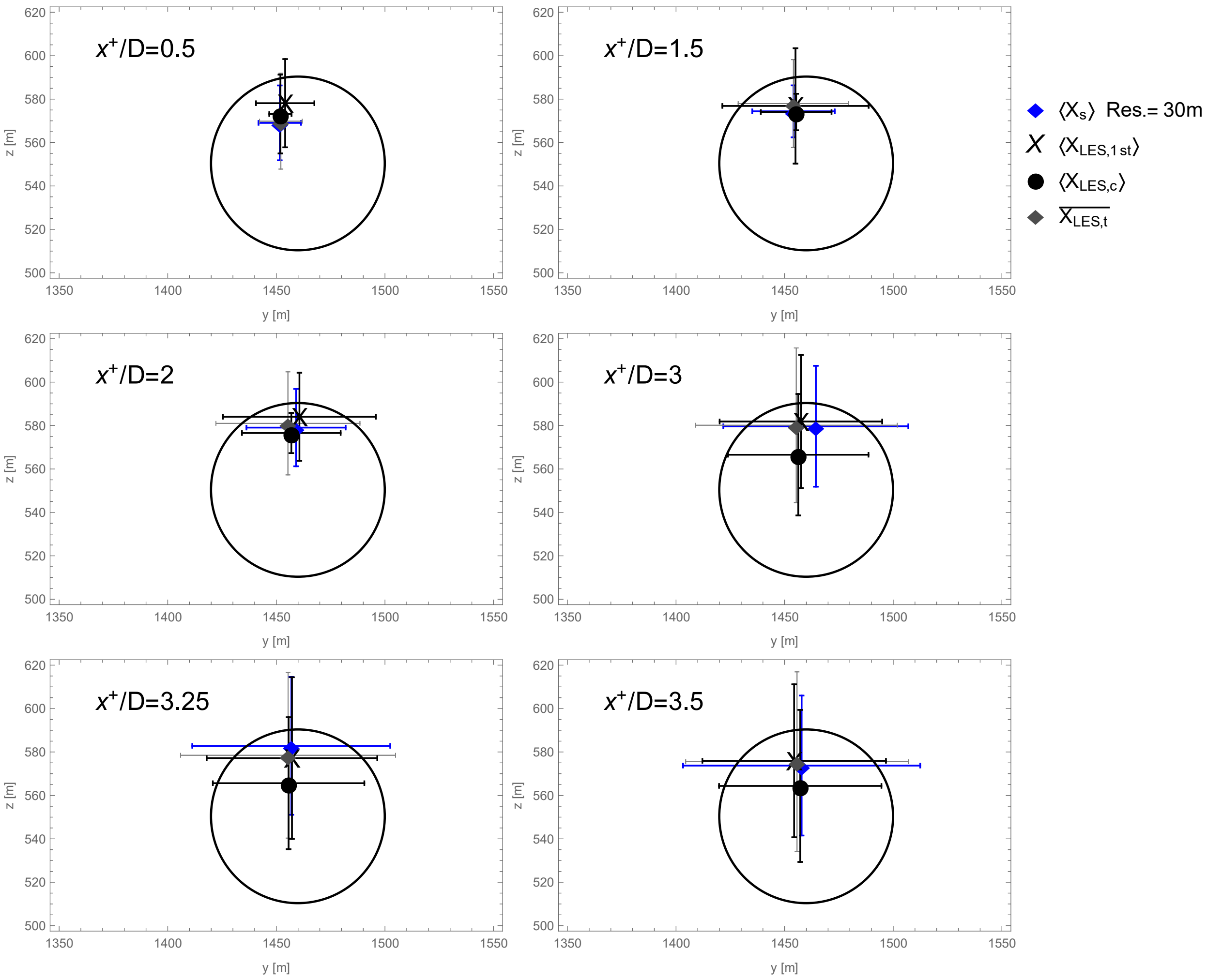

Figure 57: Average wake center location and standard deviation for PPI30 geometry, determined from synthetic and LES fields.

further from the other two LES field estimates, while at low resolutions, the scan time t_{cycle} is small enough to make the synthetic field closer to an instantaneous field, and so $\langle X_{LES,c} \rangle$ converges with the ensemble-averaged instantaneous metrics $\langle X_{LES,1^{st}} \rangle$ and $\overline{X_{LES,t}}$. The same figures indicate that the accuracy of $\langle X_s \rangle$ (with respect to the LES) is not strictly correlated with resolution, suggesting a trade-off in wake metric accuracy between scan time and resolution, in other words spatial and temporal resolution. However, it must be kept in mind that the number of samples N_c by which the metrics are averaged over is smaller for 20 m compared to 70 m by an order of magnitude, enlarging the uncertainty, comparatively. The reduced sample size increases the standard error $\frac{\sigma}{\sqrt{N_c}}$ by a factor of roughly 2 to 5 times in the vertical and horizontal directions, respectively, at the furthest downstream planes.

Figures 58 and 59 investigate the difference in wake center estimates between the synthetic scans and LES fields for each resolution of the PPI scan geometries. The difference is defined as euclidean

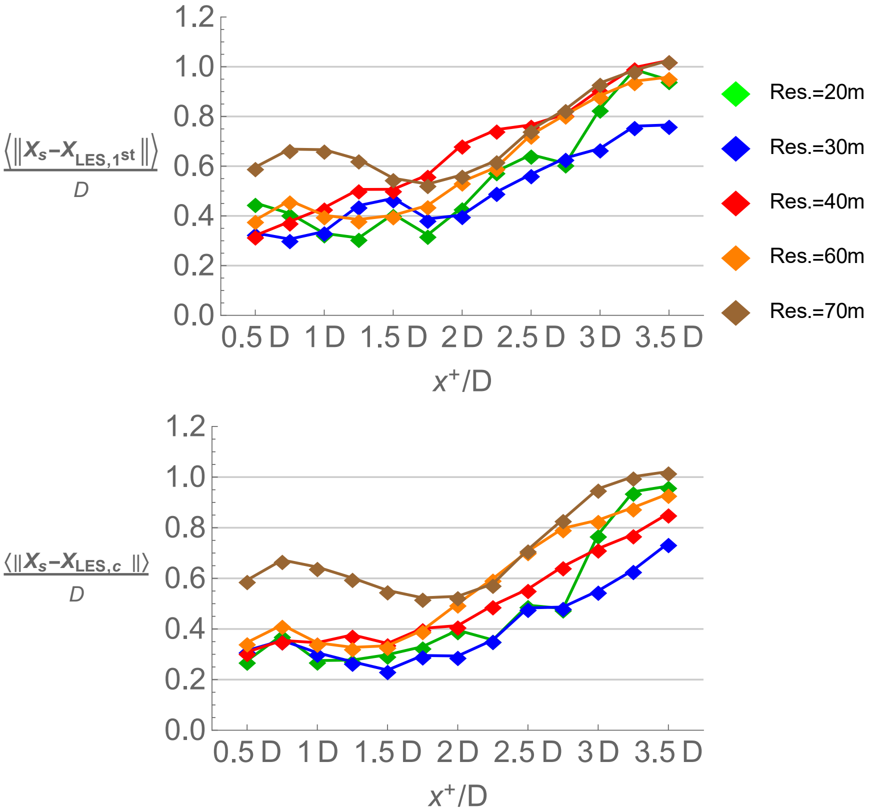

Figure 58: Error of synthetic wake center location with respect to two different LES fields, ensemble-averaged over N_c cycles.

distance between wake center estimates. Again, this difference is interpreted as an *error* of the synthetic metric with respect to the "real" flow field, the LES. This error is computed in two different ways. For Figure 58, first the distance between wake centers is calculated for each cycle, and afterwards ensemble-averaged to get an average of the errors. Normalized with rotor diameter this becomes $\frac{\langle \| X_s - X_{LES,c} \| \rangle}{D}$, for example, where $\| \bullet \|$ is the vector norm. For Figure 59 , first the ensemble-averaged wake centers are computed and then the distance between the two are taken (error of the averages). Likewise this becomes $\frac{\| \langle X_s \rangle - \langle X_{LES,c} \rangle \|}{D}$. The first method shows how accurate a single scan is on average, while the second method shows how close the ensemble-averaged metric is to the ensemble-averaged value in reality. Both methods can be useful, depending on the particular goal, i.e. wanting to know how the metric behaves on shorter versus longer time scales. This point will be discussed further in Section 9.

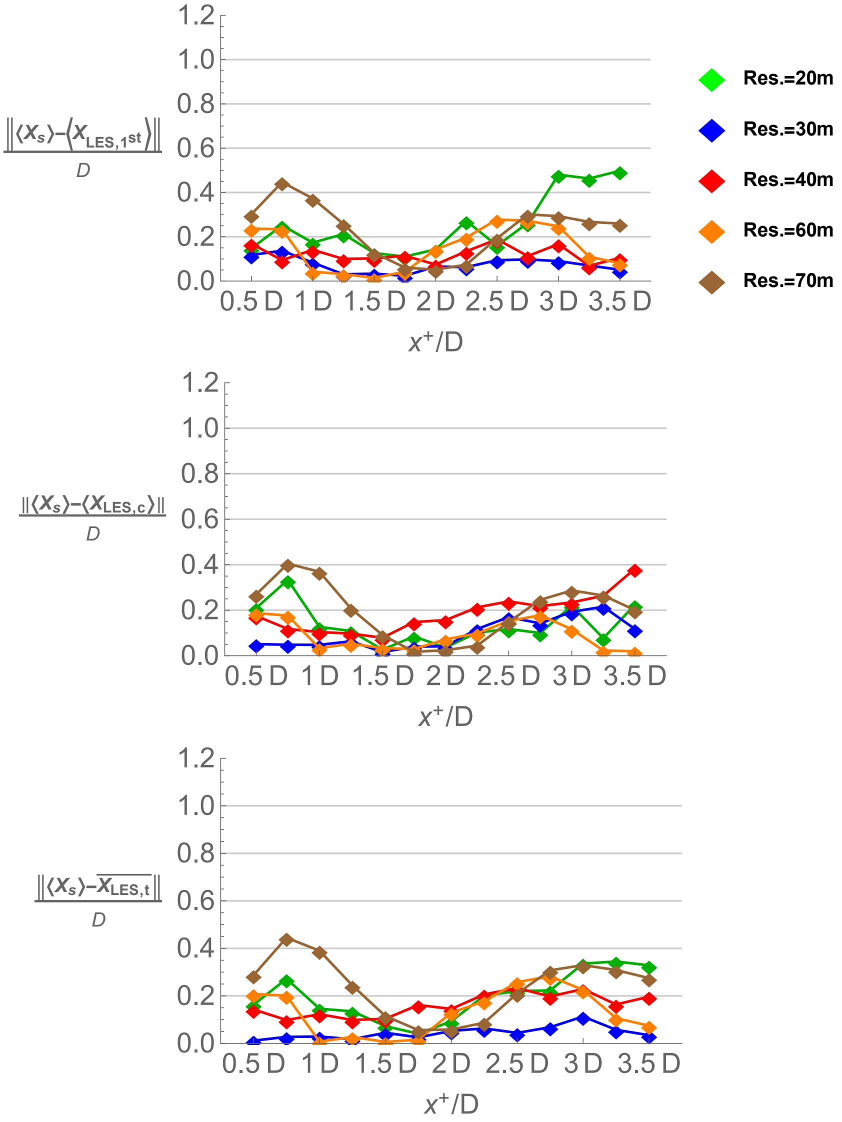

Figure 59: Error of ensemble-averaged synthetic wake center location with respect to three different LES fields

8.2.2 Wake center velocity

To give a sense of the agreement between wake center velocity estimates, Figure 60 shows $\langle u_s \rangle$ and its variability compared to that of the LES fields for a single geometry. The synthetic estimate $\langle u_s \rangle$ is within or nearly within a single standard deviation σ_{u_s} of each LES field. Likewise each $\langle u_{LES} \rangle$ is within $\pm\sigma_{u_{LES}}$ of $\langle u_s \rangle$.

Figure 61 extends the preceding comparison to each resolution of the PPI geometries. Observed in general is the wake center velocity slowdown as it moves downstream until approximately 1.25D, where it begins to recover momentum. However this recovery does not continue at the furthest downstream locations, likely due to mixing with the low-momentum wake of the ridge and subsequent identification of the wake center within this low-momentum region by the wake detection algorithm. Highlighted is the especially strong dependency of u_s and $u_{LES,c}$ on resolution. The expected reduction in velocity deficit due to averaging the wake, mentioned in Section 8.1, is evidenced by$u_{LES,c}$ and u_s having a relatively faster (more negative) wake center velocity, and the instantaneous fields of $u_{LES,1^{st}}$ and $u_{LES,t}$ having relatively slower wakes. In fact, comparing the cycle-averaged $u_{LES,c}$ at high resolution (longer scan times, t_{cycle}) to the low resolution (shorter scan times) shows that, as t_{cycle} gets shorter, $u_{LES,c}$ approaches the instantaneous metrics $u_{LES,1^{st}}$ and $u_{LES,t}$. Curiously, the opposite relationship holds for the synthetic data, i.e. as scan time gets shorter, u_s decreases, moving further from the instantaneous values. The averaged instantaneous fields $u_{LES,1^{st}}$ and $u_{LES,t}$ are in very close agreement for each resolution, except for 20 m, where values show a slight departure, assumed to be the result of a low sample number $N_c = 7$, and over more samples would be expected to converge.

The error in wake center velocities between the synthetic scans and LES fields is shown Figure 62, for different resolutions of the PPI scan geometries. Here the error is defined as the absolute value of the difference in velocity, ensemble-averaged over the number of cycles N_c in order to produce a reliable estimate by which to evaluate the accuracy of each geometry. Note that in computing error $\langle u_s \rangle - \overline{u_{LES,t}}$, the error is between already-averaged velocities.

Looking at errors in the first one diameter downstream of Figure 62, it is clear that high resolutions perform better, while this is not strictly the case moving further downstream. The top two plots show major changes in error for the extreme high and low resolutions moving downstream. This indicates that the optimal resolution depends on which part of the wake is of most interest to a particular study.

As with the wake center location error, the errors of the already-averaged velocities were also computed, available in the Appendix. These errors are further discussed in the following section.

8.2.3 Galion data

The data from a single scan in May 2017 in Perdigão is also compared to the time-averaged LES metrics in Figures 63 and 64 show the wake center location and velocities as compared to the time-averaged metrics metrics. As expected from previously inspecting the lidar scan data in Figure 41, the wake center is near the time-averaged location for $x^+/D \leq 1.5$, beyond which the wake is detected much lower, in the terrain-generated turbulence. The same sudden shift beyond $x^+/D = 1.5$ is observed in values for u_G, the wake center velocities. Note that the difference

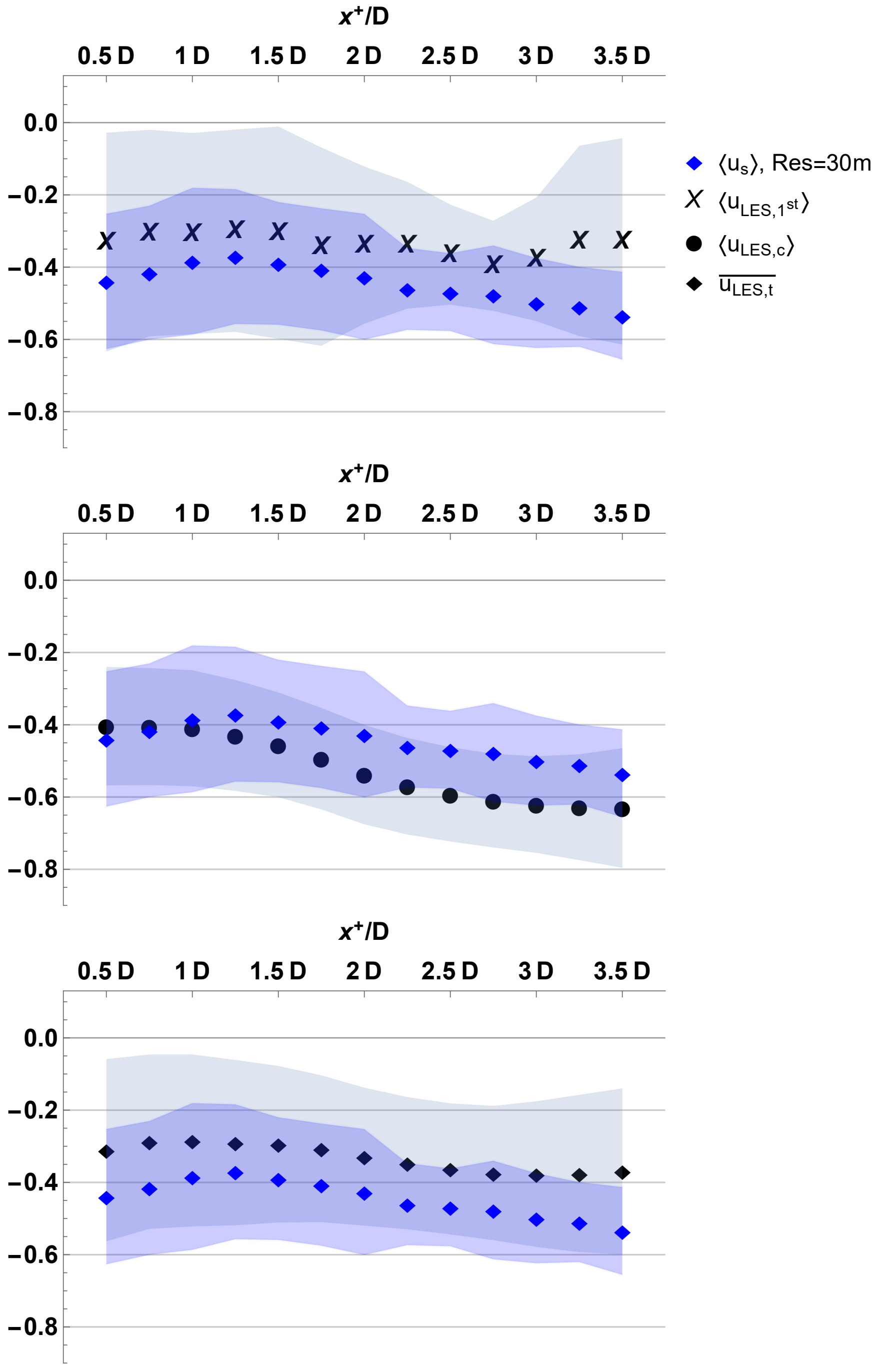

Figure 60: Averaged wake center velocity comparison for geometry PPI30. Shaded area represents ± a single standard deviation

between the Galion data and LES-derived metrics are not interpreted as errors, since the field data was collected only for a single scan and for a different mean wind speed, but are shown simply as a check that the LES metrics are not vastly different than the field measurements.

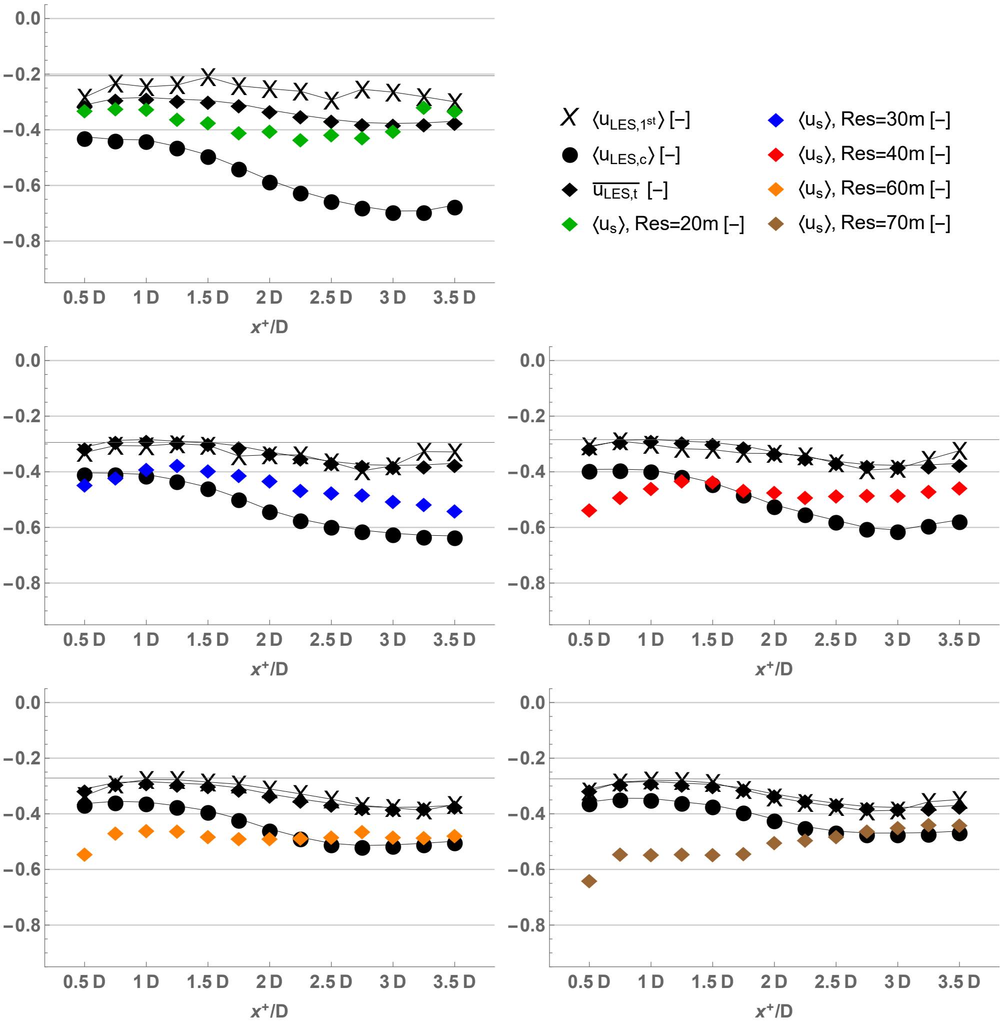

Figure 61: Averaged wake center velocity comparison for PPI geometries.

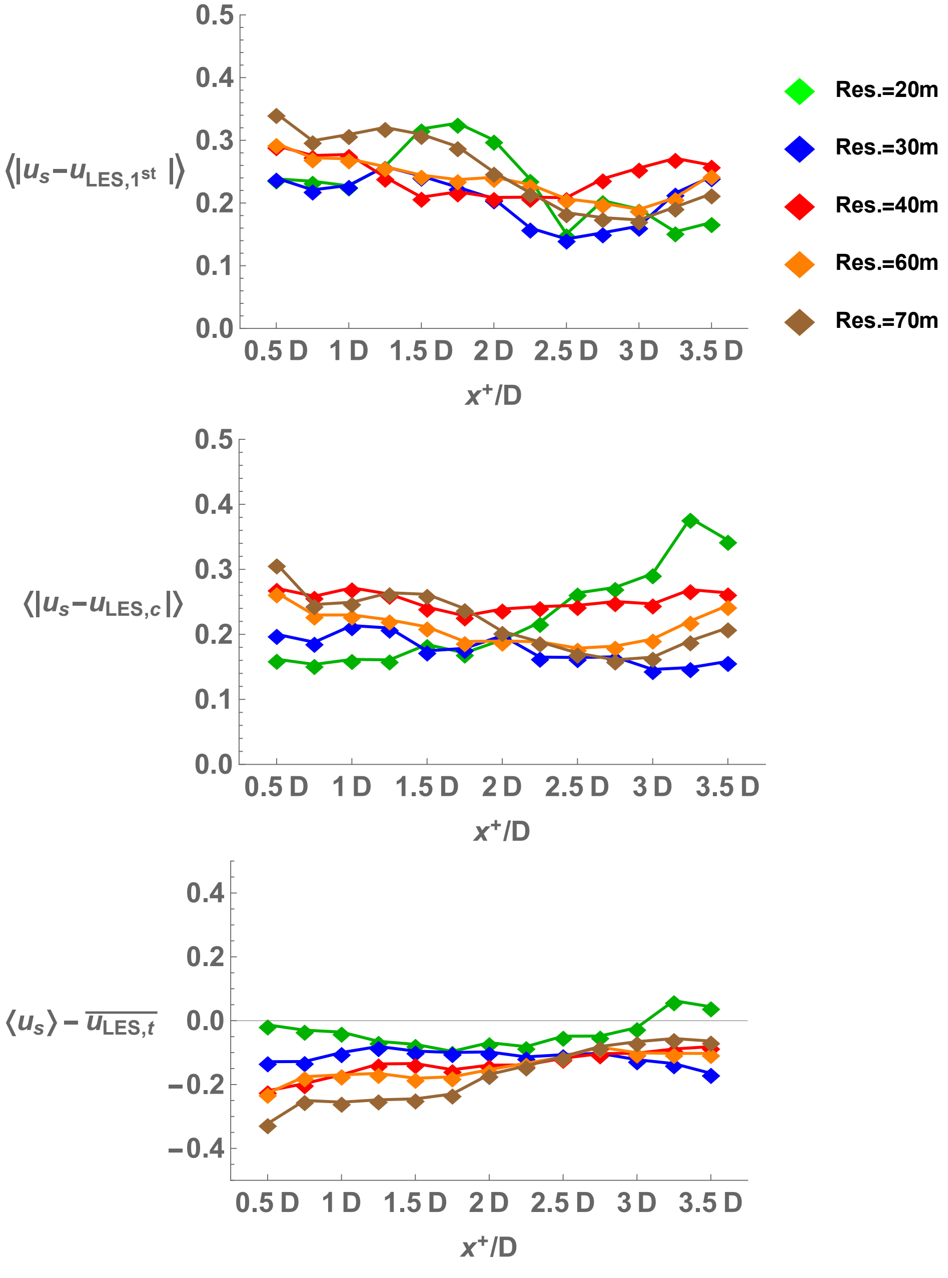

Figure 62: Error of synthetic wake center velocities with respect to three different LES fields

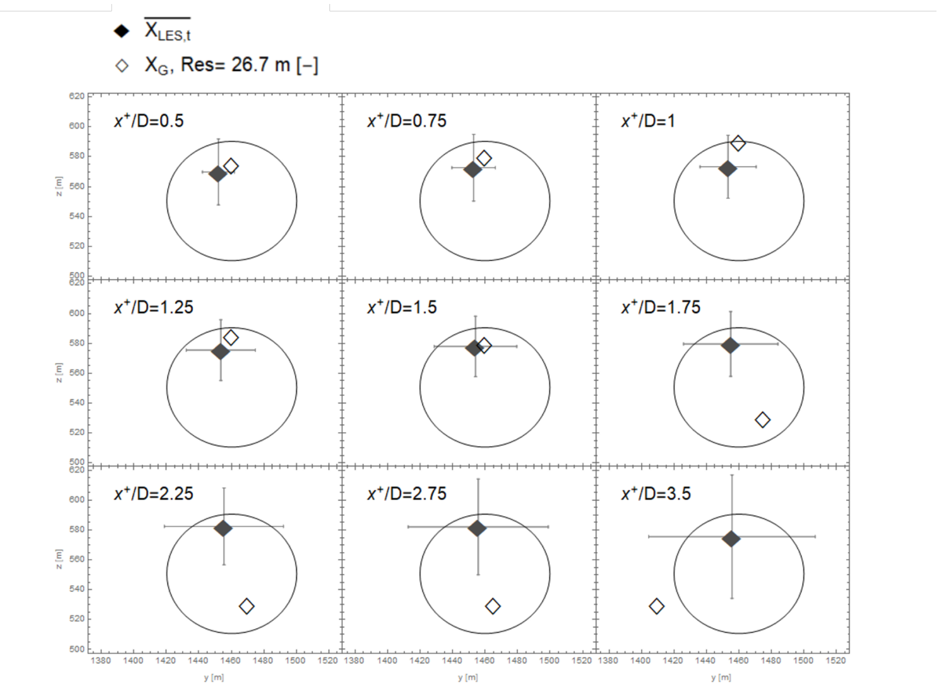

Figure 63: Wake center locations for the single Galion scan X_G and time-averaged wake center locations for all LES fields $\overline{X_{LES,t}}$.

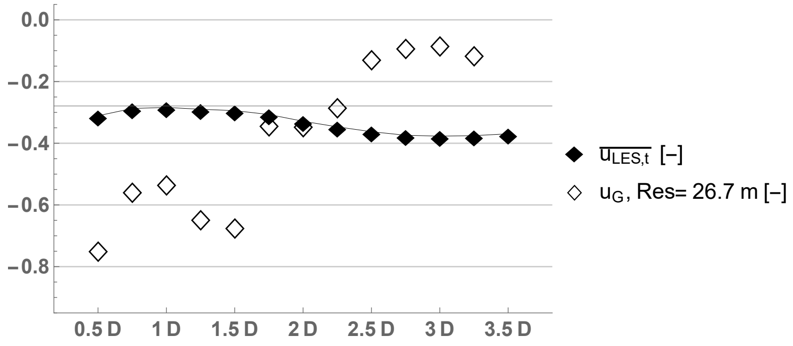

Figure 64: Wake center velocities for the single Galion scan u_G and time-averaged wake center velocites for all LES fields $\overline{u_{LES,t}}$.

9 Analysis and Conclusion

It is important to consider the practical consequences of the results, for example, which are the most useful to wind turbines/farms and the most feasible to apply to existing lidar methods to improve their predictive power. Also the degree to which these results can be trusted must be considered, by understanding the flaws of the methods used in their determination. One aspect to keep under close scrutiny are flaws in the wake center detection algorithm.

9.1 Consistency of wake center detection

Before generating conclusions on geometries, it is important to keep in mind the consistency of wake center estimates. This is visualized in Figure 65 with a histogram of the wake center positions $X_{LES,t}$. Notice the grouping of wake center locations near the bottom, around a clearly visible edge, which is the bottom limit of the search plane of Figure 37, intended to avoid searching regions of terrain turbulence for the wake. Notice that at $x^+/D \geq 3$, the number of $X_{LES,t}$ located at the bottom sharply increase, as the algorithm gets caught in this terrain turbulence below. These wake center data of $x^+/D \geq 3$ do not represent the wake well and so will be discarded in evaluating the performance of each geometry in Section 9.2.

9.2 Error Tables

We look to quantify the general performance of each geometry given by their errors, already presented in Sections 8.2.1 and 8.2.2. A simple overall estimate of a geometry's performance is made by averaging the error across all downstream locations. Equations 9.1 and 9.2 are definitions for an overall error estimate for wake center velocity and wake center location, given by E_{u_r} and E_x, respectively. Note that planes i being averaged are from the first $x^+/D = 0.5$ ($i = 1$) to $x^+/D = 2.75$ ($i = 10$), as the planes further downstream are deemed to produce inaccurate data, as mentioned previously. Equation 9.1 defines error in wake center velocity as the mean absolute error of u_s and u_{LES}, ensemble-averaged over each cycle and each downstream plane i.

$$E_{u_r} = \frac{1}{10}\sum_{i}^{10}\langle|u_s - u_{LES}|\rangle_i \tag{9.1}$$

Equation 9.2 defines error in wake center location as the euclidean distance between X_s and X_{LES}, ensemble-averaged over each cycle and over each downstream location i.

$$E_X = \frac{1}{10}\sum_{i}^{10}\langle\|X_s - X_{LES}\|\rangle_i \tag{9.2}$$

Only the errors for the method of finding the average of the errors is presented, while the results for the *error of the averages*, $\|\langle X_s\rangle - \langle X_{LES}\rangle\|$ and $|\langle u_s\rangle - \langle u_{LES}\rangle|$ are not used as error estimators, for reasons discussed in Section 9.3.

The best performing geometry for each type of estimator is highlighted in Tables 10 to 12. For the PPI geometries, the 30 m resolution scans in general show the lowest error, while the extreme low resolution 70 m scans show the worst performance. Of the RHI scans, the best performing geometry is less clear, optimal more or less scattered evenly over resolutions, and at error levels

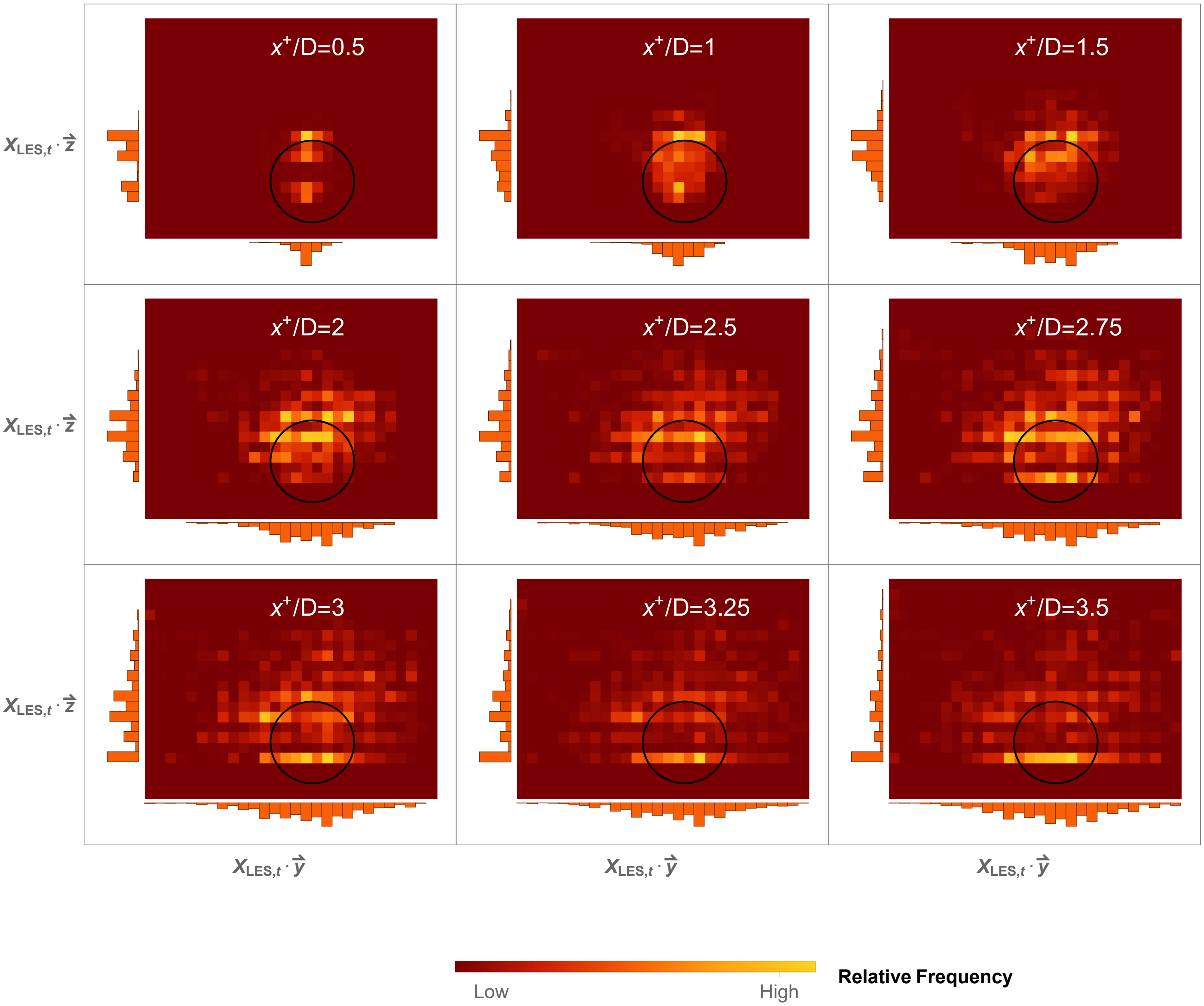

Figure 65: Histogram of wake center locations $X_{LES,t}$ over all instantaneous fields, where $\vec{y}$ and $\vec{z}$ are unit vectors

roughly similar to those of PPI scans. The GAL geometry shows higher error levels than the optimal PPI and RHI scans by nearly every estimator.

	LES,1st		LES,c		LES,t	
Resolution	E_{u_r} [–]	E_x [m]	E_{u_r} [–]	E_x [m]	E_{u_r} [–]	E_x [m]
Res=20m	0.25	0.45 D	0.19	0.36 D	0.06	0.16 D
Res=30m	0.21	0.44 D	0.19	0.34 D	0.11	0.04 D
Res=40m	0.24	0.57 D	0.25	0.42 D	0.15	0.15 D
Res=60m	0.25	0.51 D	0.21	0.48 D	0.16	0.13 D
Res=70m	0.27	0.64 D	0.23	0.62 D	0.21	0.22 D

Table 10: Error levels for PPI geometries. Green-highlighted entries mark the lowest error of each estimator.

	LES,1st		LES,c		LES,t	
Resolution	E_{u_r} [–]	E_x [m]	E_{u_r} [–]	E_x [m]	E_{u_r} [–]	E_x [m]
Res=20m	0.25	0.51 D	0.26	0.33 D	0.05	0.12 D
Res=30m	0.19	0.50 D	0.21	0.41 D	0.09	0.15 D
Res=40m	0.19	0.47 D	0.22	0.34 D	0.09	0.11 D
Res=60m	0.25	0.49 D	0.21	0.45 D	0.16	0.10 D
Res=70m	0.27	0.61 D	0.23	0.58 D	0.21	0.18 D

Table 11: Error levels for RHI geometries. Green-highlighted entries mark the lowest error of each estimator.

	LES,1st		LES,c		LES,t	
Resolution	E_{u_r} [–]	E_x [m]	E_{u_r} [–]	E_x [m]	E_{u_r} [–]	E_x [m]
Res=26.7m	0.31	0.45 D	0.23	0.43 D	0.37	0.12 D

Table 12: Error levels for GAL geometry.

9.3 Error Analysis

It is important to ask in what situations the above estimators are relevant, and relate the answer to the goals of wake characterization. Then, one can ask what causes certain geometries to perform better than others, and how they might be improved further.

9.3.1 Goals of wake characterization

It is clear that an understanding of wake location and velocity deficit is crucial for the capture of power by downstream turbines. However, it is less clear over which time scales these metrics should be analyzed− is knowing their short-term value (e.g. instantaneous or over a scan cycle period), or long-term average value more important? Surely one would like to know the wake position over the next 10 minutes, perhaps to control a downwind turbine accordingly, but also to know the long term average wake position for planning turbine locations. The goal of this study is to compare the relative accuracy of wake characteristics from lidar scans, and since the wake metrics have a time dependency, their accuracy can be different on short time scales (the error of a single scan), than on longer scales (the error of averaged metrics). This will decide in which cases the error estimators in Tables 10 to 12 are appropriate.

9.3.2 Applicability of Different Error Estimators

As seen in Section 8.2, the error levels change depending on whether the average of the errors, or the error of the averages is taken. In order to judge the effectiveness of each method, one must consider the effect of averaging time on the metrics. In general, one would like the flow statistics to be constant throughout the averaging time, under the assumption that the wake metrics also remain relatively constant, and therefore their averaged value is close to the true value during the averaging period. Similar to the definition of homogeneity in space is stationarity in time, defined as conditions when flow statistics are not time dependent [28]. This means the underlying probability distribution function of wind speeds and wind direction, for example, remain constant in time. Also, stationarity means that ensemble averages, as their sample number increases, approach the time average [14]. However, for wind energy applications, wind speeds in non-complex terrain are conventionally considered stationary for up to 10-minutes [12], so the meaning of a wake metric averaged over longer than 10 minutes is difficult to interpret, as conditions do not remain stationary that long in reality, especially in complex terrain. However in this specific case, the LES model *is* stationary over long time scales, e.g. the stability conditions remain neutral, the long-term averaged mean wind direction and driving pressure gradient are constant in time. Furthermore, the large characteristic length scales of the current terrain (mountain heights) produce large time scales, the largest of which can be estimated as the largest eddy size possible in the domain, $t_E = z_{max}/u_*$. For this calculation, a lower value of u_* than used for the pressure gradient in Section 5 is applied. This is because in complex terrain, the pressure balance also involves the pressure differential formed by drag on the ridges, reducing the effective friction velocity. Thus u_* is estimated as 0.3 m s^{-1} in the above expression, and $t_E = 2.78$ hours, which far exceeds $T_{LES} = 1.78$ hours, meaning that quantities $\overline{X_{LES,t}}$ and $\overline{u_{LES,t}}$ have not been averaged long enough to achieve stationarity, and don't represent the converged long-term average values. Additionally, non-stationary effects common of complex terrain, such as drainage winds (where air close to the terrain is cooled and flows downhill [29]), have their own time scales which need to be taken into account with respect to averaging times.

This is in contrast with the errors of the form $\langle |u_s - u_{LES}| \rangle$, which evaluate the error of each scan individually. This short-term error provides a measure of the random error of the scan which the long-term averaged error does not. Therefore the errors $\langle |u_s - u_{LES,1^{st}}| \rangle$ and $\langle |u_s - u_{LES,c}| \rangle$ are considered a good general indicator of scan geometry performance, and will be used to evaluate accuracy.

As mentioned, wake metrics in these fields heavily depend on performance of the wake detection algorithm. For example the results of the algorithm for an instantaneous field $u_r^*(\boldsymbol{x}, t_0)$, compared to a cycle-averaged field like $\widetilde{u_r^*}(\boldsymbol{x})$, are more sensitive to random velocity fluctuations, as the wake center is more prone to be misidentified as lying in a region of slow moving air outside the wake center. On the other hand, using the algorithm on a cycle-averaged field, where the wake is more spread out and its center location less definite, can lead to the problem seen in Figure 51, where the turbine wake becomes indistinguishable from the terrain wake and the wake center is detected in the low-momentum region behind the ridge. It is expected that the relative accuracy of $u_{LES,1^{st}}$

and $u_{LES,c}$ depends on both the time scales of the wake center motion as well as of the velocity fluctuations, the ideal case being that for the cycle-averaged field, the fluctuations are smoothed out while the wake motion is slow enough for its location to be accurately represented. If that is the case, the cycle-averaged field $u_{LES,c}$ would better for determining error in wake location, while the first instantaneous field $u_{LES,1^{st}}$ would give a better indication of error in wake center velocity. With this criteria in mind, the error levels in Tables 10 to 12 are analyzed: geometries PPI30 and RHI40 give the lowest combination of E_{u_r} for the LES first instantaneous fields and E_X for the cycle-averaged field, and are considered optimal.

9.3.3 Consequences of error levels

The error in wake center velocity can be analyzed in terms of consequences for wind turbine power production. For example, the most optimistic error level (found in the PPI30 geometry) is $E_{u_r} = 0.19$. Recall that this error is a non-dimensional quantity since

$$u_s - u_{LES,1^{st}} = \text{Max}[u_r^*(\boldsymbol{x}, t)] - \text{Max}[u_r^*(\boldsymbol{x}, t_o)]$$

and $u_r^* = u_r/|u_{\infty,LES}|$, where $u_{\infty,LES} = -4.10ms^{-1}$. Then E_{u_r} is the error per unit free-stream velocity. To give a rough idea of the implications for power production, the average wake center velocity, taken from averaging $\overline{u_{LES,t}}$ at all downstream locations, is $u_r^* = 0.33$. That means, for example, if the synthetic scan underestimates u_r^* by 0.19 (equal to E_{u_r} for PPI30 with the cycle-averaged LES fields in Table 10), the error in wake center velocity is $\frac{(.19-.33)}{.33} = -42\%$. Since the available wind power (in the turbine's partial load region) scales with the incoming wind speed cubed, the percentage drop in estimated power available would be $\frac{.33^3-(.33-.19)^3}{.33^3} = 92\%$ for a turbine directly in the wake. Of course these figures are merely illustrative — such velocity errors cannot be assumed to hold in the far wake, at distances wind turbines are commonly placed in wind farms, and the error in power would be more accurately determined using the rotor area-averaged velocity. Additionally, the average wind turbine power scales with less than the average wind speed cubed, making this error overly conservative. However, there clearly needs to be much improvement in accuracy for these scans to be bankable, and this error far exceeds the uncertainty levels of 15% mentioned in Section 1.2 [7]. However, the goal of this study is to optimize scan geometry, which can be done even with error levels unacceptable for field measurement campaigns.

The consequences of error in wake position are more challenging to assess. In this LES, the wind turbine decays rapidly downstream, making it hard to measure errors in wake position at distances typical of wind turbine spacing. One may consider using the error trend in the near-wake to fit a model to predict error further downstream, however in complex terrain this is not feasible, due to the wake altering effects previously discussed.

9.4 Concluding Remarks

Each geometry that has been tested samples the same LES data, and in stationary conditions, creating a systematic and unbiased estimate of their relative accuracy. Of course this accuracy has been shown to be heavily dependent on the method of wake detection/characterization, and further improvements must be made to ensure this algorithm is sufficiently robust. Although the scan geometries were optimized for two metrics, wake center position and velocity, more metrics need to be tested, creating a larger solution space for optimization.

In optimizing error level, a trade-off in spatial and temporal accuracy is observed between high spatial resolution scans with longer scan times and vice-versa. In general, optimizing this trade-off is made more difficult when time scales introduced by complex terrains are not fully known. The geometries created in this study outperformed the geometry provided from the Perdigão 2017 experiments, due to the much smaller scan area (and scan time). However, the geometries were constructed with prior knowledge from the LES of wind direction and wake location, enabling the coverage area to be narrowed around the wake region. In future studies, it may be practical to test larger scan areas, as it is unlikely in real cases that the wind direction be aligned with the scan geometry as it was in this study.

For overall accuracy in wake center location and velocity, the PPI30 and RHI40 geometries performed best, measured by the ensemble-averaged error between the synthetic lidar metrics and those determined from the first instantaneous field of each scan as well as from the field which has been averaged over the duration of the cycle. These geometries correspond to an effective resolution of 23 to 39 meters on the wake characterizing planes. Although for wind energy applications the error levels are unacceptable, the results of relative accuracy of scan geometries are still considered valid. Several different methods of determining error were investigated, and although errors in long-term averages may be smallest in some cases, they are not a clear an indicator of accuracy outside of the LES, especially in complex terrain. This suggests that the best performing geometries in this study would most appropriately be used for short-term predictions of wake behavior, to be used for example in active wind farm control.

9.4.1 Suggested future work

1. As mentioned, the wake detection and characterization algorithm needs improvement. Currently, the wake search region is somewhat arbitrarily defined by a distance from the previously determined upstream wake center location. The wake search area could be more informed by incorporating an estimated wake expansion, so that as downstream location increases, the search region expands accordingly, which would be a necessary feature anyway if the algorithm were to measure additional characteristics of wake shape and orientation. Also, a more refined definition of wake center would be beneficial, e.g. one similar to that of Doubrawa, Barthelmie, Wang, Pryor and Churchfield (2016) [13], who defined the location as the center of gravity of the wake's velocity deficit distribution.

2. In this study, the lidar location was kept fixed. This was mainly a constraint for problem simplification. Moving the lidar opens up several new possibilities for geometries to test, and lidar uncertainties related to the angles the lidar LOS makes with the wind could also be incorporated [30].

3. The geometry could be varied in other ways, a simple addition being to vary the resolution as a function of distance from turbine axis, using different functions to determine clustering of the measurement points, e.g. cosine, parabolic, or triangular functions.

4. Fourier analysis could be used to observe time scales of the wake characteristics. For example by transforming a time series of wake center position to the frequency domain, estimates of the wake position time scales could be made and then compared to the averaging times and scan cycle periods.

5. The LES could incorporate stability effects and also a less-smoothed terrain, as the latter has shown to greatly influence flow behind the Perdigão north ridge [4].
6. The turbine model could be improved beyond a non-rotating actuator disk to incorporate rotational effects, or replaced by an actuator line model to more accurately represent near-wake physics.
7. The number of scan cycles are not equal for each geometry in this study, as each scan geometry is cycled for as many times as possible within the total simulation time. Increasing the scan sample size N_c and making them equal for all geometries would provide an improved comparison of geometry performance.
8. Synthetic lidar scans could be used to optimize scan geometry not only for wake characterization but also to study flow around the entire site, e.g. flow speed-up on the ridge or drainage winds. Also, measurement of velocity profiles and turbulence statistics could be optimized to predict the power available at prospective wind turbine sites and loadings.
9. Integrate the synthetic lidar scans with the control of a simulated wind turbine. Prediction of the wake location could be used to actively yaw the upstream turbine to steer the wake and pitch the blades or yaw the downstream turbine.

References

[1] Kate Marvel, Ben Kravitz, and Ken Caldeira. Geophysical limits to global wind power. *Nature Climate Change*, 3(2):118–121, 2013.

[2] International Renewable Energy Agency (IRENA). Renewable capacity statistics, March 2017.

[3] Alfredo Peña, Charlotte Bay Hasager, Merete Badger, Rebecca Jane Barthelmie, Ferhat Bingöl, Jean-Pierre Cariou, Stefan Emeis, Sten Tronæs Frandsen, Michael Harris, Ioanna Karagali, Søren Ejling Larsen, Jakob Mann, Torben Mikkelsen, Mark Pitter, Sara Pryor, Ameya Sathe, David Schlipf, Chris Slinger, and Rozenn Wagner. Remote sensing for wind energy, 2015.

[4] J. Berg, N. Troldborg, N.N. Sørensen, E. G. Patton, and P. P. Sullivan. Large-eddy simulation of turbine wake in complex terrain. *Journal of Physics: Conference Series*, 854(1):012003, 2017.

[5] Jakob Mann, Nikolas Angelou, Johan Arnqvist, Doron Callies, E. Cantero, Roberto Chavez Arroyo, Michael Courtney, J. Cuxart, Ebba Dellwik, Julia Gottschall, S. Ivanell, Phoebe Kuhn, Guillaume Lea, C.J.S. de Matos, J.M.L.M. Palma, Lukas Pauscher, Alfredo Peña, Javier Sanz Rodrigo, Stefan Söderberg, Nikola Vasiljevic, and C Veiga Rodrigues. Complex terrain experiments in the new european wind atlas. *Philosophical Transactions of the Royal Society A: Mathematical, Physical and Engineering Sciences*, 375(2091), 2017.

[6] H. J. S. Fernando, S. M. Lee, J. Anderson, M. Princevac, E. Pardyjak, and S. Grossman-Clarke. Urban fluid mechanics: Air circulation and contaminant dispersion in cities. *Environmental Fluid Mechanics*, 1(1):107–164, 2001.

[7] European Wind Energy Technology Platform. Strategic research agenda / market deployment strategy. *WindEurope*, 2014.

[8] Wood Group. Products: Galion lidar. *Available at* `https://www.woodgroup.com/what-we-do/view-by-products-and-services/clean-energy/products/galion-lidar`.

[9] Julie K. Lundquist Harinda Jospeh S. Fernando. Perdigão science program overview. *Available at* `https://www.eol.ucar.edu/field_projects/perdigao`.

[10] Nikola Vasiljević. Flickr photo gallery of perdigão 2014 site visit. *Available at* `https://www.flickr.com/photos/zamjatin/sets/72157649022069345`.

[11] G. A. M. van Kuik, Joachim Peinke, R. Nijssen, D.J. Lekou, Jakob Mann, Jens Nørkær Sørensen, C. Ferreira, J. W. van Wingerden, D. Schlipf, P. Gebraad, Henk Polinder, Asger Bech Abrahamsen, G.J.W. van Bussel, John Dalsgaard Sørensen, P. Tavner, C. L. Bottasso, Michael Muskulus, D. Matha, H. J. Lindeboom, Steven Degraer, O. Kramer, S. Lehnhoff, M. Sonnenschein, Poul Ejnar Sørensen, R. W. Künneke, Poul Erik Morthorst, and Klaus Skytte. Long-term research challenges in wind energy – a research agenda by the european academy of wind energy. *Wind Energy Science*, 1:1–39, 2016. © Author(s) 2016. CC Attribution 3.0 License.

[12] Jacob Berg, Jakob Mann, Mark Kelly, and Morten Nielsen. Technical university of denmark course reader for 41600: Micro meteorology for wind energy, 2016.

[13] Paula Doubrawa, Rebecca J. Barthelmie, Hui Wang, S. C. Pryor, and Matthew J. Churchfield. Wind turbine wake characterization from temporally disjunct 3-d measurements. *Remote Sensing*, 8(11):939, 2016.

[14] John C. Wyngaard. Turbulence in the atmosphere. *Turbulence in the Atmosphere*, pages 1–393, 2010.

[15] Søren Ott, Jacob Berg, and Morten Nielsen. Linearised cfd models for wakes, 2011.

[16] H.K. Versteeg and W. Malalasekera. *An Introduction to Computational Fluid Dynamics: The Finite Volume Method*. Pearson Education Limited, 2007.

[17] Stephen B Pope. Turbulent flows. *Measurement Science and Technology*, 12(11):2020, 2001.

[18] Sina Shamsoddin and Fernando Porte-Agel. Large-eddy simulation of atmospheric boundary-layer flow through a wind farm sited on topography. *Boundary-layer Meteorology*, 163(1):1–17, 2017.

[19] P.S. Jackson and J.C.R. Hunt. Turbulent wind flow over a low hill. *Quarterly Journal of the Royal Meteorological Society*, 101(430):929–955, 1975.

[20] P. J. Mason and R. I. Sykes. Flow over an isolated hill of moderate slope. *Quarterly Journal of the Royal Meteorological Society*, 105(444):383–395, 1979.

[21] A. Bechmann, N. N. Sørensen, J. Berg, J. Mann, and P.-E. Réthoré. The bolund experiment, part ii: Blind comparison of microscale flow models. *Boundary-Layer Meteorology*, 141(2):245, Aug 2011.

[22] G.J. Taylor and D Smith. Wake measurements over complex terrain. *Wind Energy Conversion 1991*, pages 335–342, 1991.

[23] Jeffrey D. Mirocha, Daniel A. Rajewski, Nikola Marjanovic, Julie K. Lundquist, Branko Kosovic, Caroline Draxl, and Matthew J. Churchfield. Investigating wind turbine impacts on near-wake flow using profiling lidar data and large-eddy simulations with an actuator disk model. *Journal of Renewable and Sustainable Energy*, 7(4):043143, 2015.

[24] Peter P. Sullivan, James C. McWilliams, and Edward G. Patton. Large-eddy simulation of marine atmospheric boundary layers above a spectrum of moving waves. *Journal of the Atmospheric Sciences*, 71(11):4001–4027, 2014.

[25] J. W. Deardorff. Three-dimensional numerical study of the height and mean structure of a heated planetary boundary layer. *Boundary-layer Meteorology*, 7(1):81–106, 81–106, 1974.

[26] Wolfram Research, Inc. Mathematica, Version 11.3. Champaign, IL, 2018.

[27] Aditya Choukulkar, Ronald Calhoun, Brian Billings, and James Doyle. Investigation of a complex nocturnal flow in owens valley, california using coherent doppler lidar. *Boundary-layer Meteorology*, 144(3):359–378, 2012.

[28] S. H. Derbyshire. Atmospheric boundary layer flows—their structure and measurement. by j. c. kaimal and j. j. finnigan. oxford university press. 1994. pp. 289. price £50.00 (hardback). isbn 0 19 506239 6. *Quarterly Journal of the Royal Meteorological Society*, 121(525):1177–1177, 1995.

[29] L. Mahrt, Scott Richardson, David Stauffer, and Nelson Seaman. Nocturnal wind-directional shear in complex terrain. *Quarterly Journal of the Royal Meteorological Society*, 140(685):2393–2400, 2014.

[30] H. Wang, R. J. Barthelmie, S. C. Pryor, and G. Brown. Lidar arc scan uncertainty reduction through scanning geometry optimization. *Atmospheric Measurement Techniques Discussions*, 8(10):10429–10471, 2015.

10 Appendix

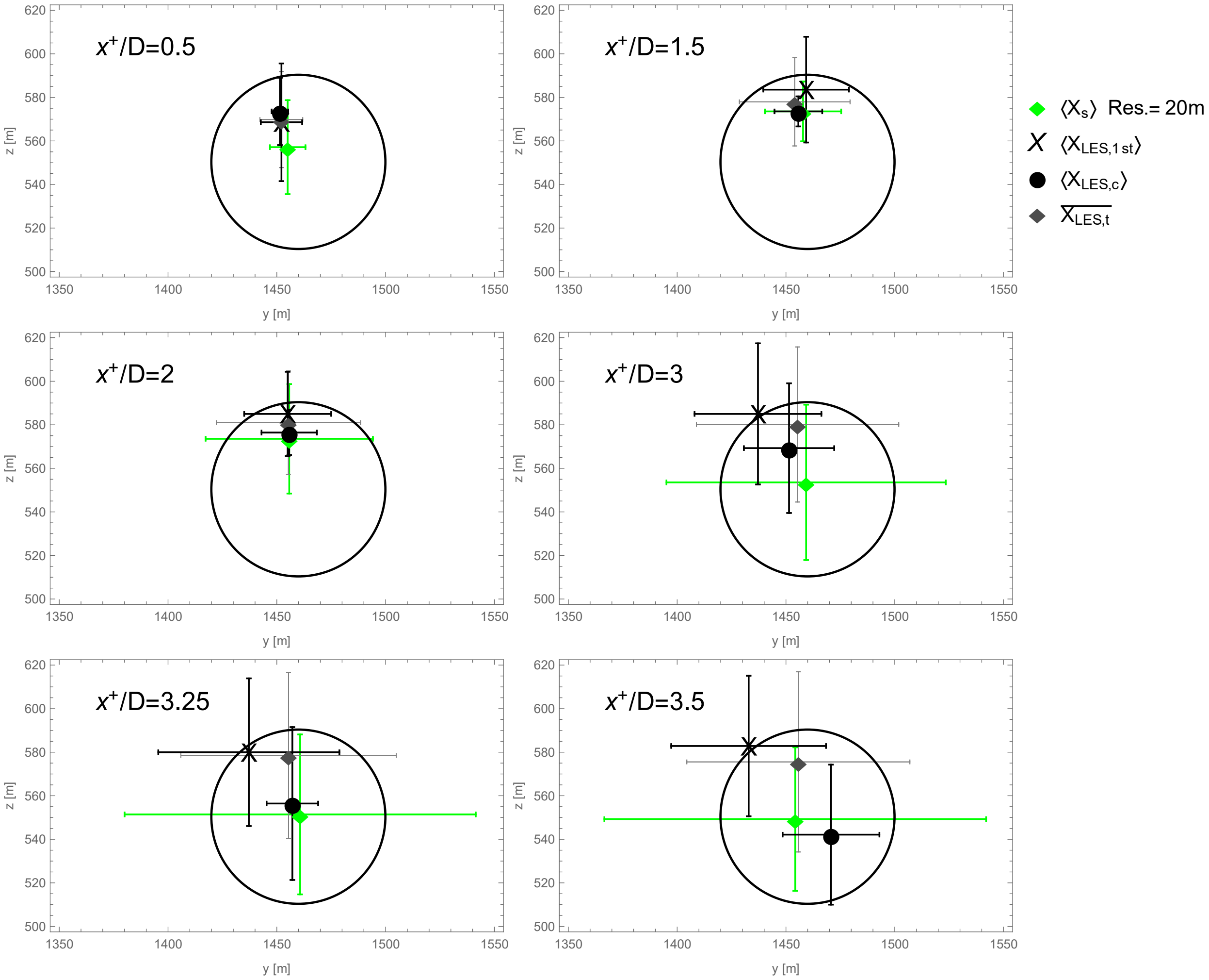

Figure 66: Average wake center location and standard deviation for PPI20 geometry, determined from synthetic and LES fields.

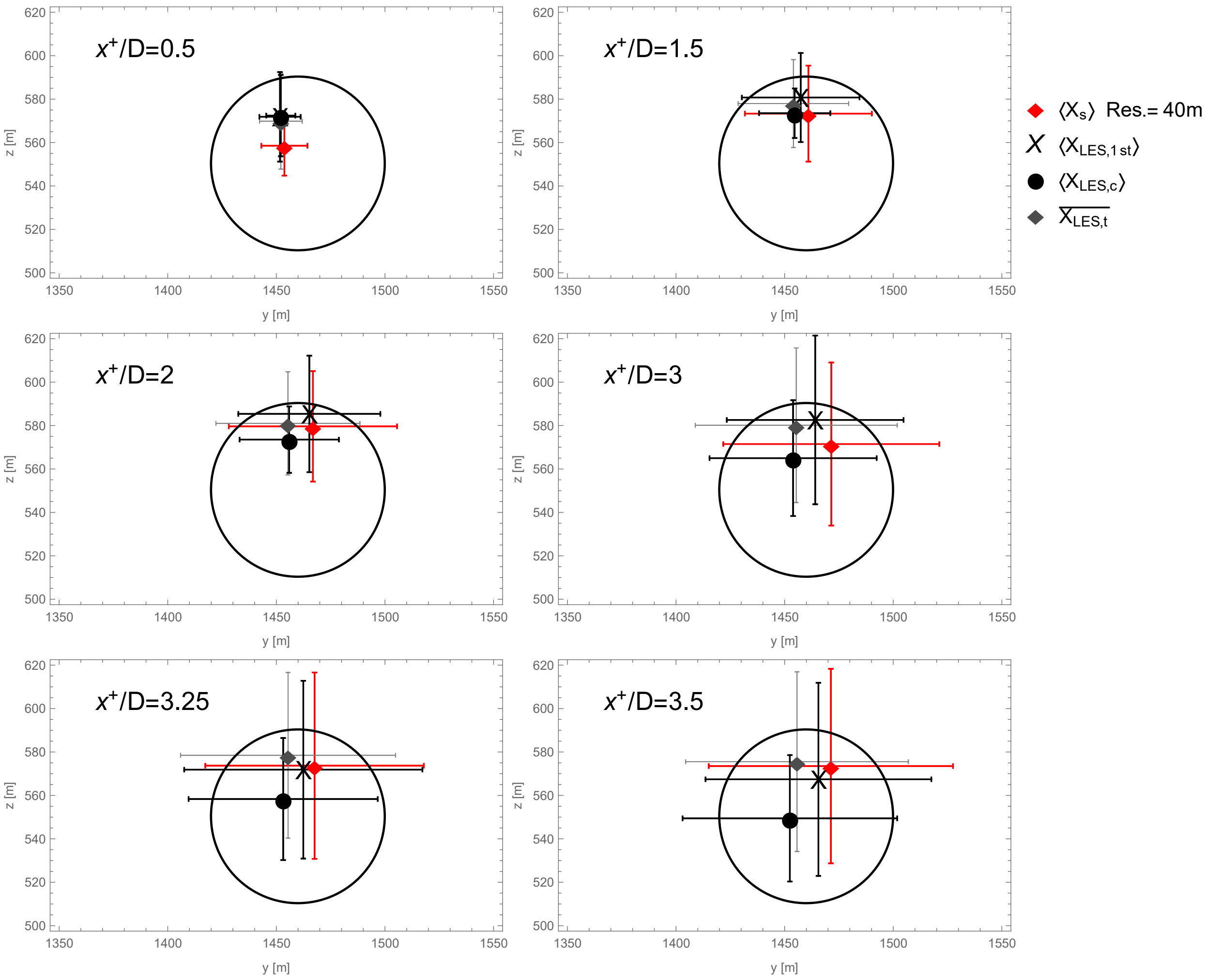

Figure 67: Average wake center location and standard deviation for PPI40 geometry, determined from synthetic and LES fields.

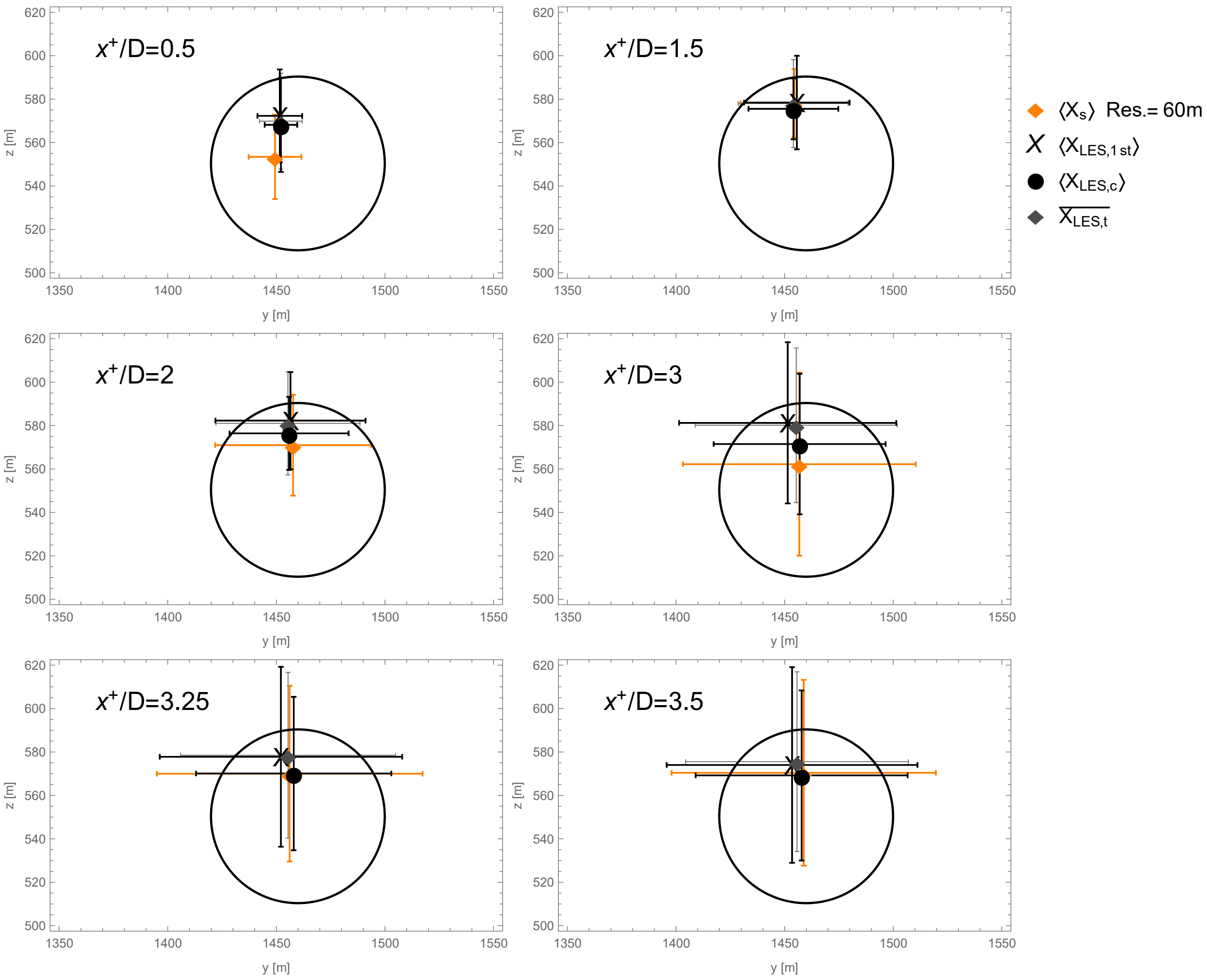

Figure 68: Average wake center location and standard deviation for PPI60 geometry, determined from synthetic and LES fields.

	LES,1st		LES,c		LES,t	
Resolution	E_{u_r} [−]	$E_{\mathbf{x}}$ [m]	E_{u_r} [−]	$E_{\mathbf{x}}$ [m]	E_{u_r} [−]	$E_{\mathbf{x}}$ [m]
Res=20m	0.12	0.19 D	0.16	0.12 D	0.06	0.16 D
Res=30m	0.09	0.07 D	0.08	0.07 D	0.11	0.04 D
Res=40m	0.14	0.12 D	0.07	0.15 D	0.15	0.15 D
Res=60m	0.16	0.15 D	0.07	0.10 D	0.16	0.13 D
Res=70m	0.20	0.22 D	0.13	0.18 D	0.21	0.22 D

Table 13: Error levels of ensemble-averaged metrics for PPI geometries

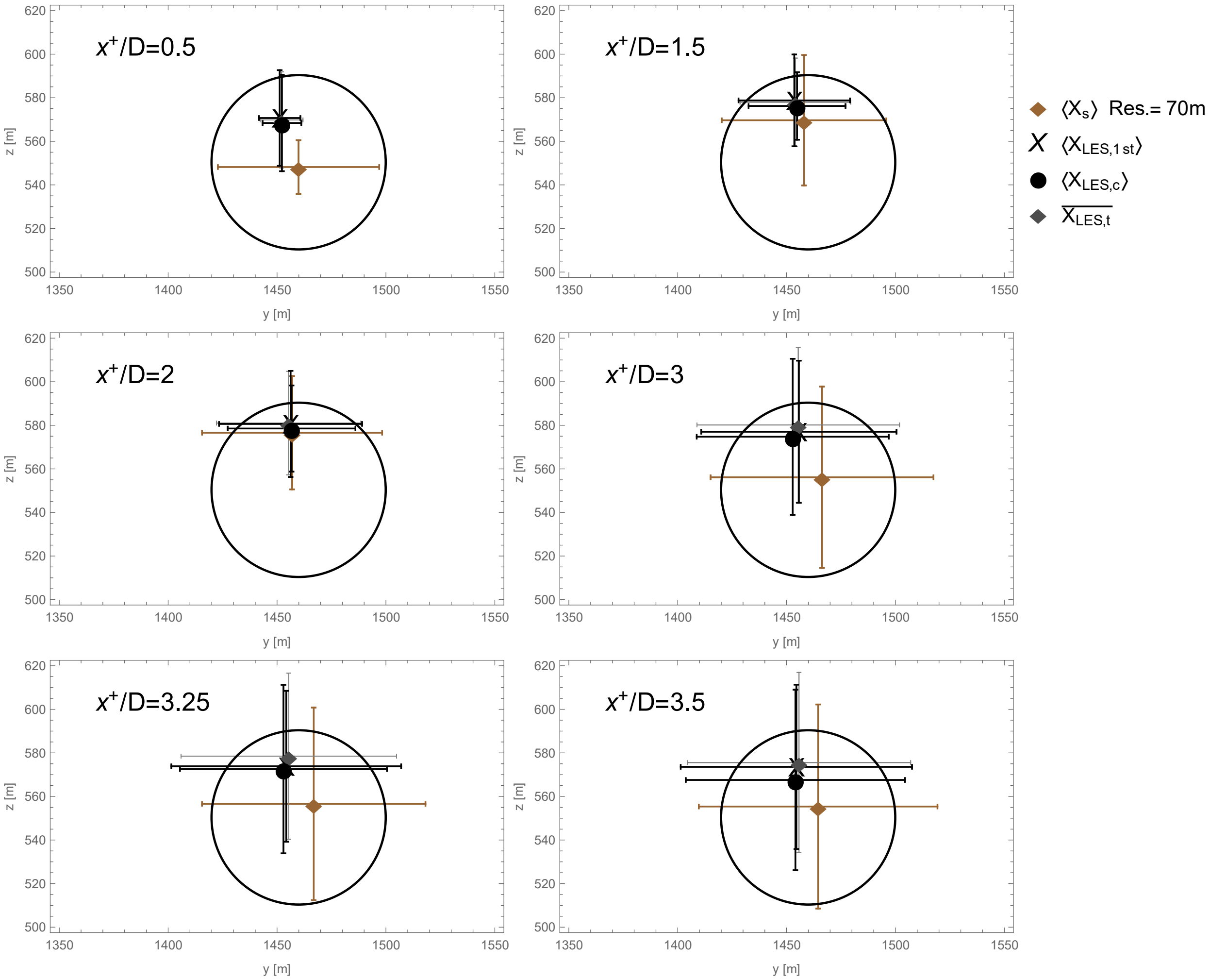

Figure 69: Average wake center location and standard deviation for PPI70 geometry, determined from synthetic and LES fields.

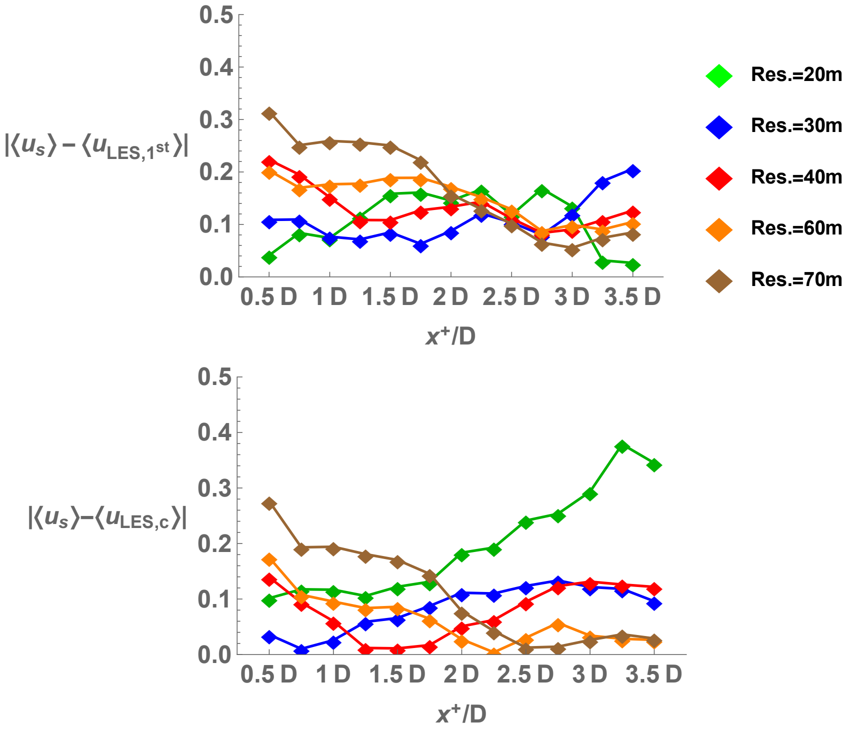

Figure 70: Error of ensemble-averaged wake center velocities with respect to two types of LES fields.